Preliminary Design Optimization of an Amphibious Aircraft

by

Jason W. Cary

A thesis submitted to the Graduate Faculty of
Auburn University
in partial fulfillment of the
requirements for the Degree of
Master of Science

Auburn, Alabama
December 12, 2011

Approved by

Gilbert L. Crouse Jr., Chair, Associate Professor of Aerospace Engineering
John E. Cochran Jr., Professor of Aerospace Engineering
Winfred A. Foster Jr., Professor of Aerospace Engineering

Abstract

An amphibious aircraft combines the speed and range benefits of a conventional aircraft with the ability to land and takeoff on open water. There are other appealing factors to operating an amphibious aircraft including convenience, the ability to operate without a hard surface runway and additional safety for overwater operations. These factors, however, all come at a cost and impact the design of the aircraft. To examine these tradeoffs, common design and optimization methods were applied to the conceptual design of an amphibious aircraft and then compared to wind tunnel results of that design. In this study, a hypothetical troop and cargo transport aircraft mission profile was selected.

A sizing program was developed to create an aircraft geometry and evaluate its performance. This code was written to account for many different aircraft criteria, including tail configuration, wing and fuselage geometry, and method of water operation (floats, hydrofoil, boat hull, etc.). The sizing code was first validated on several classes of existing aircraft. It was then run in conjunction with a hybrid, particle swarm-simplex optimizer to find a configuration for the hypothetical transport aircraft with minimum overall weight.

The optimized design was tested in Auburn University's subsonic, 3 ft. x 4 ft. wind tunnel. The model was run through a battery of tests including measuring the forces and moments, and surface flow visualization. Runs were made at various angles of attack and sideslip angles. The testing included cases with several different control surface deflections. Analysis was also performed

on the aircraft using Athena Vortex Lattice and Orca3D to determine stability in flight and while on water. Results of the testing were used to validate the performance parameters estimated by the design code.

Acknowledgments

The author would like to thank Dr. Gilbert L. Crouse Jr. for the opportunity to work on this research as well as for his guidance and support throughout the course of this effort. Thanks are also due to Mr. Jason Welstead, Mr. Brian Reitz, Mr. David Wall, and Ms. Rachel Ottaway for all the assistance they offered over the course of this research. Many thanks go to Andy Weldon for the advice and work he put into every piece machined for this project. The author would also like to thank his father and mother for their help, support and encouragement.

Table of Contents

List of Figures

List of Tables

Chapter 1

Introduction

An amphibious aircraft can be defined as an aircraft that can take off and land on either land or water. There are historically two classes of amphibious aircraft: flying boats and floatplanes. The earliest examples of amphibious aircraft were built in the 1920's but they did not see widespread service until World War II. The first amphibious aircraft in use by the United States military were a family of light-utility, amphibious aircraft produced by the Grumman Corporation: the Goose, the Widgeon, and the Mallard. Initially produced for civilian use, the potential military applications of these aircraft were quickly recognized and large numbers were put into service in air-sea rescue and anti-submarine patrol roles. Following these successes, Supermarine Aircraft in the United Kingdom produced the Walrus and the Sea Otter, a family of single-engine biplanes which were also used during World War II, performing observation and rescue duties. Following the war, the demand for amphibious aircraft began to decrease due to the increased availability of hard surface landing strips in remote areas. Today, the main roles of amphibious aircraft are in firefighting, search and rescue, as well as providing access to remote, unforgiving locations [1].

1.1 Amphibious Aircraft Design

Unfortunately, designing an aircraft capable of landing and taking off on open waters will incur penalties on the aerodynamics and performance of the aircraft, generally in the form of additional weight and drag. These penalties

make it increasingly important that, for a given mission profile, an amphibious aircraft be properly sized during the preliminary design phase.

An amphibious aircraft must be designed to meet the conditions of both a boat and an aircraft. For example, when on water, the seaplane should have good takeoff and landing characteristics, proper amounts of buoyancy, and adequate lateral and longitudinal stability for water operations. When in the air, the primary concerns are the aircraft's aerodynamic characteristics, which are generally hindered through meeting the water operations goals mentioned.

The initial thrust of this research centered on the creation of an amphibious aircraft sizing code that took a basic set of inputs and output the aircraft's geometry and performance data. To allow the designer maximum flexibility when deciding what configuration the aircraft will have, five different water operations methods, three different aircraft tail and wing configurations, two fuel locations, two aircraft types, and two engine types have been included. The designer is allowed to choose from twin floats, a boat hull, a hydrofoil, wing tip floats, sponsons, or any combination thereof for the method of water operations. The sizing code was designed to properly calculate the size of the water operations device and factor it into the drag calculations for the aircraft, which in turn impacts its performance characteristics. The designer can choose between having the aircraft in a canard, conventional or flying wing configuration. The fuel can be located in the wings of the aircraft or held at the center of gravity of the aircraft. The aircraft can either be a cargo/transport aircraft or a general-aviation aircraft, which are the two primary types of amphibious aircraft. Finally, the sizing code has separate models for jet and propeller engine types. The code will take the designer's choices on all these configurations and properly analyze the affect those choices will have on the overall design of the aircraft.

With the sizing code modified to account for the addition of water operations devices, the next thrust of this research was directed toward integrating an optimization algorithm into the sizing code. This allows a number of variables to be systematically varied by the sizing program to find the lightest weight aircraft configuration possible to meet a given mission profile. Multiple optimizers were investigated, including: unconstrained nonlinear optimizers, a constrained linear optimizer, a pattern search optimizer, as well as a hybrid particle swarm-pattern search optimizer. The unconstrained nonlinear optimizers used were the fminsearch and fminunc functions built into MATLAB. The constrained nonlinear optimizer used was the fmincon function built into MATLAB. In the case of this research, a hybrid particle swarm-simplex optimizer was employed as the optimization algorithm. This hybrid optimization algorithm leverages the simplex technique's ability to quickly and efficiently find a local optimum in a well defined solution space, while it uses the particle swarm as a transport mechanism for individual search particles [2]. To test the validity of this sizing code and optimizing algorithm, an aircraft was designed and optimized to meet a hypothetical mission profile. In this case, the mission profile is that of a littoral transport aircraft, capable of carrying 50 soldiers and their equipment or an equal amount of cargo weight totaling 18,750 lb. The aircraft will have range of approximately 1,000 nmi. at a cruise altitude of 20,000 ft. For low altitude landing/approach and extraction, it will operate in ground effect for 30 nmi., representing two, 15 nmi., near-water-level mission legs. The optimization code was used to go through all the various aircraft configurations available to the sizing code, as well as a number of geometrical inputs, eventually resulting in what was the lightest possible configuration and geometry.

Finally, it is important to design an aircraft that is not only optimized for minimum weight, but also has adequate performance characteristics on the water and in the air. To this end, the design of the hypothetical aircraft was run through a number of tests after optimization was complete. This included the design and construction of a wind tunnel model, which was tested in Auburn University's 3 ft. X 4 ft. subsonic wind tunnel to determine the accuracy of the drag and performance estimates given by the design code. Second, the longitudinal and lateral water stability of the design was tested using Orca3D. This was useful in determining whether the sizing code was designing the water operations devices to be of adequate size to stabilize the aircraft while on the water's surface. Finally, Athena Vortex Lattice (AVL) was used to estimate the stability derivatives of the aircraft and assess whether the design had any unstable or divergent flight modes and determine if the tails and control surfaces were sized properly. Together, this information will be useful in determining ways to improve the sizing code and optimization techniques used to make a better preliminary design of an amphibious aircraft.

Chapter 2

Review of Literature

2.1 Aircraft Design

Aircraft design in general and seaplane design in particular have been a focus of study for many decades. Raymer [3] and Roskam [4] have published a detailed breakdown of the steps involved in the conceptual design of aircraft. Their work details the processes involved in taking initial requirements for the aircraft and sizing the aircraft from those requirements. "Sizing" refers to the general size of the aircraft, with special focus on the airplane weight needed to fulfill its required mission objectives. The Class I sizing process, which uses largely empirical methods, does a progressive build-up of the takeoff weight of the aircraft. This build-up includes the weight of the crew, payload, fuel and empty-weight of the aircraft. Raymer performs the empty-weight estimation based on an empirical ratio of the takeoff weight of the aircraft to the empty weight of the aircraft. This ratio can vary depending on the class of the aircraft being designed. The Class II sizing process uses a different method of calculating the empty weight of the aircraft, in which the individual component weights are calculated based on weight equations. The equations are statistically based but they do allow the designer to account for very detailed configuration design parameters. The drawback of this method of empty weight calculation is that the design of the aircraft has to have progressed significantly further than is required in the Class I method. It is necessary to have the aircraft's V-n loads diagram, a preliminary structure for the aircraft, and to have made decisions on all systems and equipment that will be necessary for the aircraft's mission. Once estimates of fuel-fractions during different portions of the mission are made, empty weight

calculations can proceed. Some fuel-fractions (takeoff, climb, descent, landing) are based largely on historical data trends for different segments of the mission. Others, such as cruise, ground effect and reserve time, are calculated based on performance parameters during that mission segment. Finally, an iterative approach is used to calculate an estimated takeoff weight using the estimated fuel-fractions and empty weight equation. An initial takeoff weight guess is made, followed by a statistical empty weight calculation and an estimate of fuel fractions, which leads to an estimated takeoff gross weight. Then, the initial guess is compared to the calculated takeoff gross weight. If the results do not match, a value between the two is used as a next guess and the process is iterated until convergence is obtained.

The next step in the design process outlined by Raymer is to use the initial weight sizing of the aircraft to create a geometry for the aircraft. This includes the selection of airfoil shape, main wing and tail geometries, engine sizing and fuselage sizing. First, an airfoil is chosen based on its lift and drag characteristics during cruise, stall characteristics, pitching moment characteristics, and available thickness necessary to accommodate structure and fuel. Next, the main wing geometry is designed. This consists of determining the necessary planform area, S, of the wing based on its gross takeoff weight and lift coefficient. The shape of the wing is determined by its aspect ratio, taper ratio and sweep angle and any twist in the wing.

The horizontal and vertical tails are designed by Raymer using the "tail volume coefficient" method [3]. Since the force due to the lift produced by the tail is proportional to the area of the tail, the tail-effectiveness is proportional to the tail area multiplied by the length of the tail moment arm. According to Raymer, for the vertical tail, wing yawing moments that must be countered are

most directly related to the span of the wing (b), leading to the "vertical tail volume coefficient" in Equation 2.1.

$$c_{VT} = \frac{S_{VT} L_{VT}}{S\, b} \tag{2.1}$$

In the same way, a horizontal tail or canard must counter the pitching moments caused by the main wing and can be most directly related to the wing mean chord ($\bar{c}$).

$$c_{HT} = \frac{S_{HT} L_{HT}}{S\, \bar{c}} \tag{2.2}$$

Raymer gives typical values of these volume coefficients for multiple classes of aircraft and from that data the planform area of the tails can be calculated. Sizing of the control surfaces (elevator, ailerons, and rudder) is addressed primarily using historical guidelines and trends to determine the spanwise length and the ratio of control surface chord length to main wing chord length.

Raymer performs initial engine sizing using historical thrust-to-weight ratios (T/W) for jet-engine aircraft or power-to-weight ratios for propeller-powered aircraft. T/W is not constant as it varies with the changing weight of the aircraft as fuel is burned. Engines also produce varying amounts of thrust depending on the altitude and velocity which the aircraft is being flown at. In design, the thrust-to-weight ratio is generally referring to the T/W value during sea-level static, standard-day conditions at design takeoff weight and maximum throttle settings. This historical T/W value is then used to calculate the required lift to drag ratio during different mission segments.

Finally, Raymer presents his method of initial sizing of the fuselage. Once again, his method uses a largely statistical method based on historical data trends. The method presented is based solely on gross takeoff weight but has shown to have very good correlation to most existing aircraft. Raymer [5] also

performed a recent analytical optimization study which examined the effect of the fineness ratio in subsonic aircraft. The fineness ratio is the ratio between the fuselage length and its maximum diameter. If the aircraft being designed does not have a circular fuselage, an equivalent diameter is calculated from the cross-sectional area. It was found that the optimum fineness ratio for a subsonic aircraft with its interior volume held constant is generally between six and eight. Corke [6] also details a method for determining over-nose and over-side angles necessary for proper pilot visibility. A majority of this method is based on the landing approach angle and landing velocity. Corke goes on to give over-nose and over-side angles for different aircraft classes for use as a general guideline in the preliminary design phase.

2.2 Water Operations

The primary problem with designing an amphibious aircraft is the large performance penalty incurred due to the adaptation of the airplane to water operations. The addition of any water operations features, such as floats, a hydrofoil, or a boat-hull and sponsons, will negatively impact the aerodynamic characteristics of the aircraft. Not only are there aerodynamic issues, but also stability issues, problems caused by loading due to wave slap, and problems with landing and taking off from anything other than a very calm sea state.

The two primary configurations that aircraft have used for water operations are the boat-hull (Figure 1) with wing-tip floats or sponsons design and twin-float design (Figure 2). Garner and Coombes [7] discuss that both of these design configurations suffer due to the difficulty in designing either configuration with both aerodynamic and hydrodynamic considerations in mind. A compromise

must be made, and this is usually to design the aircraft to be as minimally stable in the water as is necessary to be considered safe. Float designs in particular have a tendency to be longitudinally unstable if pitched nose downwards at approximately one-third of its takeoff speed. This is due to suction over the bottom of the region of greatest curvature, which is generally towards the front of the float. Boat-hulled aircraft have fewer of these longitudinal stability problems, as there is a larger fore- and aft-body to reduce the tendency of the aircraft to pitch at speed.

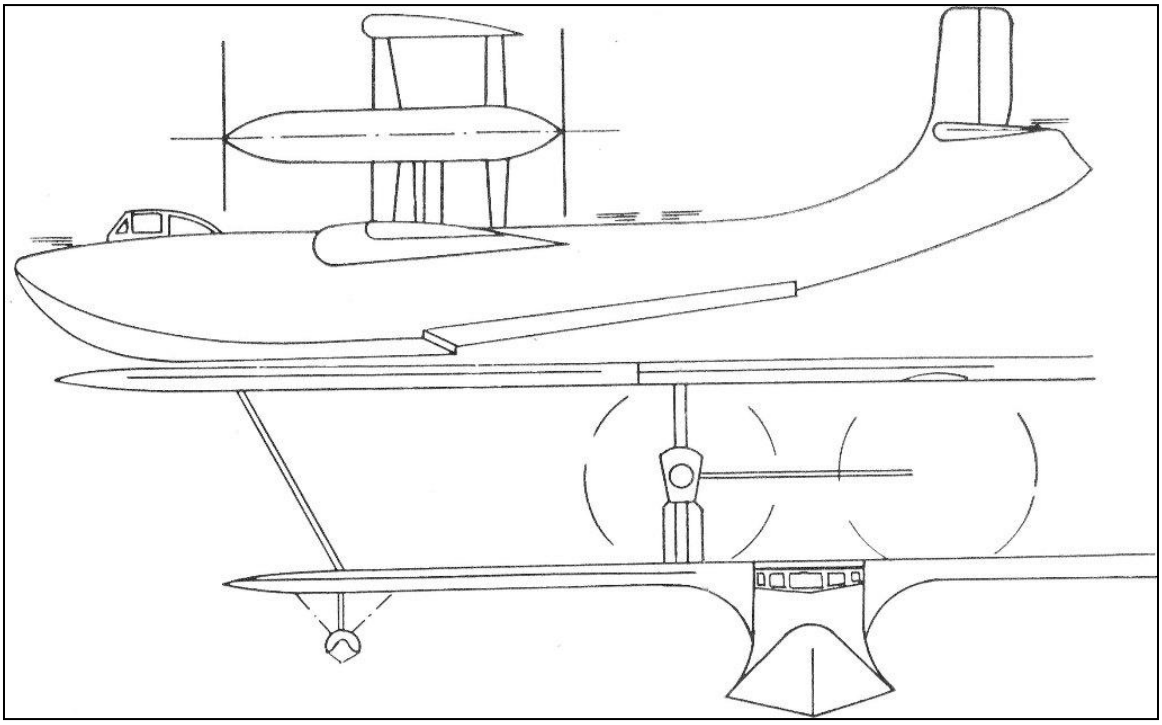

Figure 1: Boat Hull Configuration [8]

Even if a float is designed to be adequately stable longitudinally by having enough of a restoring moment when an angular displacement is introduced, both bodies are still susceptible to longitudinal instability due to insufficient damping, which results in oscillations known as porpoising. Porpoising was studied in detail by Klemin, Pierson and Storer [9]. They determined that there were two main classifications of porpoising. One class can be counteracted by applying a

steady load to the horizontal tail surface, which causes the aircraft to pass to another trim angle, "getting through" the porpoising as quickly as possible. The second class can only be counteracted through an alternative application of upward and downward loads on the tail surfaces, although even this is not always successful.

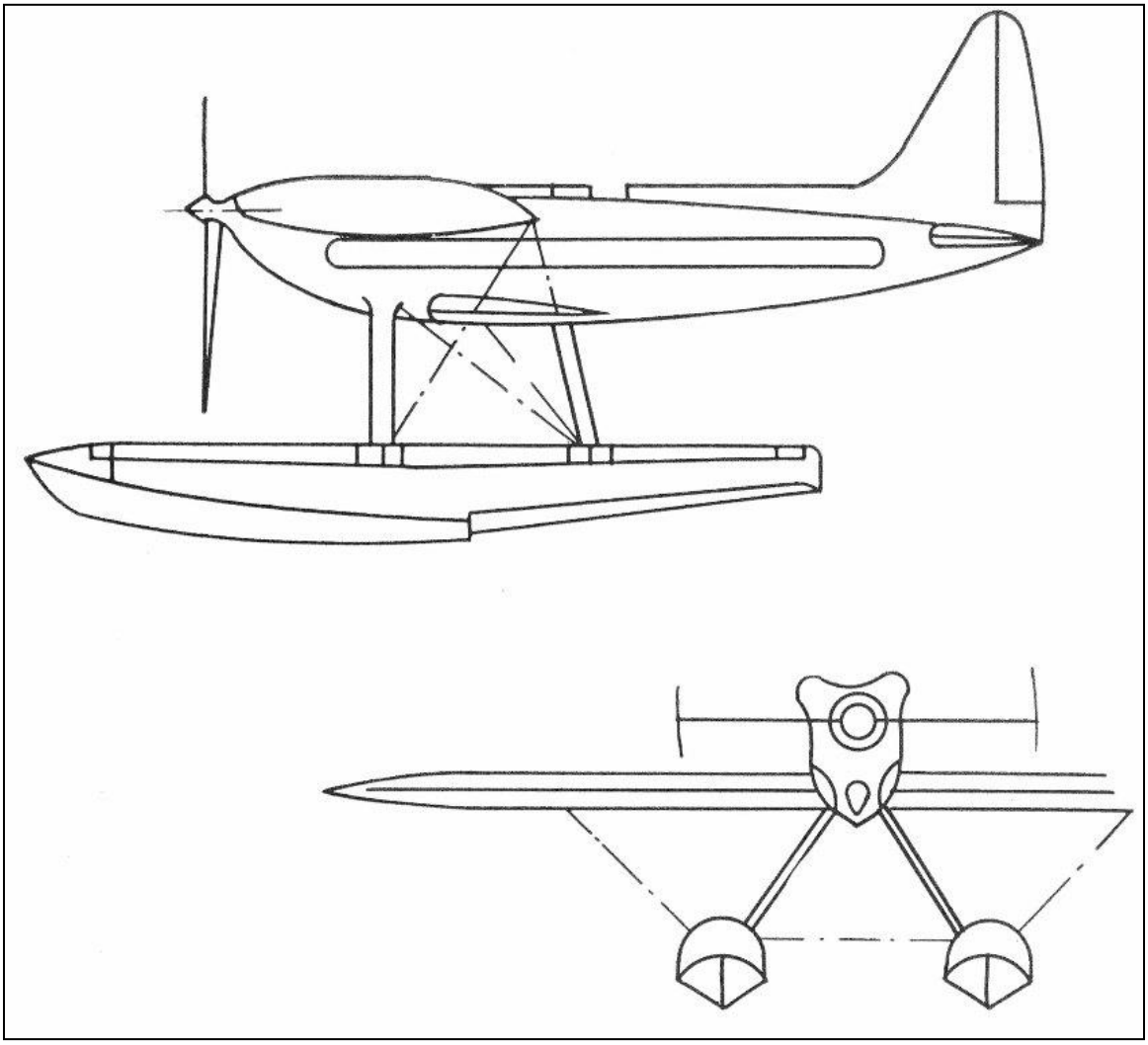

Figure 2: Twin Float Configuration [8]

As shown by Garner and Coombes [7], lateral stability is also an issue with single-body float or boat-hull configurations. This is due to the fact that the metacenter is below the center of gravity of the aircraft. Nelson [8] defines the

metacenter as being the point at which a vertical line from the heeled center of buoyancy crosses through the vertical line of the original center of buoyancy.

This lateral instability can be countered in multiple ways. As the size of the aircraft increases, the center of gravity with respect to the metacenter moves down. It was calculated that for an aircraft with greater than 100 tons of displacement, the center of gravity would be sufficiently low so that no additional lateral stabilizer would be necessary. For small amphibious aircraft though, the issue of lateral stability has been handled primarily in two ways: the addition of a second float to the single float design, and the addition of wing-tip floats or sponsons to the single boat-hull design.

There have been strides made in studying methods of improving a float's hydrodynamics and aerodynamics simultaneously. Benson and Lina [10] performed a study on the use of a retractable planning flap in place of a fixed step on a float. The step is the abrupt break in the bottom line of the float. It is used to cause the water to separate from the float, which leads to a reduction in suction, assists in getting the float to plane, and improves longitudinal control. Performance improvements were gained by adjusting the depth of the retractable step during and after takeoff. Improvements of eight percent in water resistance and two to three percent in total air drag were noted.

Efforts have also been made to decrease the aerodynamic drag of boat-hull designs. A large portion of this work has come in studying the effects of varying the length-beam ratio of the hull of the aircraft, as is discussed by Carter [11]. The length refers to the overall length of the hull while the beam refers to the maximum width of the hull. Carter studied an increase in the length-beam ratio from 6 to 15 while keeping the length-beam product constant. It was found through wind-tunnel tests that, for a length-beam ratio increase from 6 to 15, the

minimum drag coefficient was reduced by 29 percent, while not significantly affecting the hydrodynamics of the hull.

During takeoff in calm seas, it is often possible for a seaplane to operate at trim conditions that give maximum lift to drag ratios. When the aircraft has to takeoff from seas with significant waves, departures from these usual takeoff trim conditions are made due to the uncontrollable pitching and heaving of the aircraft in the water. The aircraft will experience increased water loads. Drag will also increase due to having a larger wetted length to beam ratio. Spray may also become more prevalent, which can lead to having wetted control surfaces that would be dry under nominal conditions. These factors all increase the resistance of the aircraft which leads to a decrease in takeoff performance. Research was conducted by Mottard [12] to examine the effects of these factors on the takeoff resistance. Tests were run on a boat-hulled seaplane with a length to beam ratio of 15 and a wing loading of 120 lb/ft^2. The high wing loading was used so as to have a range of water speeds corresponding to that of a high-speed amphibious aircraft. Results showed that the maximum takeoff resistance increase occurred at around 70 percent of takeoff speed. In 6 ft waves, the takeoff resistance of the aircraft increased 65 percent over nominal values during calm seas. These results were very consistent over a range of dead-rise angles, which is the angle from the keel of the hull to its chine.

More experimental methods of water interaction have been explored such as the use of hydro-skis or hydrofoils. A supersonic amphibious aircraft, Seadart, was built using a pair of retractable hydro-skis by Convair San Diego for the United States Navy in 1951. As is discussed by Long [13], a test pilot in the Seadart program, there were five Seadart hulls built, with three of those hulls being tested over the course of five years. Tests of the first Seadart revealed

serious vibrations and loading on the aircraft created by the blunt aft-body of the skis as it crossed waves. In an attempt to reduce vibrations and loads, the twin skis were replaced by a single large ski but it was found to have unacceptable hydrodynamic stability and control characteristics. This was remedied by changing the ski shape and increasing the lateral deflection of the elevons, which gave the aircraft excellent hydrodynamic stability and control characteristics.

Research conducted by Fisher and Hoffman [14] looked at the calm- and rough-water landing and takeoff characteristics of a seaplane with a single retractable hydroski. The initial results found that the ratio of gross weight to maximum ski resistance was 3.2 with loads of 8 to 10g's in waves eight feet high. A yawing instability occurred just prior to the hydroski emerging from the water's surface. This was fixed by adding an afterbody extension to the ski, but this increased ski resistance and resulted in a reduced weight to resistance ratio of 2.9.

A hydrofoil is a second type of experimental water operations method and refers to the wing-like structure that is mounted on struts below the hull of a boat. It can be used to lift the boat partially or fully out of the water during forward motion. As the speed of the craft increases, the amount of lift that the hydrofoil produces increases to raise the hull partially out of the water, which greatly reduces the amount of drag and thusly allows for an increase in speed. The hydrofoil concept has also been applied to a number of amphibious aircraft (Figure 3).

Figure 3: Grumman JRF-5 with Grunberg Hydrofoil System [15]

As discussed by McKann, Blanchard and Pearson [16], a subsonic airfoil section shape performs well as a hydrofoil at low forward speeds. With a completely attached flow and while operating at equal Reynolds numbers, the forces and moments created in air and water are essentially identical for these foil types. A foil that operates at these conditions is often referred to as a "subcavitating" hydrofoil. At high speeds, the static pressure around the foil falls below the vapor pressure of water, which causes the water to evaporate around the foil and leads to the formation of water vapor bubbles. Ventilation can occur if the foil is surface-piercing, as air can be sucked down into the low pressure region. This two phase (liquid and gas) flow phenomenon is termed "cavitation" and when the entire upper surface of the hydrofoil is free of an attached flow, it is said to be "supercavitating". Supercavitating hydrofoil shapes have been developed for use at these high speeds where cavitation cannot be avoided. These hydrofoils are characterized by a sharp leading edge, usually having an entrance angle of about six degrees. The most common section shapes are: a plane faced wedge with a blunt trailing edge; an ogive shape, consisting of

convex circular arc surfaces with sharp leading and trailing edges; and a circular arc concave lower surface with a contoured upper surface. Examples of supercavitating hydrofoil shapes are shown in Figure 4.

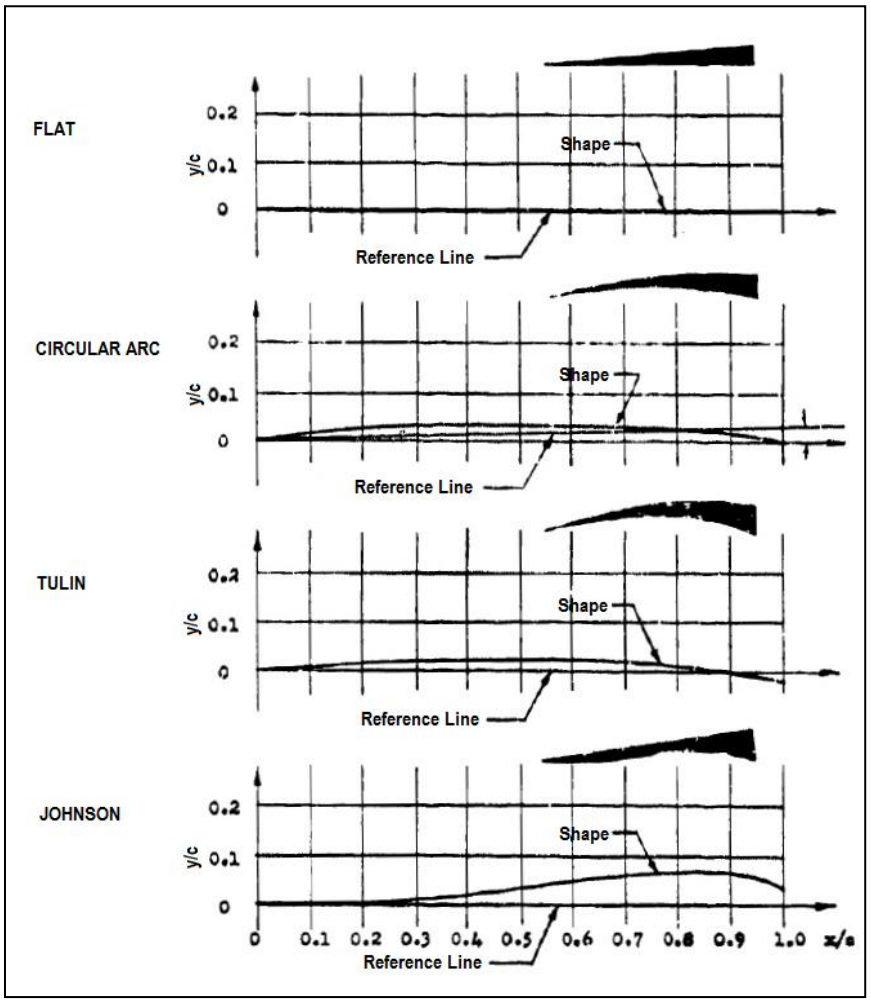

Figure 4: Supercavitating Hydrofoil Shapes [17]

Vagianos and Thurston [17] detail many different hydrofoil configurations that have been used, on both airborne and maritime platforms. The first and most common is the single hydrofoil system, which consists of one hydrofoil placed slightly ahead of the center of gravity of the aircraft. The single hydrofoil supports a predetermined design percentage of the gross weight of the vehicle at unporting. Unporting occurs when a hydrofoil breaks the water's surface. Additional stability in this configuration must be provided in addition to the foil;

such as the wing, tail or control surfaces of the airplane. The Grunberg system uses one main hydrofoil positioned behind the center of gravity while two small floats or hydroskis are placed at the front of the aircraft to provide necessary stability. In this configuration, the hydrofoil takes a majority of the design load, with the two smaller members being used primarily for stabilization. A tandem hydrofoil system consists of using two foil arrangements, one at the bow and one at the stern of the aircraft. At unporting, each hydrofoil array carries about 50 percent of the load. This arrangement is not practical for seaplane design due to the additional drag weight and cost compared to a single foil configuration. This arrangement develops undesirable lateral and longitudinal stability problems during unporting in heavy seas.

Some of the problems with the use of hydrofoils are detailed in Petrie's [18] report on the developmental and operational experiences with the United States Navy's first hydrofoil ship named "High Point". During the testing of the ship in 1961, it was found that there was cavitation damage in the aft propellers due to separation off the upper surface of the hydrofoil. Ventilation of the forward foil of the aircraft was also a problem while in large, short-crested waves. Ventilation of a hydrofoil occurs when part of the foil pierces the surface of the water and air is sucked down the lifting surface of the foil. This causes a drastic decrease in lift due to the density reduction from water to air. This ventilation issue was fixed by lengthening the forward strut to get the hydrofoil deeper into the water. This also led to an increased sea state capability for the craft.

2.3 Optimization Models

As the computational capacity of computers and the understanding of the physics involved in aerospace design have increased, the modeling of aircraft through optimization methods has become a powerful tool to aid in the development of new aircraft. As discussed by Jenkins and Hartfield [2], a variety of different algorithms have been proposed and used as optimizers and they can be broken down into two general categories: a stochastic and a direct methodology. A stochastic optimizer is a process that uses a non-deterministic approach to finding its solution, following a predictable pattern but with an element of randomness introduced. This allows for a greater chance of obtaining a globally optimized solution, as opposed to a solution that gets stuck on a local optimum. Types of stochastic optimizers include genetic algorithms (GA's) that are based on survival of the fittest principles, and particle swarm algorithms (PSO's), which are based on principles of social behavior. Direct solution techniques include pattern search algorithms (PS) and gradient-based optimizers, among others. More recently, hybrid optimizers have been developed that utilize a combination of optimizing algorithms to improve optimization efficiency for a range of problems.

A genetic algorithm uses a probabilistic methodology for optimization, primarily based on survival of the fittest principles. Genetic algorithms were initially developed based on principles from John Holland's book, "Adaptation in Natural and Artificial Systems" [19]. A population of potential solution candidates is created, with each candidate possessing a fitness and a chromosome. The chromosomes are composed of genes which are GA variables set in the input file. To create a new population, certain individual members are chosen according to their fitness to create an offspring based on a tournament

style selection process. The "weaker" solutions are killed off, while the "stronger" solutions go on to "reproduce" and "mutate" using various crossover routines to produce new generations of offspring solutions. Genetic algorithms have been shown to be very effective and robust for a wide range of optimization problems. For example, Obayashi, Yamaguchi and Nakamura [20] employed a genetic algorithm in designing a transonic wing planform shape; research conducted by Vicini and Quagliarella [21] utilized a genetic algorithm to optimize airfoil selection for a given aircraft; and Crossley and Laananen [22] preformed a conceptual design of a helicopter via the use of a genetic algorithm. The GA's superior effectiveness stems from its ability to find optimums in a design space with a fairly large number of variables, and also its ability to operate in design spaces that are not necessarily smooth and continuous. This makes the use of genetic algorithms ideal for complex engineering problems. The downside of the use of a GA is that it takes many more evaluations of the objective function than a direct search method, such as a gradient-based optimizer or pattern search.

Particle swarm optimization is a population-based, stochastic algorithm originally developed by Kennedy and Eberhard [23] in 1995. PSO is based around a type of swarm intelligence modeled after human social interaction. The algorithm begins by generating a population of randomly chosen members defined by a set of independent parameters. Each particle moves through the possible solution space with some velocity, and seeks a globally optimized position by changing its given parameters in accordance with a specified set of rules. The particles are allowed to interact with neighboring particles, mimicking the social behavior of a group of individuals collectively seeking a common goal. Each particle has two or three rudimentary reasoning capabilities: memory of its

own best position, knowledge of its local neighborhood's best position and/or knowledge of the entire population's best position. Individual particles communicate desirable positions on the solution space to each other and adjust their own position and velocity based on these good positions. An objective function is usually set, which allows these desirable positions to be evaluated to determine which produces the most favorable performance characteristics. Repulsive Particle Swarm Optimization (RPSO) is a variation of the standard PSO in which a repulsive force is introduced between particles to attempt to ensure particles will not get caught in local minima or maxima. This prevents premature convergence and increases the chance of finding a globally optimum solution. A modification was made by Mishra [24] to the RPSO which allowed each particle an opportunity to pause and search its immediate surroundings for a possible better solution before continuing on in the more generalized swarm search.

A pattern search algorithm is a direct optimizing technique proposed by Hooke and Jeeves [25] in 1961. This algorithm works by first selecting an initial trial case. Exploratory moves are made, varying each individual parameter in a systematic manner while holding all other parameters constant. After each individual change the objective function is reevaluated but not changed. For example, if, in a maximization problem, the change increases the objective function, then the value of the parameter is set to the modified value. The other parameters are modified in turn. If all the parameters have undergone exploratory moves and the objective function is increased, then the variables are changed simultaneously in a pattern move. If the pattern move does not lead to an increase in the objective function, the sizes of the exploratory moves are reduced and the process is repeated. One of the greatest strengths of the pattern

search algorithm is that it is relatively efficient at finding local optimums if it is well positioned in the possible solution space. One of the greatest weaknesses of the pattern search is that it requires a well chosen initial guess to be effective, particularly in a solution space that is computationally discontinuous.

The gradient method is a first order optimization algorithm. Hasdorff [26] describes multiple methods of using gradient optimization to find a local minimum; with the most popular being the method of steepest descent and the method of conjugate descent.

The method of steepest descent is an algorithm for finding the nearest local minimum of a function. This method presupposes that the gradient of the function can be computed. The gradient of a function with n variables is

$$\nabla f = \left(\frac{\partial f}{\partial x_1}, \ldots, \frac{\partial f}{\partial x_n}\right) \tag{2.3}$$

An initial guess is made at point P_0, and a sequence is then constructed P_0, P_1, P_2,… such that:

$$f(P_{i+1}) < f(P_i) \tag{2.4}$$

This sequence is found by propagating the from P_i to P_{i+1} along a line extending from P_i in the direction of $-\nabla f(P_i)$, which is the local downhill gradient and is recalculated at each step. The next point in the sequence is found using

$$P_{i+1} = P_i - \gamma_i \nabla f(P_i) \tag{2.5}$$

where γ is the step size, which is allowed to change each iteration. The search slides down the gradient until it converges on a solution, which is where the directional derivative is equal to 0. One of the downsides of the use of the steepest descent method is that if the function has a long, narrow valley shape, the minimum can take a significant amount of iterations to find.

The drawbacks of the steepest descent method are addressed through the use of the conjugate descent method, which, instead of using the local gradient of a function to go downhill to a minimum, conjugate directions are used. Two vectors, v and u, are said to be conjugate with respect to A if:

$$u^T A v = 0 \tag{2.6}$$

In other words, u and v are conjugates if they are orthogonal with respect to A. As with the steepest descent method, an initial guess P_0 is made. For each iteration of the conjugate descent method, a metric must be in place to determine if the search is converging toward a local minimum. This metric comes about through the fact that P*, the unknown local minimum, is also the unique minimizer of the following quadratic function:

$$f(P) = \frac{1}{2} P^T A P - P^T b \tag{2.7}$$

This means that if f(P) becomes smaller after an iteration, the search is converging toward P*. Next, the first basis vector, v_1, is taken to be the negative of the gradient of f at P_0. This gradient is equal to AP_0-b. The other vectors in the basis will be conjugate to the gradient. Next, let r_n be the residual at the nth step in the iteration.

$$r_n = b - A P_n \tag{2.8}$$

Here, r_n is the negative of the gradient at P_n, so if the gradient descent method was being used, the search would move in the direction of r_n. Instead, for the conjugate descent method, it is insisted that the directions, v_n, be conjugate to each other. The method also requires that the next search direction be found from a combination of the current residual and all the other previous search directions. This gives the expression for the next search vector:

$$v_{n+1} = r_n - \sum_{i \le n} \frac{v_i^T A r_n}{v_i^T A v_i} v_i \tag{2.9}$$

Following this direction, the next optimal location is given by:

$$P_{n+1} = P_n + \alpha_{n+1} v_{n+1} \tag{2.10}$$

where

$$\alpha_{n+1} = \frac{v_{n+1}^T r_n}{v_{n+1}^T A v_{n+1}} \tag{2.11}$$

This iterative process will continue until a local minimum value is reached. The conjugate descent method is used at a slight cost in calculation time per iterative step when compared to the steepest descent method, but the number of iterations needed to converge on a minimum value is much less.

There have been a number of different combinations of optimizing methods employed together in the form of a hybrid optimizer in an effort to more quickly and efficiently arrive at a globally optimum solution to various engineering problems. Jenkins and Hartfield [2] have made use of a hybrid particle swarm-pattern search optimizer in rocket motor optimization problems. The hybrid optimizer makes use of the pattern search technique's ability to quickly find a local optimum in a limited solution space, while using the particle swarm as a transport mechanism for the pattern search particles. A random population of particles is created, with initial particle velocities and positions being defined. The particle swarm calculations then determine new particle positions and fitness. A pattern search is initiated, followed by a check to see if the swarm has been improved. The particle swarm then calculates new particle positions and the cycle repeats itself. Since the particle swarm is non-elitist, the combined hybrid optimizer can examine a very large number of possible solutions, leading to a greater chance of finding a globally optimum solution to a problem. This

method also, perhaps just as importantly, is capable of finding many near-optimum solutions to a given problem, increasing its usefulness as a design tool.

2.4 Wind Tunnels

While there have been large advances in theoretical and computational methods, low-speed wind tunnel testing is still essential for obtaining the full range of data necessary to guide design decisions for many practical engineering applications. In aerospace applications, wind tunnel results provide experimental data on the lift and drag of a model, as well as roll, pitch and yaw moments, from which stability derivates, as well as the location of the neutral point, can be found.

One of the most important concepts for relating wind tunnel results to theoretical and computational models is that of similar flows. Usually, it is not economically feasible to perform wind tunnel tests on a full size model, so scaling factors must be introduced. The goal of the scaling process should be to produce a model that is dynamically similar to the unscaled aircraft. Anderson [27] describes two flows as being dynamically similar if: bodies in both flows are geometrically similar, and the similarity parameters, which in aerospace applications are Mach number and Reynolds number, for both flows are the same. Having dynamically similar flows is important because lift, drag and moment coefficients will be identical for two geometrically similar bodies in these flows. This means that the aerodynamic coefficients measured during wind tunnel testing will be the same as the aerodynamic coefficients for the full scale model at the same Mach and Reynolds numbers. It is often not practical to obtain full scale Reynolds numbers on a scale model due to limitations of some

wind tunnel's operating speeds. The Reynolds number can be matched by increasing speed, but the Mach number will now be incorrect. This problem can be overcome through the use of a variable density tunnel (VDT), which was first developed by NACA [28] in 1929, and can be used to match Reynolds and Mach numbers through tunnel pressurization. Unfortunately, most wind tunnels are not capable of pressurization and are therefore not capable of achieving a dynamically similar flow when scaling down from a full scale model. In these instances, corrections can be applied through scaling corrections, as described by Barlow, Rae and Pope [29]. First, a plot of C_D vs C_L is made from the wind tunnel data. Next, the induced drag coefficient is calculated using the following equation.

$$C_{D,i} = \frac{C_L^2}{\pi AR} \tag{2.13}$$

The induced drag coefficient is then subtracted from total drag coefficient to give the profile drag coefficient, $C_{D,0}$. $C_{D,0}$ is then corrected for the change in Reynolds number from model scale to full-scale using Figure 5.

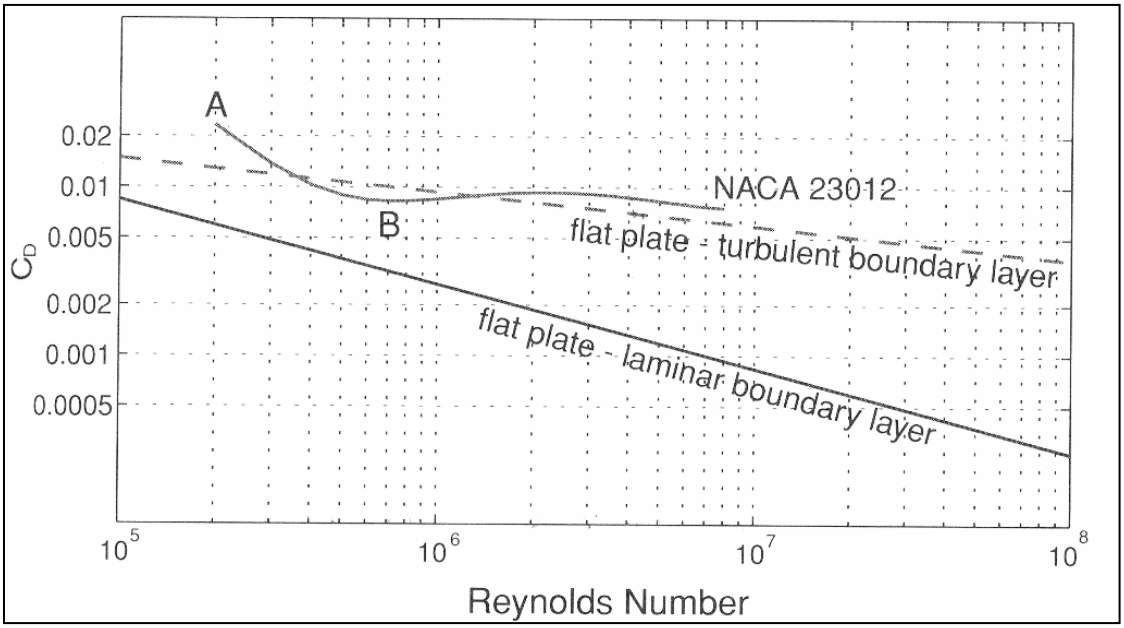

Figure 5: Reynolds Number Correction Chart [29]

This step is considered to be relatively controversial, as some engineers believe that manufacturing defects on the actual aircraft can cause an increase in drag as great as the drag reduction due to Reynolds number scaling from model scale to full-scale. For the purposes of this research, the correction was used as we are looking to see the theoretical accuracy of the sizing code compared to the wind tunnel results, and the sizing code does not take into account any manufacturing defects. The correction factor is the difference in C_D value between the tunnel Reynolds number and the Reynolds number for the wing of the full-scale aircraft. This correction factor is subtracted from the tunnel profile drag coefficient to bring it to full-scale. The lift induced drag is then added back in to find the total drag at full-scale Reynolds number. The zero lift drag coefficient, C_{D0} can then be used to find the drag area. This scaling correction method allows wind tunnel drag results to be scaled up to flight condition Mach and Reynolds numbers.

There are a number of factors that lead to incorrect correlation between wind tunnel data and any flight test. Collected tunnel data will suffer from an inexact or unknown Reynolds number, boundary layer effects, interference and wall effects, simulation of flow through engine nacelles, etc. Flight test data will suffer from piloting irregularities, gust interference, and errors in the center of gravity location just to name a few.

The largest boundary layer effect that influences the accuracy of wind tunnel results is the improper transition location from a laminar to turbulent boundary layer. Usually the transition is delayed due to the smaller lengths involved on the scale model. Turbulent boundary layers have much greater associated skin friction than their laminar counterparts, so by delaying transition, drag estimations can be thrown off. While there is a higher drag associated with turbulent flows, there is far less energy in laminar flows, which makes it more

susceptible to roughness or corners and can lead to premature separation of the boundary layer. This leads to a loss of lift and an increase in drag on the model. Both of these examples of boundary layer effects cause error between wind tunnel results and computational or flight test results. One way of mitigating these effects, which is explored by Braslow, Hicks and Harris [30], is through the use of grit-type boundary layer transition trips. When applied correctly, these are intended to fix the boundary layer transition location. Incorrect application, such as the transition strip protruding too high above the surface of the model, can result in undesirable effects, which can include additional drag or possibly robbing the newly created turbulent boundary layer of energy and leading to premature separation. Transition trip location can vary depending on the type of airfoil being used. As documented by Holmes and Obara [31], on a NACA four or five digit airfoil, transition will occur at approximately 10% chord at cruise conditions. Newer, laminar flow airfoils can transition much later, at nearly 60% chord.

Another issue is that of wall interference and blockage. The presence of tunnel walls reduces the area through which the air must flow around the model compared to free-air conditions. This, in accordance with Bernoulli's equation, means that the velocity of the air in the vicinity of the model will be increased in comparison to a free-air velocity, leading to errors in wind tunnel results. Wake blockage is also a problem present in wind tunnel testing. Any model without some type of suction-type boundary layer control will generate a wake that will have an average velocity that is lower than that of the free stream. To maintain a constant volumetric flow rate, the velocity outside the wake in a closed tunnel must increase to make up for the decreased velocity inside the wake. This higher velocity means a lower pressure by Bernoulli's principle, and this lower pressure,

which arises as the boundary layer (which later becomes the wake) grows on the model, puts the model in a pressure gradient. Research conducted by Thom [32] shows viable mathematical methods for correcting velocities in wind tunnels due to blockage effects.

Flow visualization techniques are also a powerful tool for analyzing the flow over a model. Using flow visualization, it is possible to see stagnation points as well as areas of separation on a model, and this information can be used to reduce drag by correcting any aerodynamically problematic areas of the design. Many flow visualization techniques are in practice today, with each having specific pros and cons. For the purposes of this research, dye, smoke, and oil visualization techniques are the primary methods considered.

The observation of fluid motion using smoke and dye is one of the oldest visualization techniques in fluid mechanics. It is relatively inexpensive and easy to implement, while still giving great insight into the complex phenomena occurring in fluid flows. Smits and Lim [33] describe multiple methods of using various dyes to perform flow visualization in a water tunnel. Generally a suitable dye has to meet three requirements: neutrally buoyancy, high stability against mixing and good visibility. The most popular dyes are conventional food dye, milk and fluorescent dye. Most commonly, the dye of choice is introduced into the flow upstream of the model through a probe, usually constructed out of a hypodermic needle or stainless steel tube approximately 1.5 to 2 mm in diameter. The greatest drawback of this method of injection is the disturbance this can cause to the flow field. This is usually countered by placing the probe significantly upstream to minimize these effects. Dye ports in the model are another common method of dye injection (Figure 6). When using dye ports, it is

important to keep the exit velocity to a minimum so as to disturb the flow as little as possible.

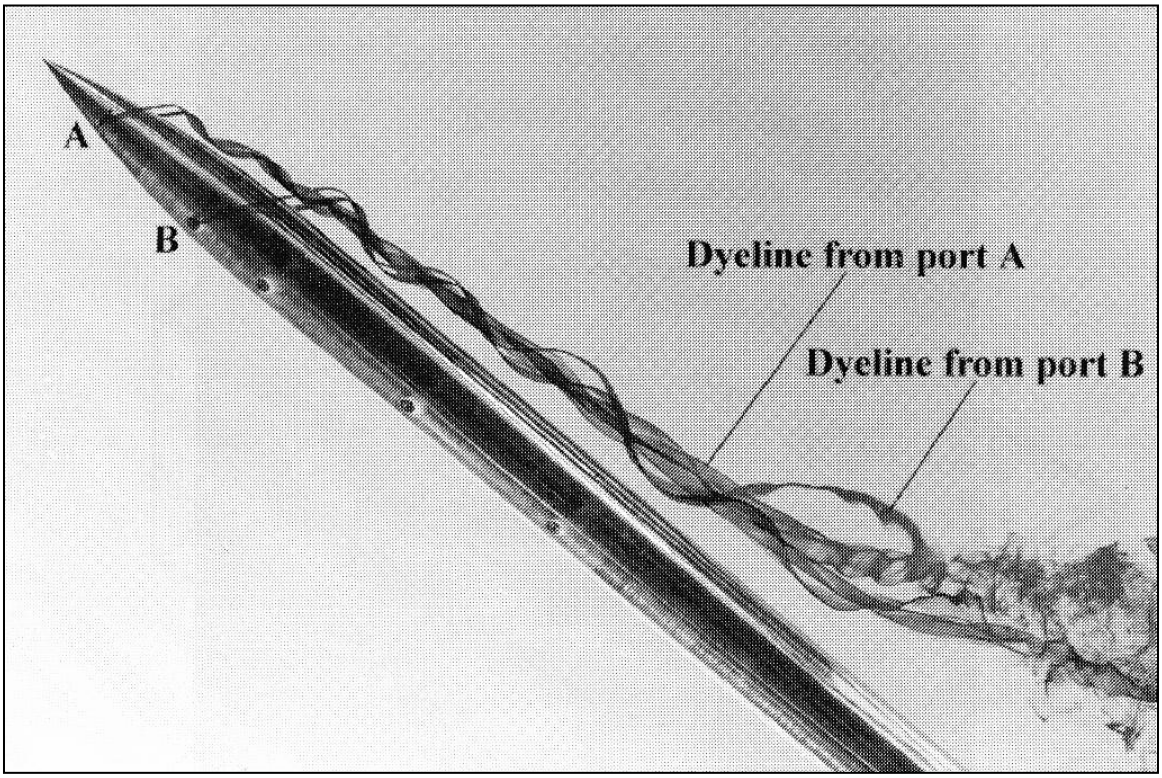

Figure 6: Dye lines and Injection Ports in a Water Tunnel [33]

The principle of visualizing the flow over a model in a wind tunnel is the same, in principle, as the visualization in a water tunnel using a dye, as detailed by Merzkirch [34]. A number of different "smokes" can be injected into the flow well upstream of the test section. These "smokes" can include steam, aerosols, and tracer gases, which leave a residue on the surface and become visible under special optical conditions. The "smoke" has to be of a gaseous nature in order to maintain neutral buoyancy in air, with only the tracer particles being significantly denser than air. The solid or liquid particles normally have a diameter less than 1 μm, which makes the buoyancy effects practically negligible. Also, at the related low particle Reynolds numbers, the drag force, which acts in

the vertical direction, is very high and almost balances the force of gravity which basically suspends the particles in the flow.

Lastly, oils can be used to visualize surface flows. The oil is usually spread onto the areas of interest with a paint brush before the wind tunnel is turned on. It will then flow under the influence of shear stress from the airstream and gravity. Because the surfaces of interest are usually inclined in some fashion, the oil mixture must have sufficient viscosity to sufficiently resist the influence of gravity. The most common material for oil flow visualization is a petroleum based lubricating oil. It is important to have the color of the oil mixture contrast with the color of the model surface. One popular way of doing this is by adding fluorescent dye to the oil and using an ultraviolet light to illuminate flow (Figure 7). Oil can also be made white by mixing titanium dioxide into it. This approach is best used on a black surface and removes the need to install and use black lights to illuminate the flow. Photographs can be taken after the flow is turned off but the available time is relatively short because the oil will flow just under the influence of gravity [29].

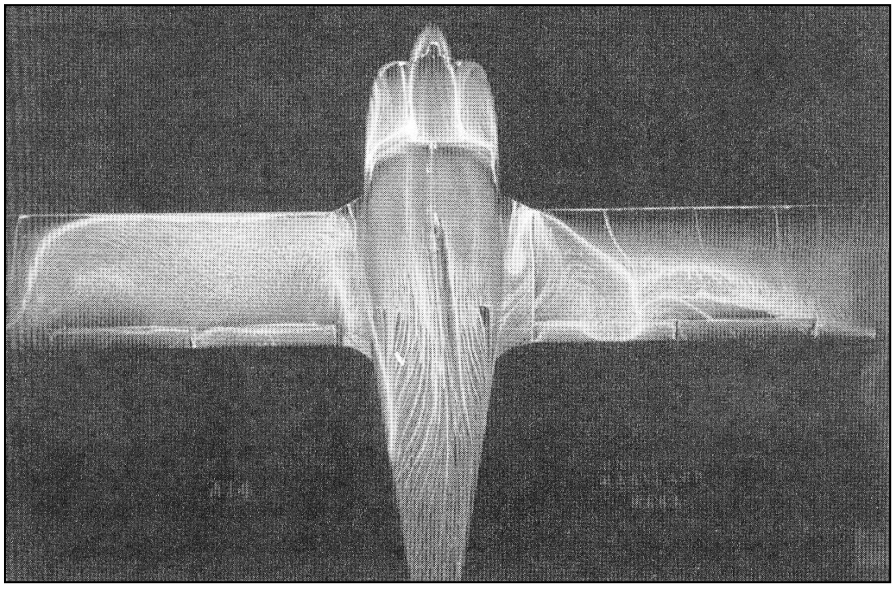

Figure 7: Oil Visualization Technique [29]

Chapter 3

Sizing Code Development and Validation

3.1 Development

3.1.1 Introduction

A code was developed in MATLAB to size and predict performance characteristics for an amphibious aircraft. When given required input parameters, such as a mission profile, wing aspect ratio, taper ratio, tail volume coefficients, fuselage fineness ratio, etc., the code outputs all major aircraft component geometries, fuel and component weight estimations, center of gravity and neutral point locations, component drag estimates, and mission performance characteristics.

The sizing code is set up to work with a number of different aircraft configurations. The designer has the choice of using a conventional, canard or flying wing aircraft configuration. Also, multiple methods of water operation can be used in the code, which lets the designer compare the impacts a specific type of water operation method will have on the performance and weight of the amphibious aircraft. The code can be configured to analyze the aircraft using a boat hull, twin floats, a hydrofoil, sponsons, or wing-tip floats. Often times, amphibious aircraft are designed with a combination of the above water operation methods, such as a boat hull being used with the addition of wing-tip floats or sponsons to increase lateral stability, or the addition of a hydrofoil to any configuration to decrease the load on the airplane as it approaches takeoff speed. To increase the usefulness of the sizing code, as well as to obtain a more feasible final preliminary design, any combination of the various water operations methods may be used, which allows for testing as many

configurations as possible. Additionally, the code allows the designer a choice on where the aircraft's fuel will be stored, either located at the center of gravity or stored in the wings, as well as the option for the use of strut-braced wings.

The sizing code functions by inputting an initial takeoff gross weight estimate for the aircraft, as well as certain geometry inputs. The code is then put into a while loop, where it compares the difference between the initial gross weight estimate and the gross weight calculated based on aircraft geometry and performance characteristics. Initially, the gross weight estimate and geometric input parameters are used to size the major components of the aircraft (main wing, horizontal and vertical tails, water operations method). With the components sized, the drag on individual components is calculated during different mission legs, such as cruise in and out as well as time spent in ground effect. These drag estimates are then used to determine fuel consumption which leads to a component-by-component weight build up of the vehicle. The code then checks to see if the calculated gross weight is within a specified difference margin to the initially estimated gross weight, in the case of this paper 0.1 lb. If the calculated value is within this margin, the aircraft sizing is considered to be at a converged solution and the while loop terminates. If the difference between the estimated and calculated value is greater than the difference threshold, the initial gross weight estimate is overwritten by the calculated gross weight estimate and the sizing code iterates until a converged solution is found.

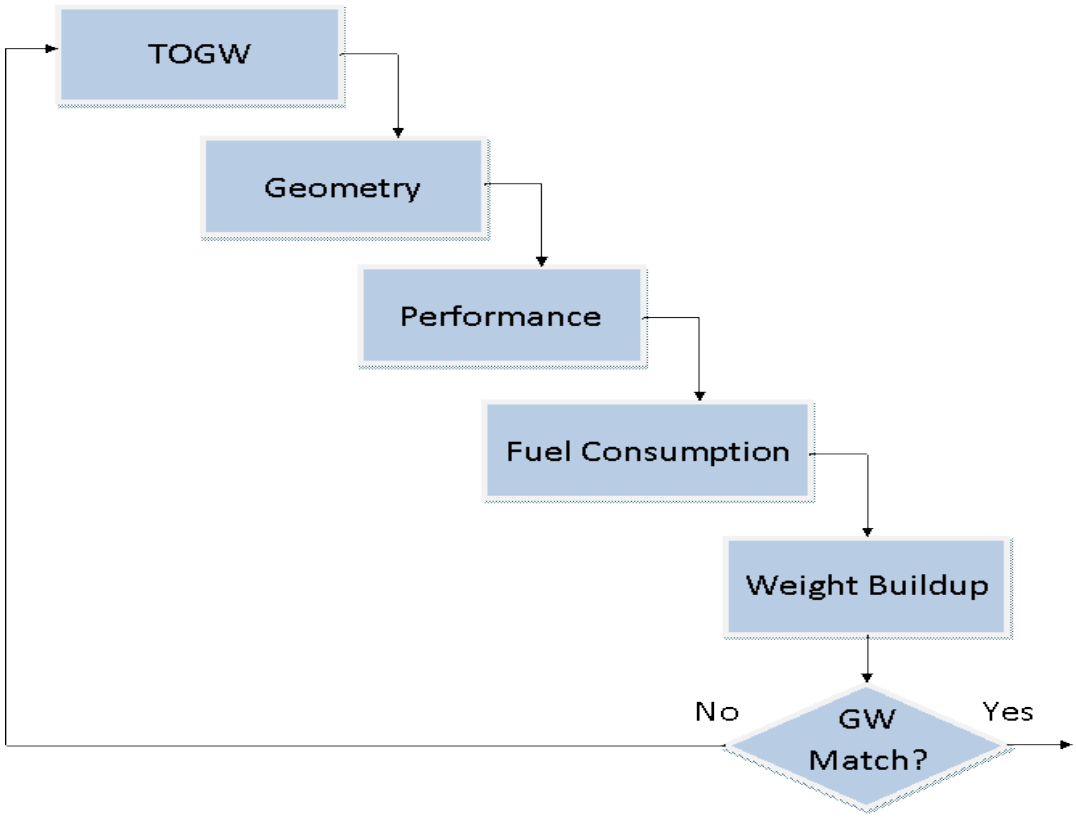

Figure 8: Sizing Code Flowchart

With the aircraft sized, individual component weights are sent to functions which calculate the center of gravity and neutral point of the aircraft. With these parameters, a static margin can be calculated. Aircraft geometry and performance characteristics are then output into a text file and a picture showing the basic geometry is drawn.

3.1.2 Lifting Surface Geometry Calculations

With an initial gross takeoff weight estimation, as well as various input parameters, the next step in the sizing process is to size the major components of the aircraft. First, the wing loading of the aircraft is calculated using an initial estimate of the maximum lift coefficient, C_{Lmax}, and the stall speed.

$$\frac{W}{S} = \frac{1}{2}\rho_{air} V_{Stall}^2 C_{Lmax} \tag{3.1}$$

Now the required planform area of the main wing, S, can be calculated using the estimated gross takeoff weight and wing loading.

$$S = \frac{W_{est}}{(W/S)} \tag{3.2}$$

The total wing span, b, of the main wing can be found using Equation 3.3,

$$b = \sqrt{S\,AR} \tag{3.3}$$

where AR is the aspect ratio of the main wing.

The main wing is divided into an inboard and outboard section to allow for maximum flexibility in determining the shape of the wing. Both sections are allowed to have distinct sweep angles and taper ratios. Also, the width of the inboard wing segment, to be called the wing segment width (WSW) for the remainder of this paper, is not permanently fixed. As the sizing code iterates through in an attempt to converge on a correct gross takeoff weight, the WSW is driven by with the volume of fuel the aircraft requires, as it is to be carried only in the inboard section between 30% and 65% of the local chord length. The root chord length for conventional and canard configurations is calculated using Equation 3.4,

$$C_{r,inboard} = \frac{2S}{(b\ WSW(1+\lambda_{inboard})) + (b - WSW\ b)\lambda_{inboard}(1+\lambda_{outobard})} \tag{3.4}$$

where λ is the taper ratio for the inboard and outboard wing section, which are both inputs, as noted in the subscript. With the inboard chord length now known along with the inboard and outboard taper ratios, the chord length at the separation between wing segments as well as at the tip of the wing can be found.

$$C_t = C_r\lambda \tag{3.5}$$

The final geometric calculation for the main wing is to determine sweep angles at the leading and trailing edge. There is an input for the sizing code that allows the designer to choose a sweep angle at a specific percentage of the wing chord length, but to find the sweep angle for various locations on the wing Equation 3.6 must be used,

$$\Lambda_{x2} = \tan^{-1}\frac{(x_2 C_r + b_{wsw}\tan(\Lambda_{x1}) - x_1 C_t + x_2 C_t) - (x_2 C_r)}{b_{wsw}} \tag{3.6}$$

where x_1 is the input sweep angle position, x_2 is the position along the chord where the sweep angle is being calculated, Λ is the sweep angle of x_1 and x_2 as noted. b_{wsw} is the semi-span of the inboard wing section length and C_r and C_t are the root and tip chord lengths of the inboard or outboard section, depending on what portion of the wing the sweep angle is being calculated for.

The planform areas for the vertical and horizontal tails are calculated using the following equations referenced from Raymer [3],

$$S_{VT} = \frac{c_{VT} b S}{L_{VT}} \tag{3.7}$$

$$S_{HT} = \frac{c_{HT} \bar{c} S}{L_{HT}} \tag{3.8}$$

where, C_{VT} and C_{HT} are tail volume coefficients for the vertical and horizontal tail respectively, L_{VT} and L_{HT} are moment arms for the vertical and horizontal tail respectively, which can be approximated as the distance between the tail quarter-chord to the quarter-chord of the main wing. The mean chord length is given by $\bar{c}$. The span and root chord length of the tails are found using Equations 3.7 and 3.8 using terms for the respective tail instead of the main wing.

3.1.3 Water Operation Method Geometry Calculations

The sizing code allows for the design of an amphibious aircraft using a wide variety of water operation methods. It can calculate the geometry and resulting effects on the performance of the aircraft due to a boat hull, twin floats, wing tip floats, sponsons or a hydrofoil. In order to maintain maximum flexibility in the code, it was designed to allow multiple methods to be chosen simultaneously. For example, most amphibious aircraft that make use of the boat hull configuration also use either wing-tip floats or sponsons to increase the stability of the vehicle during its time on the surface of the water at the expense of aerodynamic performance. Each method of water operation is sized and analyzed separately to properly capture the performance impact on the aircraft.

3.1.3.1 Boat Hull Calculations

The primary factors that affect the shape of any float or hull on an aircraft are those that concern how it behaves in the water, with aerodynamic considerations, to a large extent, being secondary. For instance, early examples of floats had difficulty taking-off from the surface of the water. This problem was fixed through the addition of a step on the float, which causes water to separate from the aft end of the float and significantly reduce resistance through the water, although it negatively impacts performance in the air.

The primary functions of any float or hull is to give the amphibious aircraft buoyancy, and to provide longitudinal and transverse stability on the water and when underway to takeoff speeds. The float must provide reasonable resistance while in the water so that the aircraft is capable of taking-off with the power it has available. It must also be designed in such a way so as to hold landing

impact pressures to reasonable levels. All of these factors can drastically change the form of floats, but for the purpose of this study, many of the design details are out of scope for a preliminary design and will be omitted until the sizing of the aircraft is complete. The floats can then be designed in more detail, taking into account the specific characteristics of the resulting aircraft and how those characteristics will drive the design of the float.

For the purpose of this sizing code, the guidelines for the design of a boat hull set out by Shoemaker and Parkinson [35] were used for initial sizing calculations. Initially, a load coefficient, C_{Δ}, for the hull is given. This coefficient will determine the beam, b, of the hull. A seaplane experiences the greatest amount of water resistance at hump speed, which is the speed just before it begins to plane on the step of its float structure. In Figure 9, hump speed corresponds to the velocity coefficient of 2.3. For this study, the load coefficient was taken to be 0.425, which corresponds to the highest load coefficient on the C_V=2.3 curve. The negative slope of this curve indicates that decreasing the beam of the float will lead to an increase in resistance. Alternatively, the curves for C_V values of 4.5 and 6.0 show that reducing the beam will reduce the water resistance of the aircraft. According to Langley [36], the practical range of load coefficients for boat hulls is between 0.35 and 0.5.

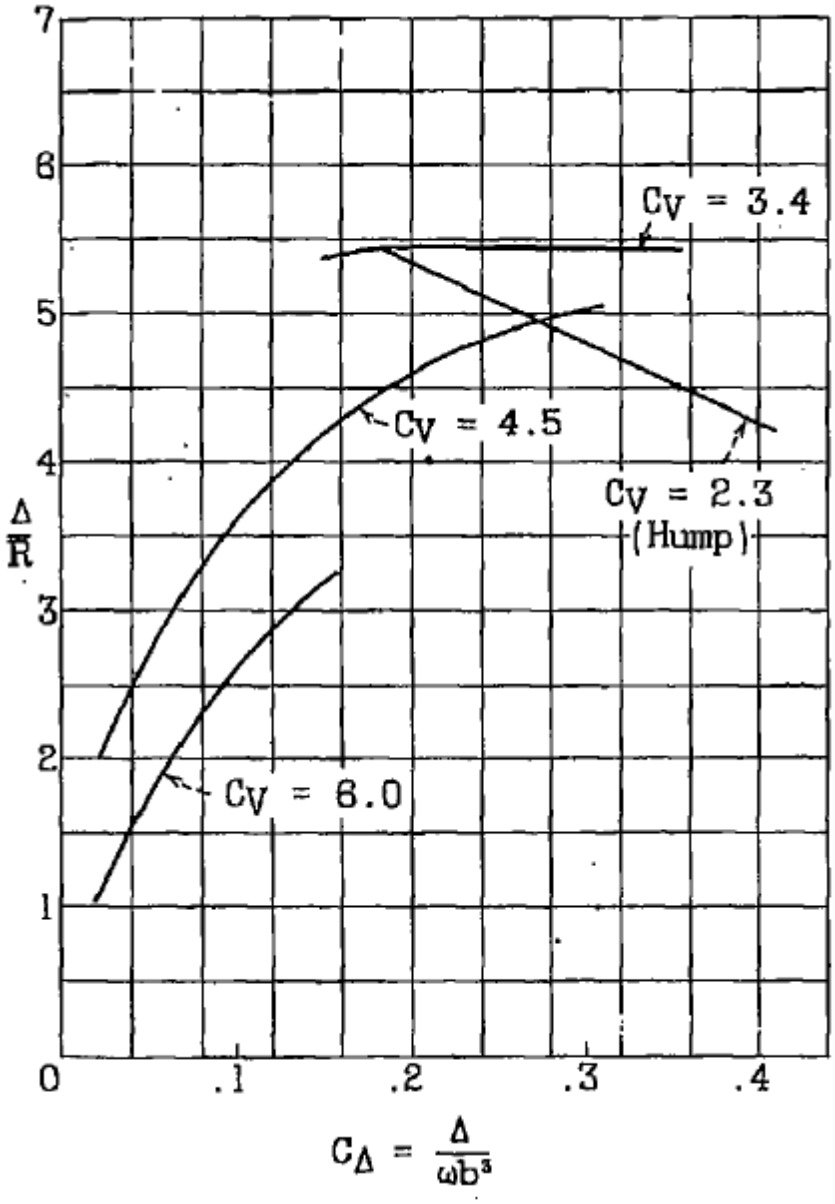

Figure 9: Effect of C_Δ onΔ/R at Best Trim Angles [35]

Next, the beam of the hull is calculated based on the load coefficient and weight of the aircraft.

$$b_{hull} = \sqrt[3]{\frac{W_{est}}{C_\Delta \rho_{water}}} \tag{3.9}$$

For the analysis performed in this study, the hull height was assumed to be equal to the hull beam. The necessary displacement of the hull was then calculated,

with a 100% reserve factor, meaning that the hull will displace twice its weight in water. A length-to-beam ratio, which varies between 3.5 for aircraft below 5,000 lb. to 4.5 for aircraft above 20,000 lb. is then input, and interpolation is used to find values in between. Generally, a lower length-to-beam ratio will result in a lower water resistance in the high speed range as well as a lower structural weight. Often times, however, the shorter beam can lead to excessive spray [35] and reduce the transversal stability of the aircraft on water. The length of the boat hull is calculated using Equation 3.10.

$$L_{hull} = \frac{R_{LB} D_{hull}}{b_{hull}^2} \tag{3.10}$$

Where R_{LB} is the length-to-beam ratio and D_{hull} is the displacement of the boat hull. The length of the boat hull is then compared to the minimum fuselage length set by the designer and the program continues. A hull of this length, width and height will now be used when doing drag calculations to determine the performance of a boat-hulled aircraft.

3.1.3.2 Twin Float Calculations

The design of floats for a twin float aircraft is very similar to the design of an amphibious aircraft that makes use of a boat hull. Once again buoyancy, stability, clean running and good takeoff properties are desirable hydrodynamic features, but these features are largely incompatible with desirable aerodynamic features, such as having a low drag shape, and the minimum size and weight possible. Unlike the boat hull, the twin float configuration must have 80% reserve buoyancy [37], meaning that the water displacement of each float must be equal to 90% of the gross takeoff weight of the aircraft. In the case of twin floats, having a wide cross section is not as important as with a boat hull

configuration, as having two floats with a wide base track will increase transverse stability.

The sizing code first calculates the required individual float displacement, which by regulation must be equal to 90% of the fully loaded takeoff weight.

$$D_{float} = 0.9 \frac{W_{est}}{\rho_{water}} \tag{3.11}$$

Next the proportions and dimensions of the float can be found since the total submerged float displacement has been fixed. A block coefficient for the float is assumed to be 0.5. The block coefficient is the ratio of the volume the float to the volume of a rectangular block with the same length, depth and breadth. For most Vee-bottom floats, which is the standard configuration used on most amphibious aircraft, the block coefficient is between 0.48 and 0.52. The breadth of a float can be found using Equation 3.12.

$$b_{float} = \sqrt[3]{\frac{D_{float}}{9C_{block}}} \tag{3.12}$$

C_{block} is the float's block coefficient, b_{float} is the breadth of the float, and D_{float} is the float displacement and has units of ft^3. Langley also offers guidelines for finding the length and depth of the float as a function of breadth based on historical ratios to obtain a float that has sufficient longitudinal stability. The length of the float should be eight times the breadth while the depth should be 1.125 times the breadth [36]. These factors are then used by the sizing code to find the appropriate length and depth of the float based on the gross takeoff weight. Two floats are then used by the performance section of the sizing code for drag calculations.

3.1.3.3 Wing Tip Float and Sponsons Calculations

Most amphibious aircraft that use a boat hull as their primary water operation method must augment their transverse stability through auxiliary means. To properly understand the reason for this lack of transverse stability, it is necessary to explain the concept of the transverse metacenter.

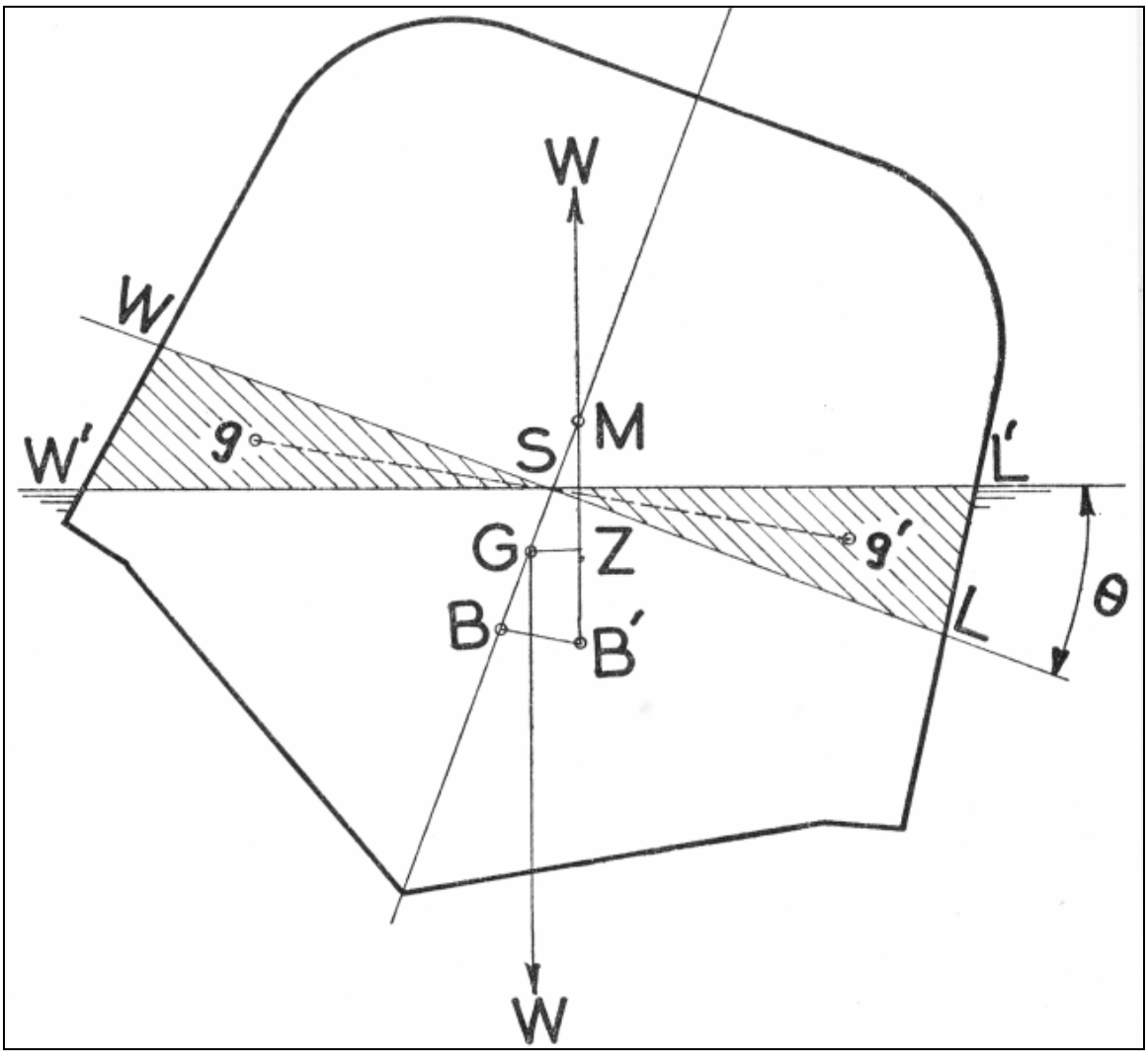

Figure 10: Transverse Metacentric Height [36]

In this figure, the center of gravity of the hull is located at point G. The center of buoyancy is located at point B. The center of buoyancy of a hull is located at the center of gravity of the water a hull displaces. The hull is heeled through a small

angle, θ, so that the water line moves from WL to W'L'. This causes the center of buoyancy to move from point B to point B' while the center of gravity stays at point G. If a vertical line is drawn through point B', the transverse metacenter is located at the intersection point between that line and the centerline of the hull. The transverse metacentric height is the distance between the center of gravity and the transverse metacenter. If the metacenter is above the center of gravity, the aircraft is stable. If the metacenter coincides with the CG, the aircraft is in neutral stability. If the metacenter is below the CG, the aircraft is unstable.

The reason that a flying boat's hull is normally augmented for transverse stability is because, in practice, it is basically impossible to achieve positive transverse stability due to the center of gravity almost always being above the transverse metacenter. Since the majority of the structure of a flying boat is above the load water line, the center of gravity will be significantly higher than the load water line. Furthermore, the metacenter is normally relatively low because of the limits to the value of the transverse moment of inertia, I, of the boat hull at the load water line. I is a function of the beam of the hull, which could be increased to give the aircraft sufficient transverse stability by lifting the metacenter above the center of gravity, but this would lead to very undesirable effects while on the water, namely a large increase in water resistance, making it increasingly difficult to takeoff.

Two methods are normally used to increase the transverse stability of a boat plane without the drastic measure of greatly increasing the beam. There will usually be either outboard wing-tip floats mounted on either side of the fuselage (Figure 11) or sponsons (Figure 12) built off the side of the hull.

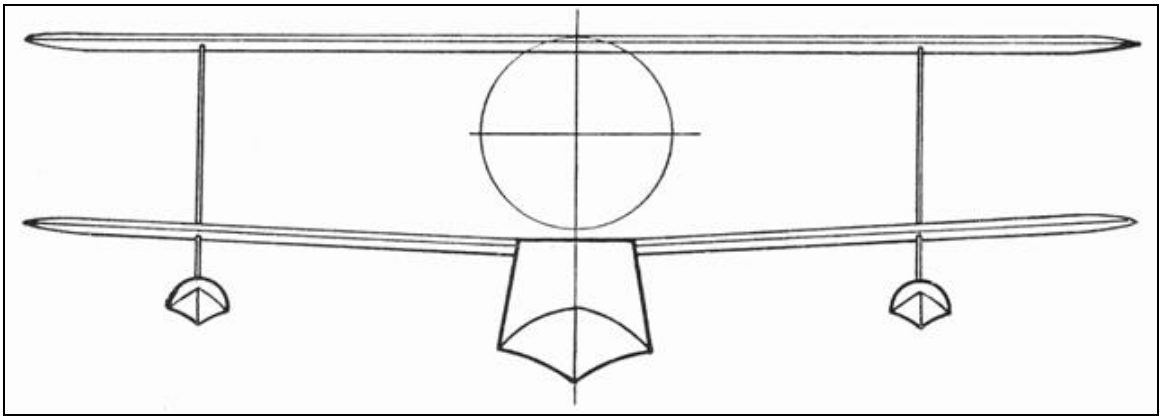

Figure 11: Wing-Tip Floats [36]

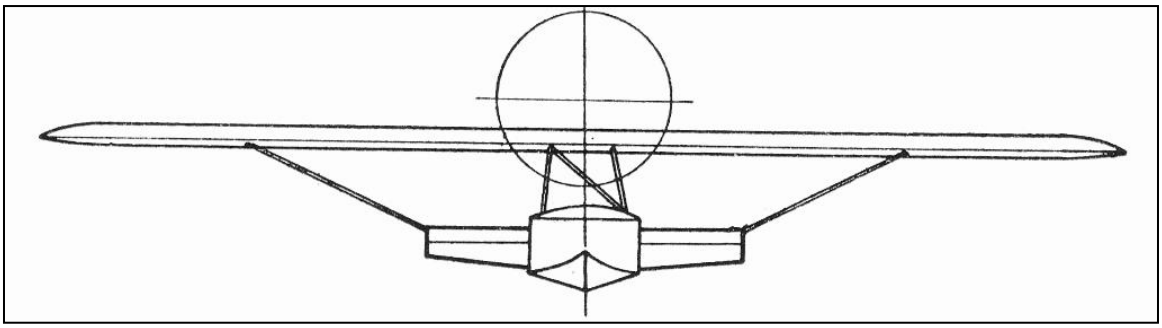

Figure 12: Sponsons [36]

Both methods provide lateral stability to the aircraft in the event of any heeling rotations.

Wing-tip floats and sponsons are designed by the same method. The Federal Aviation Administration [37] has specified a required buoyancy for any lateral stabilizing floats by mandating that the righting moment provided by a float when fully submerged be greater than,

$$M = RW_{est}\left(h + \sqrt[3]{W_{est}}\right)\sin\theta \tag{3.13}$$

where M is the righting moment of the lateral float in lb-ft, R is a coefficient based on the weight of the aircraft, h is the negative metacentric height of the hull in feet and θ is the angle of heel required to completely submerge a lateral float. The buoyancy required is found by dividing the righting moment by the distance from the center of gravity of the lateral stabilizing float to the center of

the fuselage. This is the only major difference between the sizing of the wing-tip floats and sponsons. The sizing code then calculates the breadth of the stabilizing floats, b_{stabs},

$$b_{stabs} = \sqrt[3]{\frac{D_{stabs}}{2}} \tag{3.14}$$

where D_{stabs} is the displacement of one stabilizing float. The ratios for the length and depth to the breadth are given by Langley [36], with the length being 4 times the breadth and the depth being 0.5 times the breadth. Two stabilizing floats of these dimensions are then used to calculate drag and performance parameters.

3.1.3.4 Hydrofoil Calculations

A hydrofoil is an experimental method of water operation when applied to amphibious aircraft. A hydrofoil refers to a wing structure, usually mounted on a strut below the hull, which is used to lift the hull out of the water during forward motion. As the aircraft gains speed, the hydrofoil generates more lift, and begins to push the hull out of the water. This greatly reduces the amount of drag on the aircraft and allows for an increase in speed. The hydrofoil is usually configured in a Vee-shape, so as it comes out of the water, also known as unporting, it gradually looses lift until an equilibrium is achieved between the hydrofoil generated lift and the weight of the aircraft. In a single-hydrofoil configuration the hydrofoil is usually slightly in front of the center of gravity of the aircraft.

The design and weight analysis of the hydrofoil in the sizing code takes place after the weight buildup of the aircraft. It is assumed that the lift the hydrofoil is generating is equal to the weight of the aircraft minus the lift

generated by the wing. Next, the lift coefficient of the hydrofoil, as well as the aspect and taper ratios must be assumed. Knowing these variables allows for the calculation of the planform area and span of the hydrofoil. It is assumed that the hydrofoil will unport at the stall speed of the aircraft.

$$S_{HF} = \frac{L_{HF}}{\frac{1}{2}\rho_{water} V^2 C_{L,HF}} \tag{3.15}$$

$$b_{HF} = \sqrt{S_{HF} AR_{HF}} \tag{3.16}$$

3.1.4 Performance Estimation

3.1.4.1 Component Drag Estimation

With all the components (lifting surfaces, fuselage, water operation methods) of the aircraft now sized, the sizing code performs a drag buildup on the individual components during cruise and while in ground effect. The code calculates the parasitic (skin friction) drag of each component to approximate the drag for the entire aircraft.

The first step is to calculate the Reynolds number of each component using Equation 3.17,

$$Re = \frac{\rho V L}{\mu} \tag{3.17}$$

where ρ is the air density, V is the velocity, L is the characteristic length of the component and μ is the viscosity. The Reynolds number gives a measure of the ratio of inertial forces to viscous forces and expresses the relative importance between the two types of forces. Next, the flow over the component is assumed to be fully turbulent and the friction coefficient is estimated using a power law fit based on the component's Reynolds number with Equation 3.18 [3].

$$C_f = \frac{0.455}{(\log_{10} \mathrm{Re})^{2.58}(1+0.144M^2)^{0.65}} \tag{3.18}$$

Finally, with the friction coefficient found, a component parasitic drag coefficient can be estimated using the Equation 3.19 [3],

$$C_{D,0\ \mathrm{component}} = \frac{C_f S_{wet} FF}{S_{ref}} \tag{3.19}$$

where FF is a form factor used to account for pressure drag and higher-than-freestream velocities along the surface of the component, S_{wet} is the wetted area of the component, and S_{ref} is a reference area used to normalize the drag coefficients of the various components. The drag coefficients are then summed to find an estimated zero lift drag coefficient $C_{D,0}$.

3.1.4.2 Mission Performance Estimation

With estimates for component drag coefficients, the sizing code now calculates performance parameters, such as lift-to-drag ratios during various mission segments, maximum-range speed, required sea-level thrust and weight fractions. These weight factions are then used to determine the amount of fuel necessary for the aircraft to fly its mission profile.

First, a lift coefficient is found using Equation 3.20. This lift coefficient is then used to calculate the induced drag coefficient in Equation 3.21.

$$C_L = \frac{W_{est}}{qS_{ref}} \tag{3.20}$$

$$C_{D,i} = \frac{C_L^2}{\pi e AR} \tag{3.21}$$

In Equations 3.20 and 3.21, q is the dynamic pressure and e is Oswald efficiency factor, which is a ratio between the drag due to lift of a 3-D wing and a wing

having an equivalent aspect ratio and an elliptical lift distribution. The overall drag coefficient of the aircraft is then calculated using Equation 3.22.

$$C_D = C_{D,0} + C_{D,i} \tag{3.22}$$

C_D is calculated during cruise, flight in ground effect and alternate-airport-diversion mission legs and used to find the drag force generated by the aircraft, followed by the estimated weight being divided by the drag to find lift-to-drag ratios of the aircraft throughout its mission.

The sizing code is set up to accommodate both jet and propeller engines, with the maximum-range speed being calculated using Equations 3.23 and 3.24 respectively.

$$V_{max-range} = \sqrt{\frac{2*W_{est}*\sqrt{\frac{3}{C_{D,0}\pi eAR}}}{\rho S_{ref}}} \tag{3.23}$$

$$V_{max-range} = \sqrt{\frac{2*W_{est}*\sqrt{\frac{1}{C_{D,0}\pi eAR}}}{\rho S_{ref}}} \tag{3.24}$$

The maximum-range speeds are then used to find the thrust specific fuel consumption [3].

$$C_P = \frac{\dot{m}_f}{P} \tag{3.25}$$

$$C_T = \frac{\dot{m}_f}{T} \tag{3.26}$$

Equations 3.25 and 3.26 are the equations for power specific fuel consumption and thrust specific fuel consumption respectively. Power is found from Equation 3.27.

$$P = \frac{T\,V}{\eta_P} \tag{3.27}$$

Finally, Equations 3.25, 3.26 and 3.27 are combined and solved for C_t.

$$C_t = \frac{C_P V_{max-range}}{\eta_P} \tag{3.28}$$

The engine's required sea-level thrust is found using the total drag of the aircraft during the cruise segment of the flight profile multiplied by the ratio of density at sea-level to the density at cruise altitude. The weight fraction (WF) during the various mission legs (cruise, in ground effect, during IFR reserves), is then found using the max-range speed, thrust coefficient, lift-to-drag ratio, and the range (R) of the mission leg in Equation 3.29.

$$WF = e^{\frac{R*C_t}{\frac{L}{D}*V_{max-range}}} \tag{3.29}$$

The weight fractions for all the mission legs are then used to calculate the fuel weight fraction (FWF) which corresponds to the amount of fuel the aircraft will require to complete its mission using Equation 3.30.

$$FWF = 1.06(1 - WF_{Cruise}\, WF_{GE}\, WF_{IFR}\, WF_{TO}\, WF_{Climb}\, WF_{Decent}\, WF_{Landing}) \tag{3.30}$$

The weight fraction during take-off, climb, descent and landing are given by Raymer [3] and are hardcoded into the sizing program. The fuel weight fraction can then be multiplied by the estimated weight to find the weight of fuel needed by the aircraft to complete its mission.

The aerodynamic center of the main wing and tails as well as the Oswald efficiency factor is calculated using a vortex lattice subroutine inside of the sizing code. The vortex lattice routine is fed the geometry of the wings and tails and models these surfaces as an infinitely thin sheet of discrete horseshoe vortices, which are then used to calculate the lift and induced drag of the lifting surface. These results are used to determine the location of the aerodynamic centers of

the main wing and horizontal tail, which are then output back into the sizing code and used in subsequent calculations.

3.1.5 Weight Buildup

Next, the sizing code performs a detailed weight build up of the amphibious aircraft. Much of the procedure for the weight build up is taken from Raymer [3], who uses a predominately empirical method for determining the weights of the individual aircraft components based on the weight breakdowns of existing aircraft. The code is set up to perform the weight build up of both general aviation and cargo aircraft. These two aircraft configurations use different sets of empirical equations because of the great differences in both their size and utility.

The sizing code also calculates the additional weight due to the aircraft's chosen method of water operation. The weight of the floats is calculated using two methods and the average of these weights is used for the empty weight analysis. The first method plots the weight of various production floats against their displacement. A linear trendline is then applied to the data and is used to find the weight of the float being designed based on its necessary displacement.

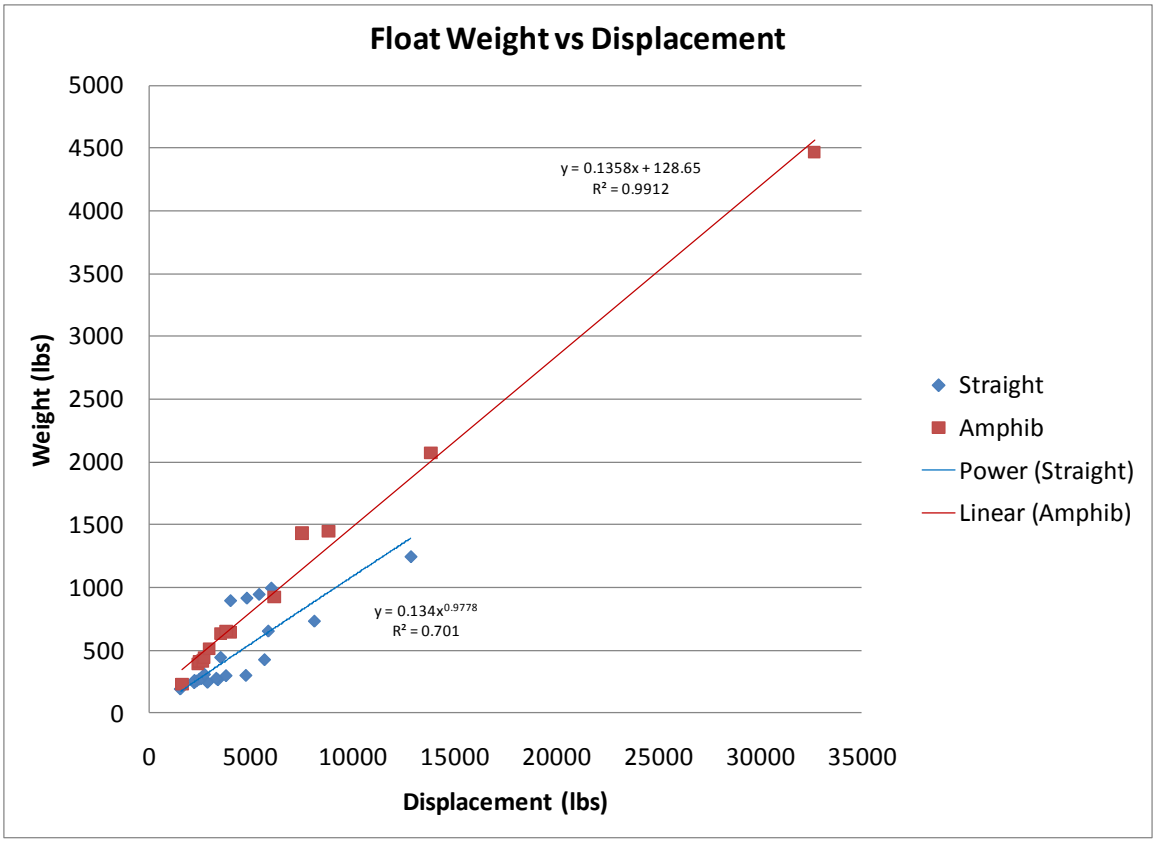

Figure 13: Float Weight vs. Displacement

The second method of finding the float weight, taken from Langley [36], uses the empirical relationship shown in Equation 3.31.

$$W_{floats} = 0.073W_{est} + 87 \tag{3.31}$$

Both of these empirical relationships have units of lbs. The weight of the struts used to connect the floats to the fuselage/wings of the aircraft is also given through the use of an empirical formula taken from Langley [36], with the struts weighing approximately 3% of the total weight of the aircraft.

The weight of the wing-tip floats, which are used to augment the transverse stability of the amphibious aircraft, is calculated through the use of an empirical relationship, with the weight of the wing-tip floats being 1.2% of the total weight of the aircraft. The weight of the stabilizing sponsons is calculated by assuming the sponson has a wall thickness of ¼ in. and is made of fiberglass with a density

of 96.768 lb/ft^3. The weight of the hydrofoil and attaching strut is calculated by multiplying the volume of the hydrofoil, which is determined during its sizing, by the density of aluminum.

Finally, the weight of the fuel is calculated by multiplying the fuel weight fraction by the estimated gross takeoff weight of the aircraft. The weights of the individual aircraft components, the chosen method of water operation, fuel and payload are then sent to the center of gravity (CG) and neutral point calculation functions.

3.1.6 Center of Gravity and Neutral Point Calculation

The CG function assumes that the weight of the water operation device is located at the center of gravity. The location of the center of gravity is found by adding the moment caused by the weight of each component, with the reference location at the nose of the fuselage, together and dividing by the total weight of the aircraft minus the weights of components located at the CG. This results in the CG location as a distance back from the nose of the fuselage.

The weight of all the lifting surfaces is assumed to be concentrated at the quarterchord of those surfaces. Placement of those surfaces is dependent on the aircraft configuration (flying wing, canard, or conventional). For example, the leading edge of the horizontal tail in the canard configuration is located at the nose of the fuselage, while the trailing edge of the horizontal tail in the conventional configuration is located at the aft end of the fuselage. There is no horizontal tail in the flying wing configuration. The vertical tail placement in the conventional configuration is dependent on the L_{VT} parameter, which is the distance from the vertical tail quarterchord to the quarterchord of the main wing.

In the flying wing and canard configurations, due to the shorter moment arm available because of the placement of the main wing, the vertical tail is moved out to the separation point between the inboard and outboard wing segments. This allows for a reduction in the vertical tail planform area necessary to give sufficient control of the aircraft. Fuel placement is based on whether the code is sizing an aircraft with fuel at the CG or in the wings. If the fuel is in the wings, it is placed in the inboard wing section between the 35% and 60% chord-line. The other components, such as engines, landing gear, hydraulics, anti-ice gear, etc. are placed based on the location of the main wing and fuselage and rely largely on the designer to place them in a realistic position.

With the center of gravity position located, the sizing code then moves on to neutral point calculation. First, the locations of the aerodynamic centers of the main wing and horizontal tails are located with their reference point at the nose of the fuselage to put it in the same reference frame as the CG location.

To simplify the equations for calculating the neutral point, the positions of the center of gravity and aerodynamic centers of the main wing and horizontal tail are all expressed as fractions of the mean chord of the main wing.

The position of the aircraft's neutral point is calculated using Equation 3.32,

$$\bar{X}_{np} = \frac{C_{L_\alpha}\bar{X}_{acw} - C_{m_{\alpha fuse}} + \eta_h \frac{S_h}{S_w} C_{L_{\alpha h}} \frac{\delta\alpha_h}{\delta\alpha} \bar{X}_{ach}}{C_{L_\alpha} + \eta_h \frac{S_h}{S_w} C_{L_{\alpha h}} \frac{\delta\alpha_h}{\delta\alpha}} \tag{3.32}$$

where C_{L_α} and $C_{L_{\alpha h}}$ are the lift curve slope for the main wing and horizontal tail and are calculated by the vortex lattice code. $\bar{X}_{acw}$ and $\bar{X}_{ach}$ are the locations of the aerodynamic centers of the wing and horizontal tail respectively. η_h is a coefficient representing the ratio between the dynamic pressure at the tail and the freestream dynamic pressure. For a canard, this coefficient is 1.0, while for a

conventional aircraft it ranges from about 0.85 to 0.95 and is taken to be 0.9 for these calculations. $C_{m_{\alpha fuse}}$ is the pitching moment contribution from the fuselage and was calculated using Equation 3.33.

$$C_{m_{\alpha fuse}} = \frac{K_f W_f^2 L_f}{\bar{c} S_w} \tag{3.33}$$

W_f is the maximum width of the fuselage and L_f is the length. K_f is an empirical pitching moment factor found from Figure 14.

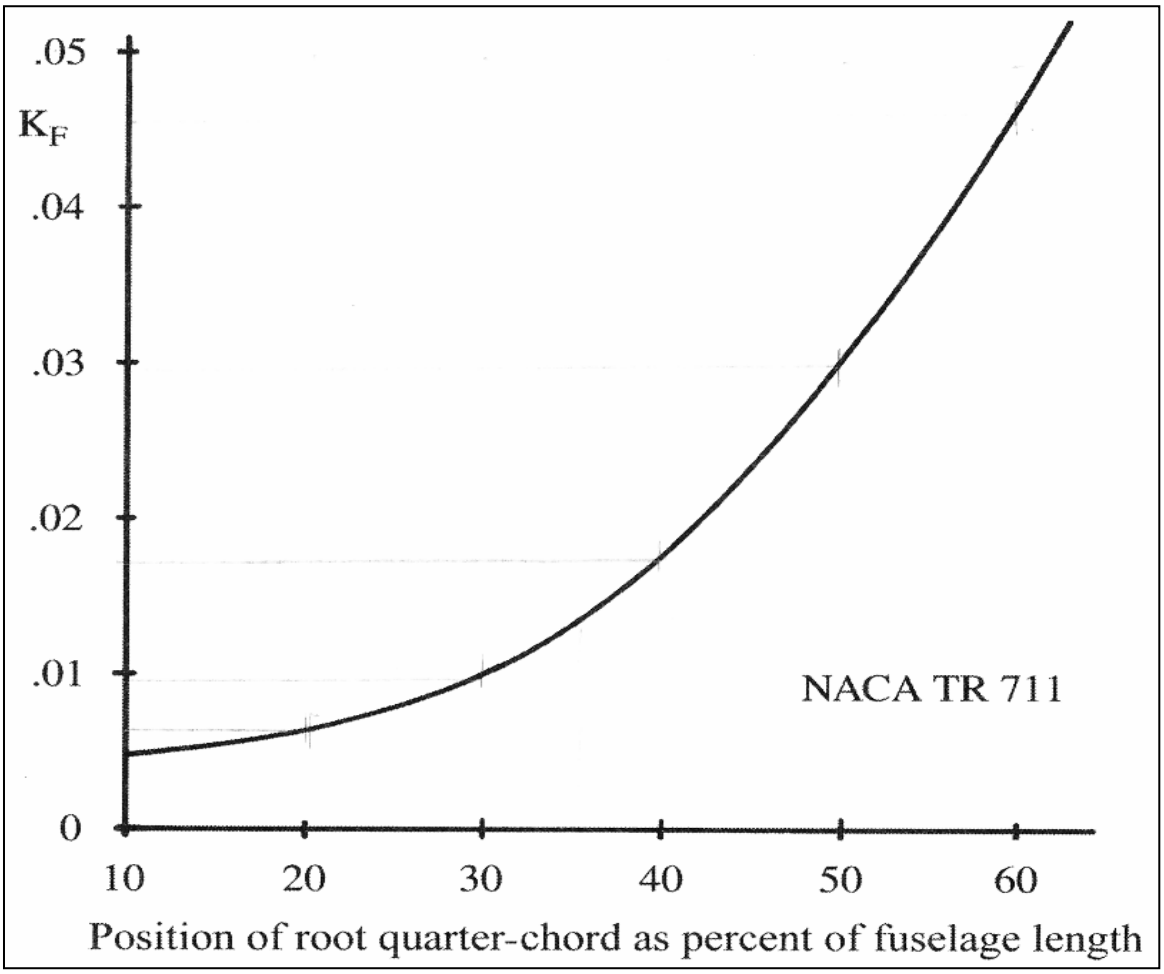

Figure 14: Fuselage Moment Term [38]

Finally, the $\frac{\partial \alpha_h}{\partial \alpha}$ term is a downwash derivative that describes the flow interaction between the main wing and horizontal stabilizers and changes the local angle of attack. For a canard configuration, there is no downwash from the

wing on the horizontal stabilizer, but the downwash from the canard will affect the wing. The estimation of the canard effect on the wing is difficult because the downwash varies across the canard span and, outboard of the canard, the wing tip vortices actually create an upwash on the wing. In a canard configuration, the effect of upwash from the wing onto the canard is calculated using Equation 3.34,

$$\frac{\partial \alpha_h}{\partial \alpha} = 1 + \frac{\partial \epsilon_u}{\partial \alpha} \tag{3.34}$$

where $\frac{\partial \epsilon_u}{\partial \alpha}$ is interpolated from Figure 15.

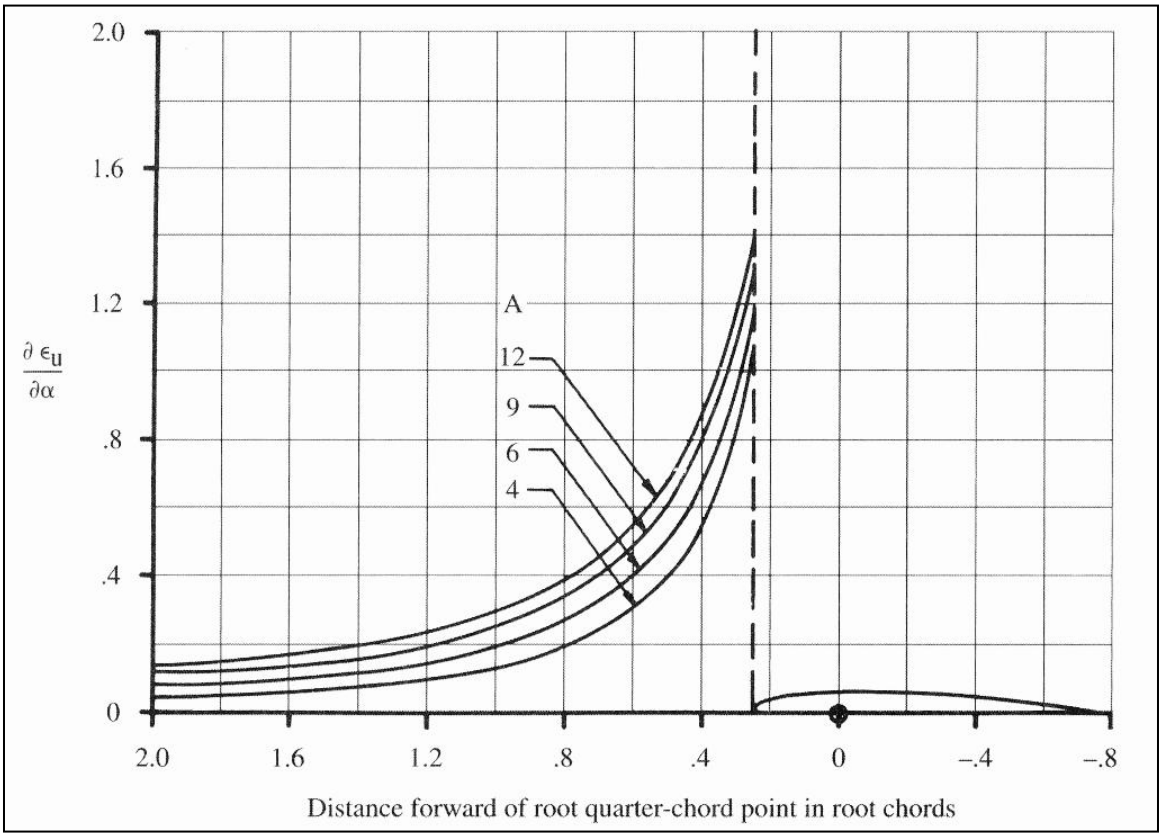

Figure 15: Upwash Estimation [3]

For a conventional tail configuration, the downwash derivative is found using Equation 3.35,

$$\frac{\partial \alpha_h}{\partial \alpha} = 1 - \frac{\partial \epsilon}{\partial \alpha} \tag{3.35}$$

where $\frac{\partial \epsilon}{\partial \alpha}$ is found using an Equation 3.36 from Pamadi [39].

$$\frac{\partial \epsilon}{\partial \alpha} \approx \frac{2C_{L_\alpha}}{\pi AR} \tag{3.36}$$

For an aircraft with a flying wing configuration, there is no downwash derivative and the equation for the neutral point simplifies down to Equation 3.37.

$$\overline{X}_{np} = \frac{C_{L_\alpha}\overline{X}_{acw} - C_{m_{\alpha fuse}}}{C_{L_\alpha}} \tag{3.37}$$

It can be seen from this equation that there is no stabilizing term for a tailless aircraft (flying wing), which means that the aerodynamic center of the main wing must be behind the center of gravity of the aircraft to make the aircraft statically stable.

With the position of the neutral point and center of gravity now known, the longitudinal static margin of the aircraft can be calculated using Equation 3.38.

$$SM = \overline{X}_{np} - \overline{X}_{cg} \tag{3.38}$$

If the CG of the aircraft is ahead of the neutral point, the static margin is positive, so the aircraft is statically stable. At the CG's aft most position, the static margin of a typical transport aircraft is usually between 5-10%.

3.1.7 Sample Output

When the previously described calculations are complete, the sizing code has determined the size and geometry of the aircraft wing surfaces, fuselage, and water operation device. It has also performed a drag build up on a component-by-component basis and used it to determine the performance characteristics of the aircraft. Additionally, it has created an empty weight build up of the aircraft based on each individual component and used those weights to determine the

location of the center of gravity. Finally, the sizing code has found neutral points of the lifting surfaces and calculated the static margin of the aircraft. To properly convey this information to the designer, the code has been designed to output both a drawing of the aircraft (Figure 16), which shows the placement of major components, as well as a text file, which has a more detailed breakdown of the aircraft, showing the geometric parameters, placement and weights of components and performance parameters. An example of the output text file can be found in Appendix A.

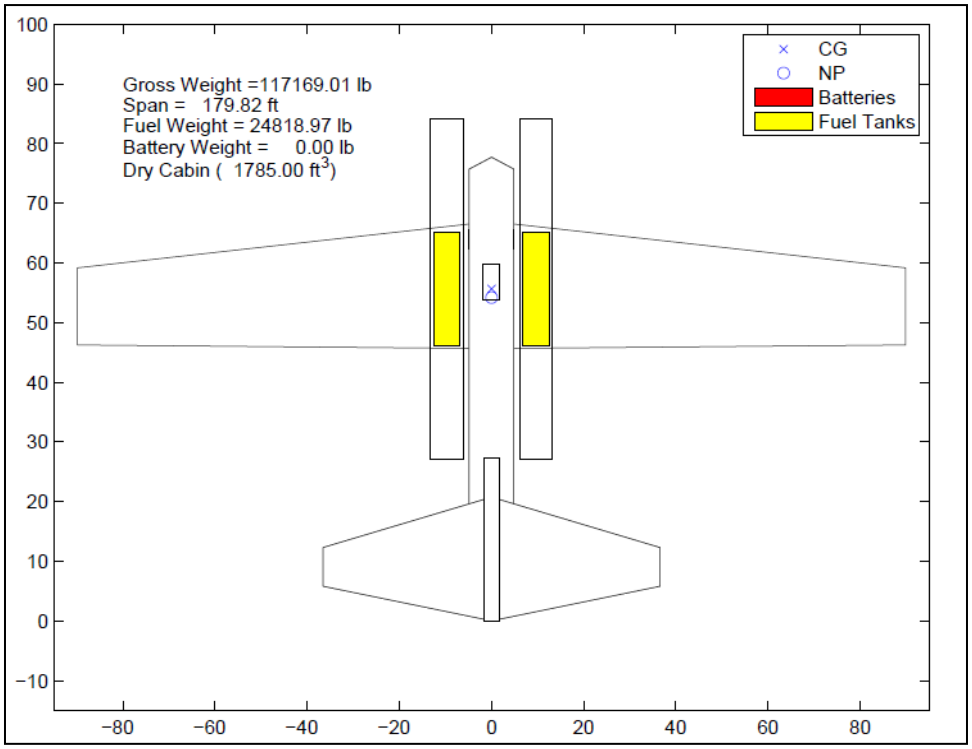

Figure 16: Sizing Code Sample Output

3.2 Validation

The sizing code was validated by using a Lockheed C-130-H and a Cessna 172-R to ensure that the sizing algorithms used in the code were working

properly over a large range of aircraft gross weights as well as aircraft types. Geometries of the two aircraft were run through the code to determine how well the coded algorithms predicted the takeoff weight and performance parameters.

3.2.1 Lockheed C-130-H

The Lockheed C-130-H is a turboprop, four-engine, military transport aircraft in use by the United States military and many other countries around the world. It was primarily designed for troop and cargo transport but has seen duty in a number of other roles, including as a gunship (AC-130), aerial refueling, search and rescue, and aerial firefighting.

Figure 17: Lockheed C-130-H [40]

The C-130-H was used in this validation effort as an example of a large, cargo aircraft. Figure 18, below, shows the Lockheed C-130-H geometry from the

sizing program and Table 1 presents a comparison of the weight calculations and geometric parameters from the program and from the actual aircraft. The weight calculations are within 7.5% and the largest geometrical deviation is the horizontal tail root chord length, which reflects a difference in the assumed taper ratio.

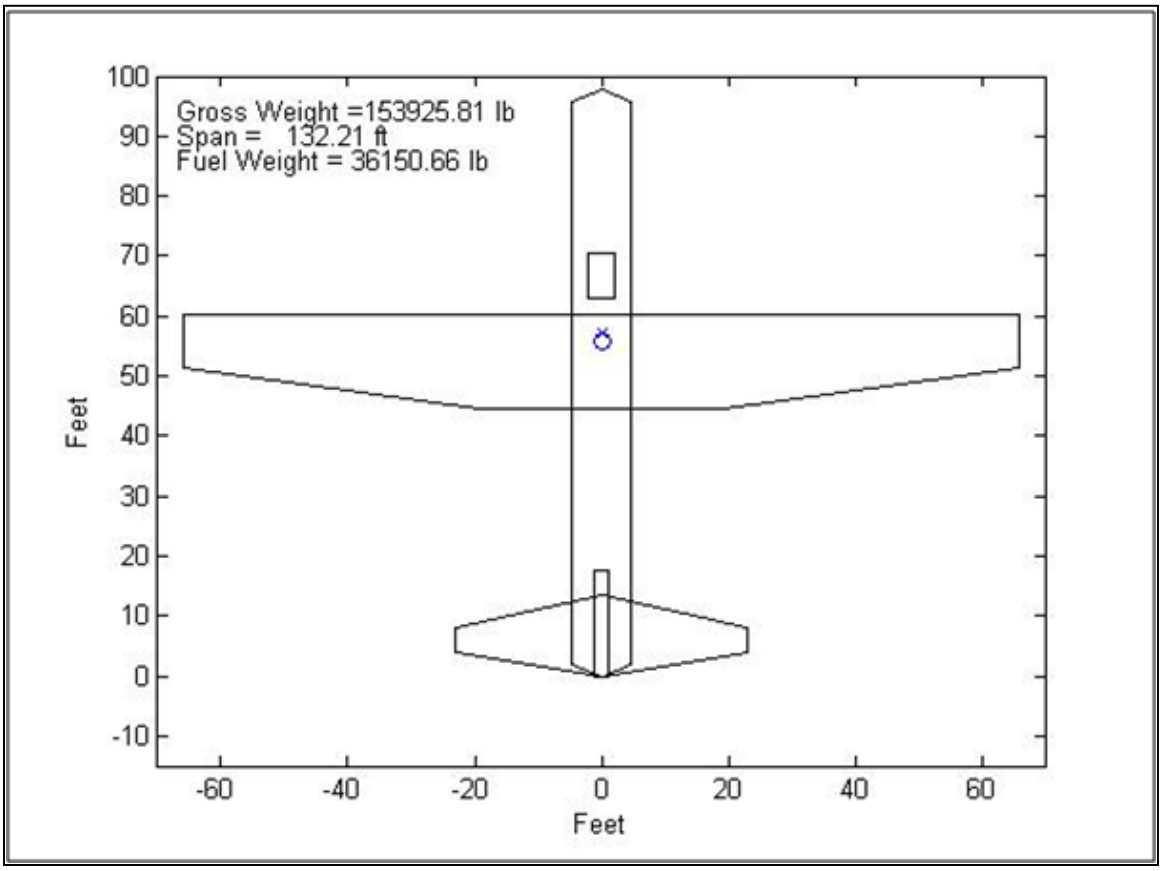

Figure 18: Lockheed C-130-H Sizing Code Output

Table 1: Lockheed C-130-H Validation Results [40]

	Sizing Code	Actual	% Error
Gross Take-off Weight (lb)	155,401.3	155,000.0	0.3%
Empty Weight (lb)	73,629.1	75,745.0	2.8%
Fuel Weight (lb)	36,772.1	34,255.0	7.3%
Planform Area (ft^2)	1,752.3	1,745.0	0.4%
Span (ft)	132.8	132.6	0.2%
Root Chord (ft)	15.6	15.1	3.5%
Wingloading (lb/ft^2)	88.7	88.8	0.2%
Planform Area, Horizontal Tail (ft^2)	491.3	536.0	8.3%
Span, Horizontal Tail (ft)	50.4	52.7	4.3%
Root Chord, Horizontal Tail (ft)	14.9	17.2	13.7%
Planform Area, Vertical Tail (ft^2)	307.0	300.0	2.3%
Span, Vertical Tail (ft)	24.9	24.6	1.1%
Root Chord, Vertical Tail (ft)	19.2	21.5	10.7%
Cruise Speed (knots)	267.6	292.0	8.3%

3.2.2 Cessna 172-R

The Cessna 172-R Skyhawk is a four-seat, single piston-propeller engine, general aviation aircraft. More Cessna 172 variants have been built than any other aircraft in history. The 172-R variant was introduced in 1996 and is the first Skyhawk to have a fuel-injected engine from the factory.

Figure 19: Cessna 172-R [41]

The Cessna 172-R was included in this validation effort as an example of a small, light-weight, general aviation aircraft.

Figure 20 shows the geometry for the 172-R and Table 2 shows a comparison of the various weight and geometric parameters. The weight estimates are captured quite reasonably, with the greatest error being a 5.6% difference in estimated fuel weight. As with the C-130-H, the largest geometric error was in the root chord length estimates for the horizontal and vertical stabilizers.

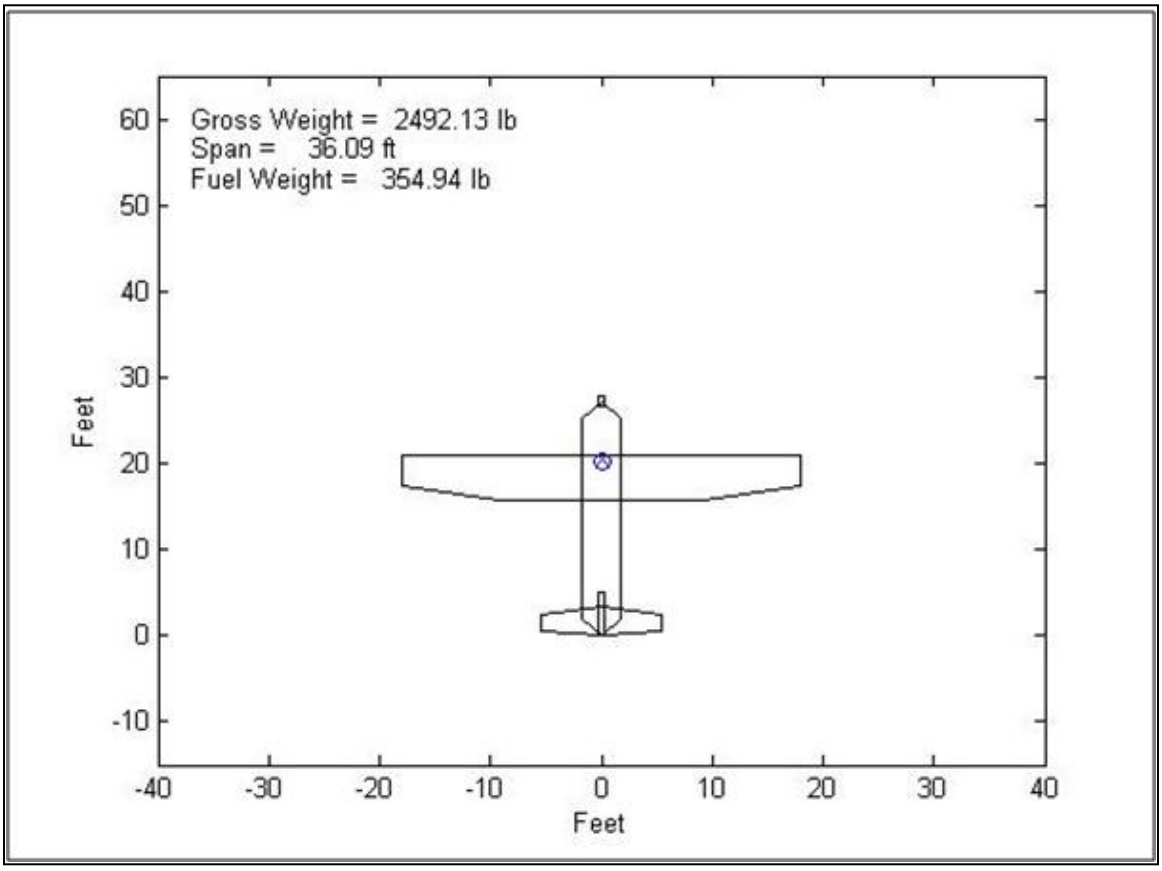

Figure 20: Cessna 172-R Sizing Code Output

Table 2: Cessna 172-R Validation Results [41]

	Sizing Code	Actual	% Error
Gross Take-off Weight (lb)	2,492.1	2,550.0	2.3%
Empty Weight (lb)	1,562.2	1,639.0	4.7%
Fuel Weight (lb)	354.9	336.0	5.6%
Planform Area (ft^2)	174.1	174.0	0.1%
Span (ft)	36.1	36.1	0.0%
Root Chord (ft)	5.3	5.3	0.0%
Wingloading (lb/ft^2)	14.3	14.7	2.3%
Planform Area, Horizontal Tail (ft^2)	29.4	30.0	2.1%
Span, Horizontal Tail (ft)	10.8	11.3	4.8%
Root Chord, Horizontal Tail (ft)	3.5	4.0	13.5%
Planform Area, Vertical Tail (ft^2)	14.9	14.9	0.3%
Span, Vertical Tail (ft)	4.1	4.0	2.0%
Root Chord, Vertical Tail (ft)	5.1	5.3	2.3%
Cruise Speed (knots)	82.9	94.0	11.8%

To assess the accuracy of the drag impact due to the inclusion of water operations in the sizing code, the Cessna 172-R geometry was run again, this time with the addition of twin floats, a modification regularly seen to Cessna 172's. Figure 21 shows the resulting geometry. Adding a set of Baumann floats to a Cessna 172-R increases the gross weight of the aircraft by approximately 275 lb [42], which yields a gross weight of 2825 lb. The gross weight of the 172-R with floats predicted by the sizing code was 2779.49 lb. This results in a 1.61% error.

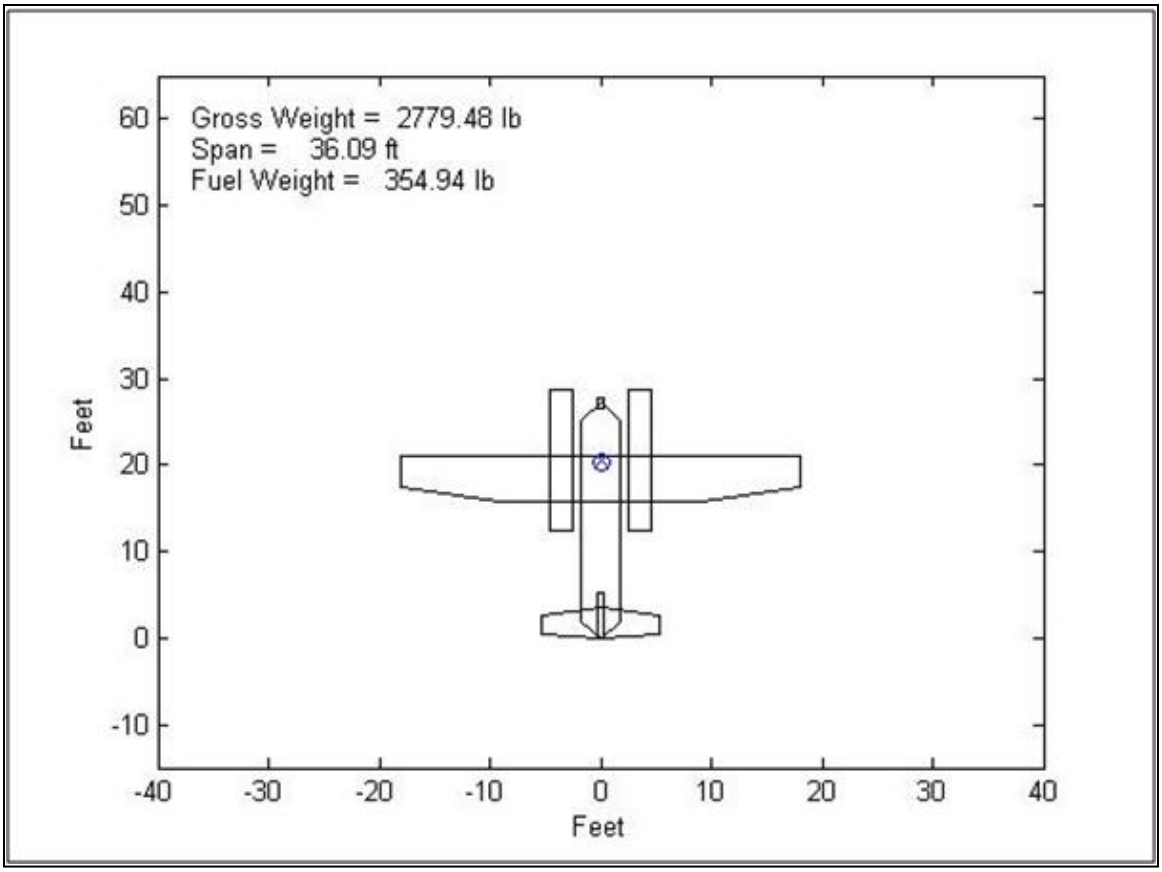

Figure 21: Cessna 172-R with Floats Sizing Code Output

3.2.2.1 Wind Tunnel Model and Results

A wind tunnel model was built to assess the floats' impact on the performance of the 172-R as well as to validate the performance data the sizing code had output for the modified 172-R. The floats were modeled off of the Baumann BF2550 Floats [42], which are regularly used for Cessna 172 conversions. The model was tested in Auburn University's 3 ft. X 4 ft. subsonic wind tunnel. Full results from these wind tunnel tests can be found in Appendix C.

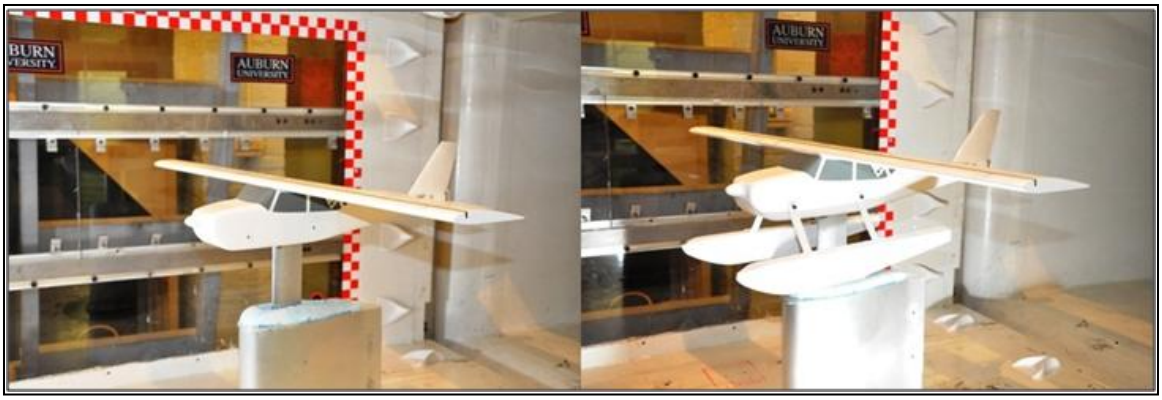

Figure 22: Cessna 172 Wind Tunnel Model

Table 3: Float Sizing Comparison

	Sizing Code	BF22250	% Error
Breadth (ft)	2.06	2.17	5.3%
Length (ft)	16.44	16.92	2.8%
Depth (ft)	2.31	2.17	6.7%
Displacement (ft^3)	39.09	39.58	1.3%

Table 4: Drag Comparison for Cessna 172-R

	C_{D0}		Drag Area (ft^2)	
	No Floats	**Floats**	**No Floats**	**Floats**
Actual Aircraft	0.03207	-	5.58	-
Sizing Code	0.03265	0.04594	5.68	8.00
Wind Tunnel	0.0480	0.0641	8.35	11.15
Adjusted Wind Tunnel	0.0340	0.0506	5.91	8.79
% Error (Sizing Code vs Adjusted Wind Tunnel)	4.1%	10.1%	4.0%	9.9%

From Table 3, it can be seen that the sizing code very accurately predicted the necessary size of the floats, with less than 7% error in any dimension. Also, Table 4 shows that the sizing code accurately predicts the zero-lift drag coefficient as well as the equivalent parasitic drag area for the case with no floats when compared to the actual drag values from a 172-R. Also, results from the

wind tunnel tests of the 172-R model (once corrected to the full-scale Reynolds number) with and without floats were very encouraging. The tunnel tests were consistently predicting conservative drag numbers, which is logical, as there are blockage effects and wall interactions as well as surface imperfections and manufacturing defects, which will all increase the measured drag of the model.

The Reynolds number correction methodology used in this research was described by Barlow, Rae and Pope [29], and detailed in Section 2.4 of this report.

Chapter 4

Design Optimization

4.1 Optimizer Selection

As has been discussed previously, there are many different optimization methods and algorithms that could be applied to the problem of amphibious aircraft preliminary design. Each optimizer has its pros and cons, with some meeting the requirements of this research better than others. Aircraft design optimization requires the variation of a large number of variables, which means that the chosen optimization algorithm will have to operate in a large design space. To be effective and useful, the optimizer must converge fairly quickly yet still process a large enough sample of possible candidates to reasonably ensure that the final design is a global optimum.

As the sizing code was written in MATLAB, the first optimizer selected for use was fminsearch, which is built into MATLAB. Fminsearch is a nonlinear numerical optimization method that uses a Nelder-Mead simplex algorithm, as described in Lagarias [43], to minimize a function. Initially, for an n-dimensional vector x and initial guess x0, the algorithm adds 5% of each component variable, x0(i), to x0, and uses these n vectors in addition to x0 to create a n+1 simplex around x0. Then, the algorithm modifies the simplex repeatedly according to the following procedure.

1. Let x(i) be all the points in the current simplex, where i=1, 2,…, n, n+1.
2. The points in the simplex are then ordered from the lowest function value, f(x(1)), to the highest function value, f(x(n+1)). For each iteration step, the algorithm throws away the worst point, x(n+1), and accepts another point into the simplex.

3. A reflected point, r, is generated using the following equation,

$$r = 2m - x(n+1) \tag{4.1}$$

where

$$m = \sum_{i=1}^{n} \frac{x(i)}{n} \tag{4.2}$$

and f(r) is then calculated.

4. If $f(x(1)) \leq f(r) < f(x(n))$, r is accepted into the simplex and this iteration of the minimization algorithm is terminated.
5. If $f(r) < f(x(1))$, calculate the expansion point, s,

$$s = m + 2(m - x(n+1)) \tag{4.3}$$

and calculate f(s).

   a. If $f(s) < f(r)$, accept s into the simplex and terminate the iteration.
   b. If not, accept r into the simplex and terminate the iteration.

6. If $f(r) \geq f(x(n))$, a contraction is performed between m and the lower value of x(n+1) and r.

   a. If $f(r) < f(x(n+1))$, calculate c using

$$c = m + \frac{(r-m)}{2} \tag{4.4}$$

   and then find f(c). If $f(c) < f(r)$, accept c into the simplex and terminate the iteration.

   b. If $f(r) \geq f(x(n+1))$, calculate cc using

$$cc = m + \frac{(x(n+1)-m)}{2} \tag{4.5}$$

and then find f(cc). If f(cc) < f(x(n+1)), accept cc into the simplex and terminate the iteration.

7. Finally, calculate the n points

$$v(i) = x(1) + \frac{(x(i)-x(1))}{2} \tag{4.6}$$

and calculate f(v(i)), for i=2, 3,…, n, n+1. The simplex at the next iteration will be x(1), v(2),…, v(n), v(n+1).

Fminsearch will continue using this Nelder-Mead simplex algorithm to return local minimizers of the target function until a stopping criterion is met. MATLAB allows for a number of different stopping criteria: maximum number of function evaluations reached, maximum number of iterations reached, tolerance on the function value reached, and tolerance on x value reached. One of the drawbacks of using fminsearch is that the optimizer generally tends to become stuck on local optima, as it is very reliant on the initial guess, x0.

To counter this reliance on having a very accurate initial guess and to increase the chances of find a globally optimized solution, a particle swarm technique was integrated with the fminsearch simplex optimizer. This hybrid optimization algorithm uses the particle swarm as the global optimizer and transport mechanism. Fminsearch is used as the local simplex optimizer. If the allowed design space is compared to an area full of hills, with the top of each hill being a locally optimized solution, then it could be said that the particle swarm moves the particles, which represent possible answers, from one hill to another while the simplex optimizer finds the top of the hill it is on. In this way, the hybrid optimizer is much more likely to find a globally optimized solution to a given problem.

Initially, when using the hybrid particle swarm/simplex algorithm, a random population sample must be generated. All variables that are to be optimized (in the case of this research there are 10) will be randomized for each particle to give the particle a position on the available design space [44].

$$x(j,i) = R\big(xmax(j) - xmin(j)\big) + xmin(j) \tag{4.7}$$

where i=1,…,population size, j=1,…,number of variables, and R is a randomly chosen number.

With an initial random sample of particles in place, the simplex optimizer runs to find the local optimum position of each particle. With that completed the particle swarm then gives each particle a new velocity and position [2].

$$v_{i+1} = \alpha R_1(\hat{x}_i - x) + \omega\beta R_2(\hat{x}_{ni} - x) + \omega\gamma R_3 + \omega v_i \tag{4.8}$$

$$x_{i+1} = x_i + v_{i+1} \tag{4.9}$$

where α, β, and γ are constants; ω is an inertial constant which gives relative weights to the local and global particle bests; R_1, R_2, and R_3 are random numbers; x_i is the current particle position; and $\hat{x}_i$ and $\hat{x}_{ni}$ are the best position the individual particle and whole swarm have seen, respectively. The algorithm then runs the local simplex optimizer again, and this process repeats itself through a given number of generations. The individual particles have basic knowledge of both their own best position and the best position that the swarm has seen. Over multiple generations, this knowledge is used to adjust their velocity and position to keep the particles moving toward the globally optimized solution. The effect of the particle's best position on its velocity is the first term in the velocity equation. The effect of the swarm's best position on velocity is the second term of the velocity equation. The last two terms in the velocity equation are repulsive terms. They are designed to keep the particles away from each

other to prevent the overall solution from becoming trapped on local optima. These repulsive forces make the hybrid optimization algorithm more effective at finding globally optimized solutions, but at the expense of computation time.

4.2 Optimization Methodology

With the optimizer determined, the next step was to integrate it into the existing sizing code. To do this, first a new execution file was made and the current sizing program was changed into a function. This allowed the sizing code to be looped through the optimization program, which is necessary as the optimization program was used to call the particle swarm optimizer, which globally optimized the particles, as well as fminsearch, the simplex optimizer which found local minima around each particle.

It was decided that the amphibious aircraft would be optimized for minimum weight, because, in general, the lower the weight of the aircraft, the less expensive the aircraft is to design and manufacture. With an objective function chosen, 10 optimization variables were selected: aspect ratio, inboard and outboard taper ratios, inboard and outboard sweep angles, tail moment arm length, fineness ratio, canard fraction, engine position, and cabin position. By choosing to use these parameters, the optimizer was given as much freedom as possible to completely change the geometry of the aircraft. Minimum and maximum bounds were set on the variables to keep the geometry from becoming unrealistic. The hybrid optimizer was set to run for 10 generations.

To increase the usefulness of the optimizer even further, another program was set up to loop the optimization program through multiple configurations of aircraft. The program controlled both the aircraft tail configuration (flying wing,

canard, or conventional), as well as the method of water operation. It allowed a loop to be constructed that would optimize the design for every allowable aircraft configuration without requiring user input.

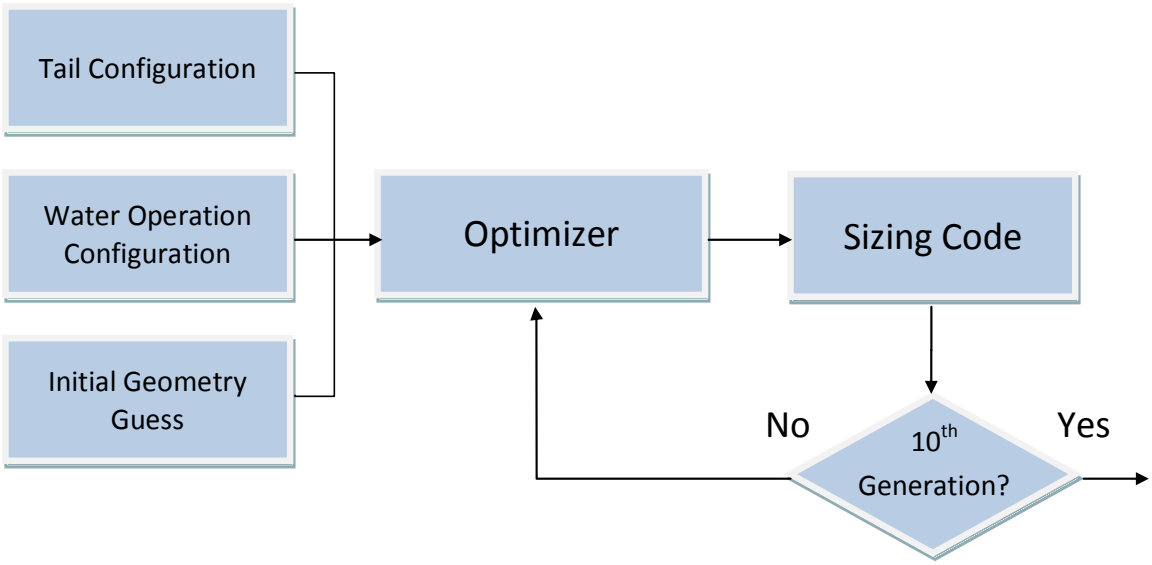

Figure 23: Optimization Program Flowchart

4.2.1 Penalty Functions

Three penalty functions were used to make it less likely that the optimizer would change the geometric variables in such a way that the resulting airplane would be in an infeasible configuration. The penalty functions cause an increase to the objective function, in this case the aircraft gross weight, if they are violated. They increase the weight in an exponential fashion; the further away from the limits set by the penalty functions, the greater the penalty. Ideally, this forces the optimizer to stay in the bounds set down by the penalty functions.

The first penalty function set bounds on the static margin of the aircraft. The static margin, as stated previously, is the difference between the location of the neutral point and center of gravity of the aircraft, expressed as a percentage

of fuselage length. If the center of gravity of the aircraft is more forward than the neutral point, the aircraft is longitudinally statically stable in flight. To ensure that the aircraft will be sufficiently stable, the lower bound set by the penalty function was a static margin of 8%. Excessive stability also is not a wanted, as too much stability will result in an aircraft that is difficult to trim and maneuver. The upper bound set by the penalty function was a static margin of 15%. The functions chosen were:

$$PF_{SM} = c(8 - 100SM)^a \tag{4.10}$$

$$PF_{SM} = c(100SM - 15)^a \tag{4.11}$$

$$W_{est,pf} = W_{est} + PF_{SM} \tag{4.12}$$

where c = 10^6 and a = 4. The values of c and a are constant though all three penalty functions. If the static margin lies between 8% and 15%, the value of penalty function is 0.

The second penalty function influences the spacing between the horizontal tail and main wing of the aircraft, dependent on configuration. For a conventional configuration, the penalty function requires that there must be at least one root chord length of the main wing between the horizontal tail leading edge and main wing trailing edge.

$$dx1 = X_{LE,tail} - (X_{TE,wing} + C_{root,wing}) \tag{4.13}$$

For a conventional aircraft, the penalty function also states that the main wing must be at or behind the nose of the aircraft.

$$dx2 = X_{LE,wing} \tag{4.14}$$

For a canard, the penalty function says that there must be at least 1.5 canard root chords between the trailing edge of the canard and the leading edge of the main wing.

$$dx1 = X_{LE,wing} - (X_{TE,canard} + 1.5C_{root,canard}) \tag{4.15}$$

The penalty function also states that the canard must be at or aft of the nose of the aircraft.

$$dx2 = X_{LE,canard} \tag{4.16}$$

If the required conditions are not met, the penalty function then chooses the smaller of dx1 and dx2 to perform the penalty on.

$$dx = \min(dx1, dx2) \tag{4.17}$$

$$PF_{wing} = cdx^{a} \tag{4.18}$$

$$W_{est,pf} = W_{est} + PF_{wing} \tag{4.19}$$

Finally, the third penalty function aims to ensure that a straight spar can be installed over the full span of the wing, between the 20% and 30% chord locations at the wing root and wing tip.

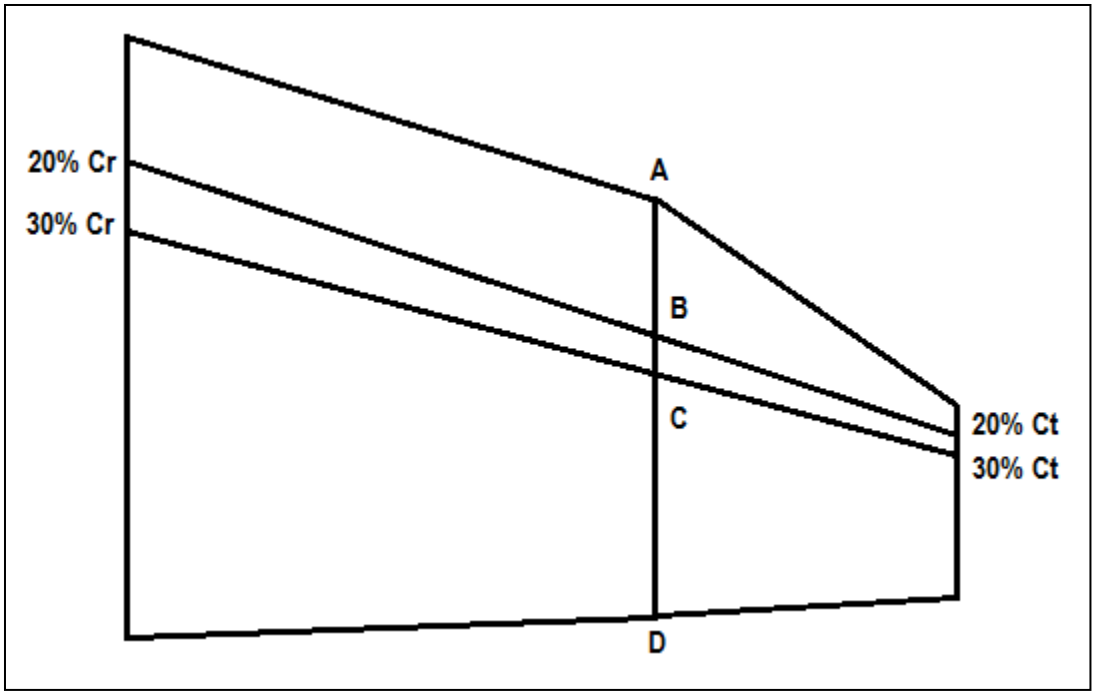

Figure 24: Wing Structure Penalty Function

To accomplish this, the penalty function locates the position of Points A, B, C, and D. These points lie on the intersection between straight lines connecting the 20 and 30% chord locations on the root and tip of the wing and the split between the inboard and outboard section of the wing. In order for the spar to be straight, Point A must always lie forward of Point B, and Point D must always lie aft of Point C.

$$\mathrm{dx1} = \mathrm{PointA} - \mathrm{PointB} \tag{4.20}$$

$$\mathrm{dx2} = \mathrm{PointC} - \mathrm{PointD} \tag{4.21}$$

If either dx1 or dx2 is less than 0, then the structural requirement of keeping a straight spar for the wing is not being met, and the penalty function will choose the greater of the absolute value of dx1 and dx2 to perform its penalty on.

$$\mathrm{dx} = \max\left(|\mathrm{dx1}|, |\mathrm{dx2}|\right) \tag{4.22}$$

$$\mathrm{PF}_{\mathrm{structure}} = \mathrm{cdx}^{\mathrm{a}} \tag{4.23}$$

$$W_{est,pf} = W_{est} + PF_{structure} \tag{4.24}$$

If dx1 and dx2 are greater than 0, then a straight spar can be maintained from wing root to wing tip, and no penalty is applied to the objective function.

4.3 Results

With the optimizer now integrated with the sizing code and penalty functions in place to steer the aircraft toward a realistic geometry, a mission profile was input as well as basic geometrical characteristics. The mission profile was chosen to be that of a littoral troop transport aircraft. This aircraft would replace the current method of deploying to beaches, which is generally performed with by transport ship or hovercraft, both of which are quite slow and lacking in range without the support of a larger ship. This littoral transport aircraft is designed to deploy from a distant base, land near the shore of its target location, offload its cargo, and return to its base of origin. It will have a mission cruise radius of 1,000 nmi. at 20,000 ft., descend to near sea level for a 15 nmi. approach leg, land and extract in the reverse order. The mission duration totals 2,000 nmi. at 20,000 ft. and 30 nmi. in ground effect. The aircraft will also have 45 minutes of IFR reserve fuel. The aircraft has a payload capacity of 18,750 lb., which is the equivalent of 50 soldiers and their gear.

The optimizer was run for 30 different aircraft configurations. Three different tail configurations (conventional, flying wing, and canard), with two different fuel placement locations (fuel at the center of gravity and fuel in the wings), were run for five different water operation configurations: twin floats, boat hull with hydrofoil and sponsons, boat hull with hydrofoil and tip-floats,

boat hull with sponsons, and boat hull with tip-floats. The results of this optimization run are shown in Figure 25.

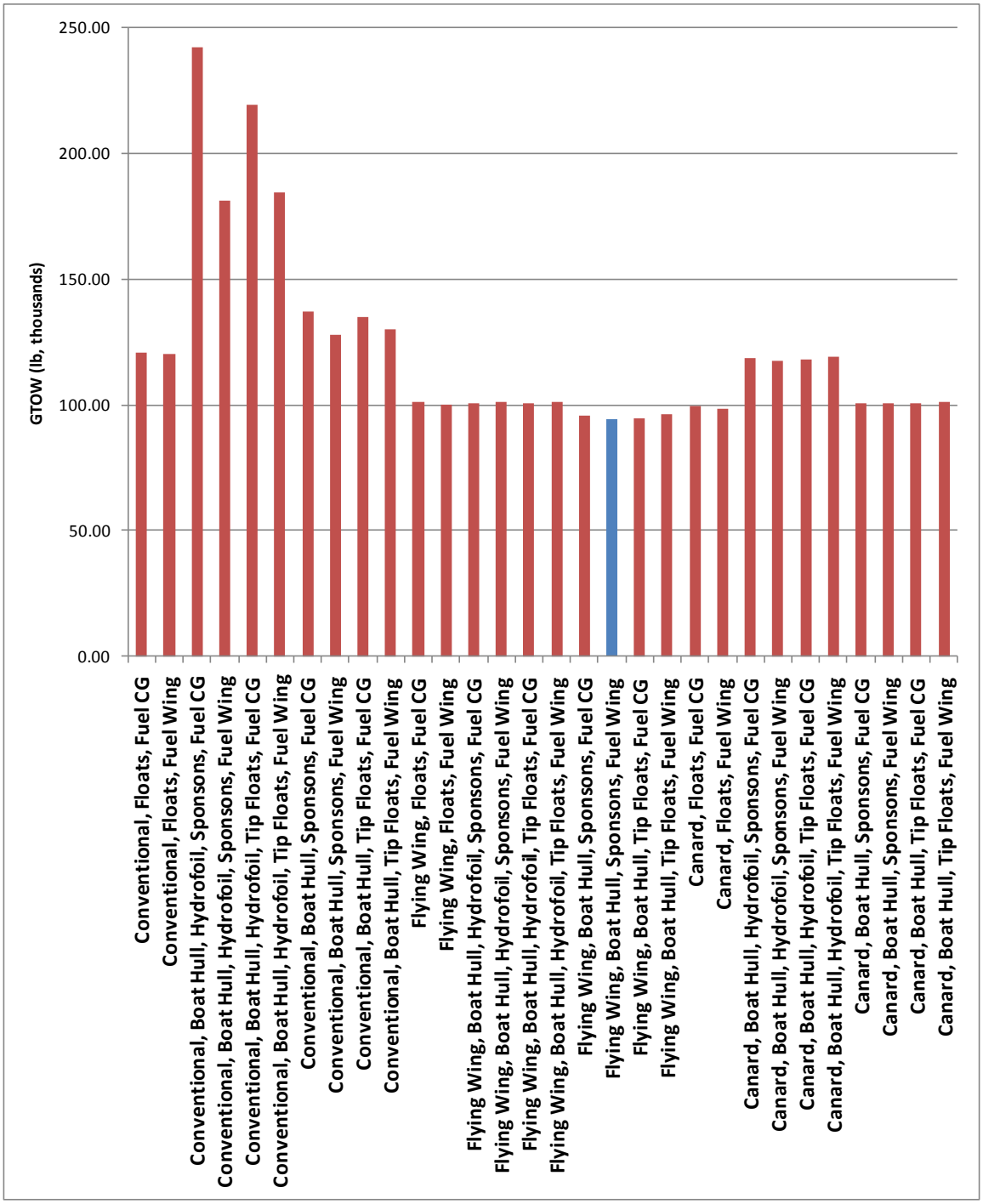

Figure 25: Optimization Results

The lowest weight configuration, 93,900.30 lb., found by the optimizer was a flying wing, with a boat hull and sponsons as the method of water operation, and fuel located in the wings.

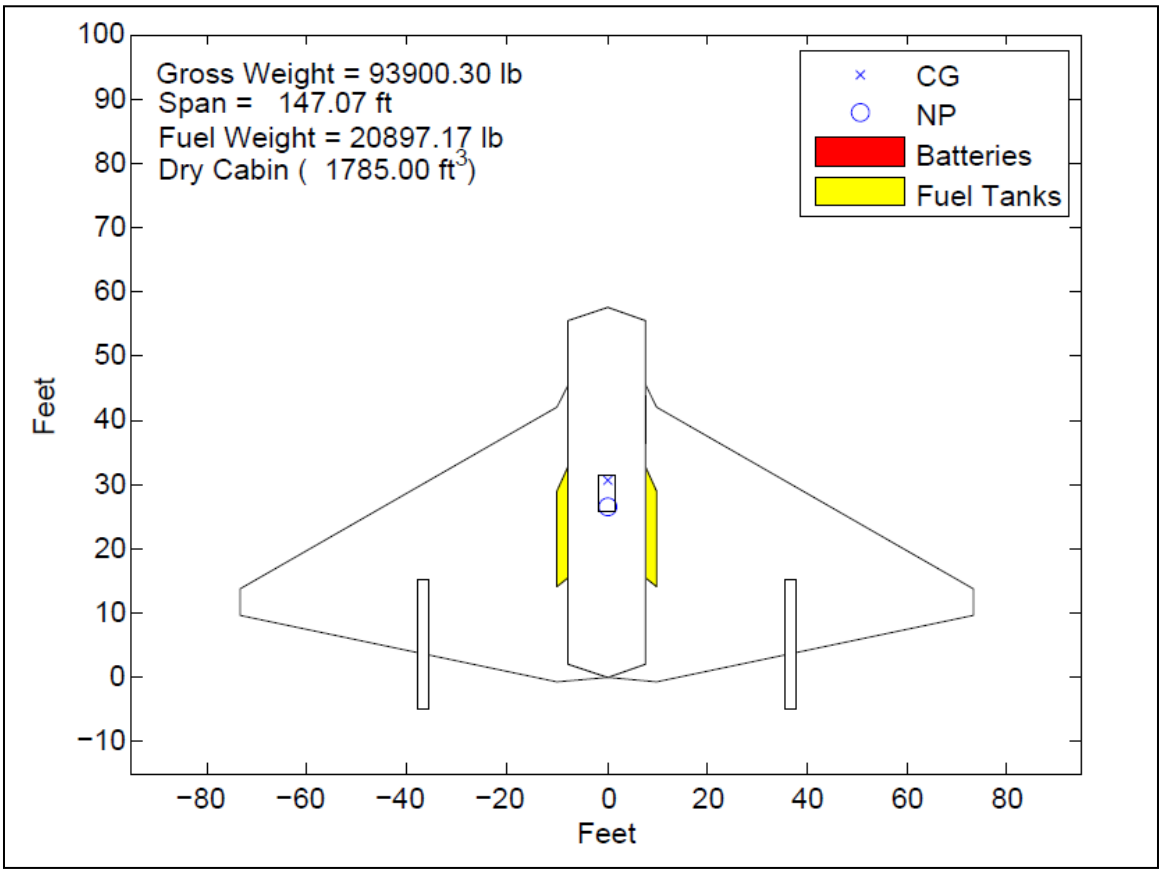

Figure 26: Final Optimized Design

A full breakdown of the final optimized aircraft, including its geometry, component weight breakdown, drag analysis, and performance data is provided in Appendix B.

4.3.1 Parametric Studies

A parametric study was conducted to examine how the changing of the stall speed of the aircraft would impact the aircraft's gross takeoff weight. The stall speed is important, especially for an amphibious aircraft, because it is indicative

of the takeoff and landing speeds of the aircraft. For example, Raymer [3] states that, for military applications, an aircraft must have an approach speed that is 1.2 times the stall speed. Having a low takeoff speed is especially important for an amphibious aircraft as the lower its takeoff speed, the less impact loads the aircraft will experience. As the aircraft accelerates to takeoff speed, the impact loads that are caused by wave slamming increase, especially on the forebody of the hull. Having a lower stall speed, and thus a lower load on the fuselage, will allow the aircraft to operate in rougher seas.

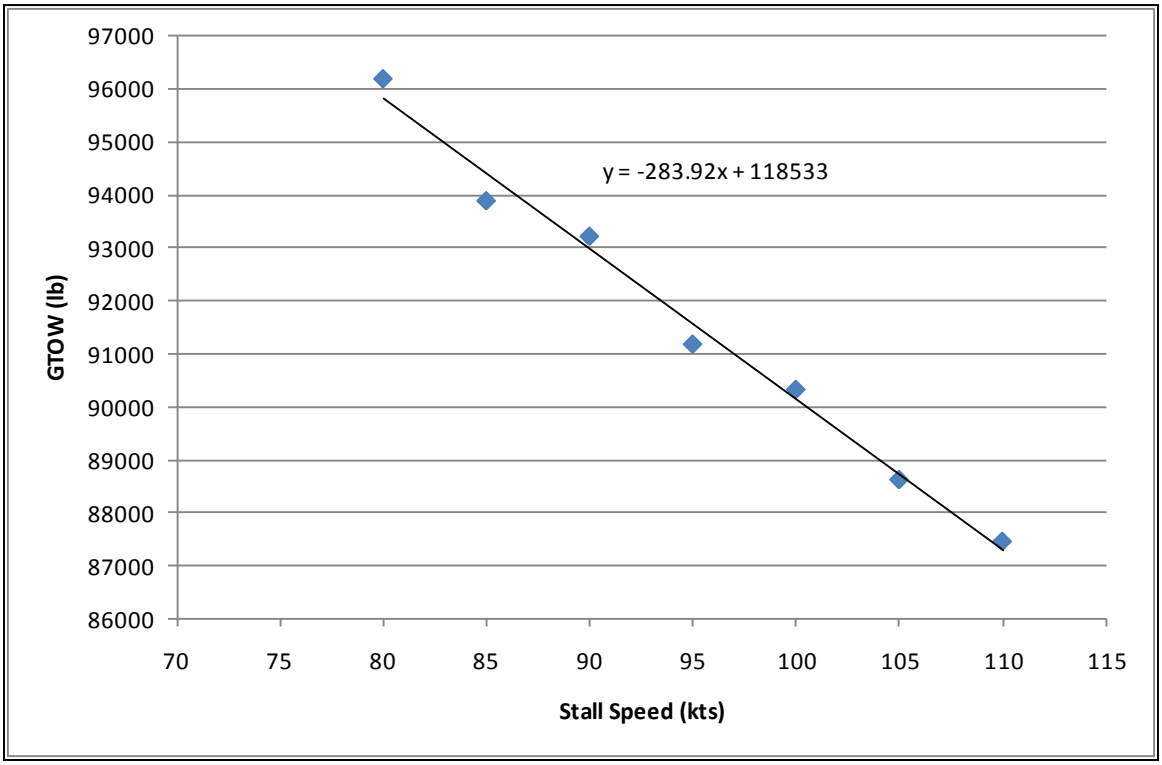

Figure 27: Stall Speed Parametric Study

The final aircraft in this optimization study was designed with a stall speed of 85 knots. The parametric study was done using the same input parameters as the final design, except the stall speed was varied from 80 knots to 110 knots in increments of 5 knots. The results of this study are shown in Figure 27. It can be seen that the stall speed and gross weight of the aircraft are inversely

proportional; as the stall speed decreases, the aircraft weight increases. This is because a decrease in an aircraft's stall speed requires an increase in wing area, and the larger wing area means an increased gross weight.

$$\frac{W}{S} = \frac{1}{2}\rho V_{stall}^2 C_{L,max} \tag{4.25}$$

This means that a tradeoff must be made, a lower stall speed, which gives the aircraft lower takeoff and landing speeds at the expense of a higher gross takeoff weight, or a higher stall speed, which decreases the gross takeoff weight but leads to increases in the speed at which the aircraft must takeoff and land. These increases in landing and takeoff speeds also correspond to increased difficulty for the pilot, as well as increased loads for the aircraft. As mentioned previously, for an amphibious aircraft to be able to operate at increased sea states, a low takeoff speed is required to decrease the loading on the hull due to wave slap. Most amphibious aircraft have stall speeds in the range of 55-100 knots. The Hughes H-4, the largest amphibious aircraft to fly, had a stall speed of 75.6 knots. It was felt that the 85 knot stall speed of the final optimized aircraft was a good balance between weight and takeoff and landing speeds. Lowering the stall speed further would have increased the gross takeoff weight an inacceptable mount, as the purpose of the optimization was to keep the aircraft weight low. At the same time, further increasing the stall speed would have significantly lowered the weight, but aircraft takeoff and landing performance would have suffered greatly as a result.

Chapter 5

Optimized Design Analysis and Testing

5.1 3-D CAD Model Development

With the preliminary design of the amphibious aircraft finalized, a 3-D model was constructed using SolidWorks. This model was used to construct a wind tunnel model as well as run Orca3D test cases. To obtain valid comparisons between the various analysis programs that were used to validate and improve the optimization code, it was very important to keep the 3-D model as true as possible to the final optimized design that was output by the sizing code.

While the output file specifies the exact geometry of all the lifting surfaces and engine nacelle, it only provides general dimensions for the fuselage and sponsons, although the code does have relative positions for all the components. This means that these last two components must undergo detailed design not specified by the optimization code.

The sizing code output specifies the length, width and height of the boat hull fuselage of the aircraft, but does not specify any further details, such as the shape of the bottom of the fore- and aftbody and the location of the step of the hull. Both of these design factors will affect the performance of the amphibious aircraft while it is on the water, especially in respect to its takeoff performance.

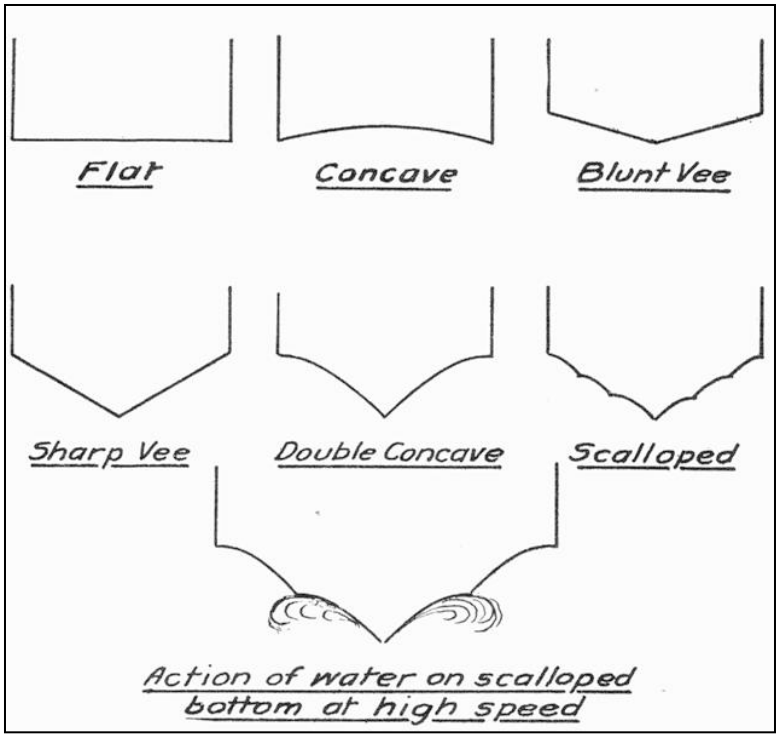

Figure 28: Various Types of Boat Hull Bottoms [45]

Figure 28 shows a variety of different bottom shapes for a boat hull or float aircraft. The bottom chosen will always be a compromise between quick takeoff and seaworthiness. According to Brimm [45], the flatter the bottom, the quicker an aircraft will takeoff in calm seas. But, in rougher seas, the flatter bottom will cause severe pounding due wave slam, which will likely make the aircraft takeoff slower than if it had a sharp bottom, which cuts through waves instead of going over them. This tendency to slam in rough water makes having a flat bottom hull a poor choice for an amphibious aircraft that is to operate littorally.

The double concave is desirable because it combines the advantages of the sharp and blunt "Vee". It has a sharp edge for entry into the water and cutting through waves yet still has a comparatively flat surface on which to plane. Another benefit of the double concave is that it deflects spray down and away from the fuselage and wings of the aircraft, which decreases loads and reduces the threat of water spray into the engines. The best overall compromise is the

double scalloped bottom. Not only does it share the advantages of the double concave, but as the aircraft increases speed and begins to plane, it begins to rise up out of the water, and is supported on successively lower scallops, reducing the water resistance as the speed increases. The forebody of the boat hull was chosen to have a double scalloped bottom, for its combination of reduced drag and spray characteristics as well as its ability to cut through the water, while the aftbody was designed to be a double concave because of its behavior during planing.

When water moves over the convex surface of the bottom of a seaplane, it creates suction in a normal direction to the surface. This means that as an amphibious aircraft accelerates through the water, the downward suction would increase with increasing speed. Takeoff performance would be greatly hampered by this. To prevent this from happening, a sharp step is placed into the hull to separate the water from the skin of the seaplane. The step is "ventilated," in that an air pocket generally forms behind it. As the speed of the aircraft increases, more air is drawn into this pocket and begins to extend back toward the stern, eventually completely separating the aft end of the hull from the water, which is called planing. The location of the step can vary, but is generally placed approximately 1/16 of the length of the hull behind the center of buoyancy. Langley [36] recommends that the depth of the step be approximately 5-8% of the breadth of the hull. For the 3-D model, the step was made to be 12 in. deep, or 6.5% of the breadth of the hull.

Sponsons are used to increase the transverse stability of the amphibious aircraft. The length, breadth and height of the sponsons, as well as their vertical placement on the fuselage, are specified by the sizing code. The sponsons are generally an airfoil shape, often with a blunt trailing edge. This is important

because if the aircraft happens to drift backwards there should be no tendency for the sponsons to be pulled under the water. Generally, the sponson is set at a slight incidence angle to present more bottom area than is necessary, which can lead to a quicker takeoff. It is also general practice to have the sponson extend beyond the step, but not interfere with the lines of the aftbody.

The sizing of rudders and elevons is specified by the sizing code, and follows historical trends. The rudders were sized to be 32% of the vertical tail chord length and span 90% of the vertical tail. The elevons were sized to be 30% of the wing chord and span 40% of the wingspan. The size and longitudinal position of the engines was specified by the sizing code, but their vertical placement was not. The engines were placed on the upper surface of the wing to protect them as much as possible from water spray.

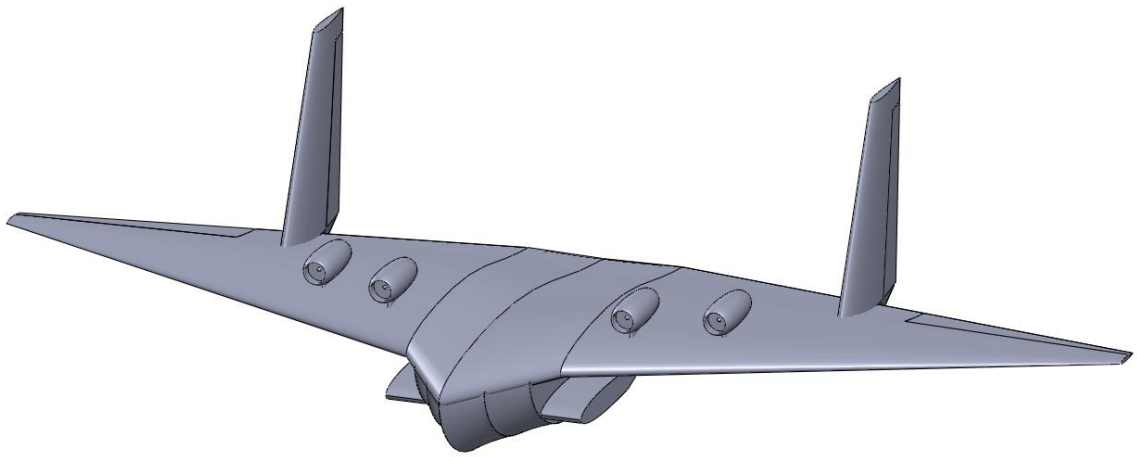

Figure 29: Final Optimized Aircraft Design

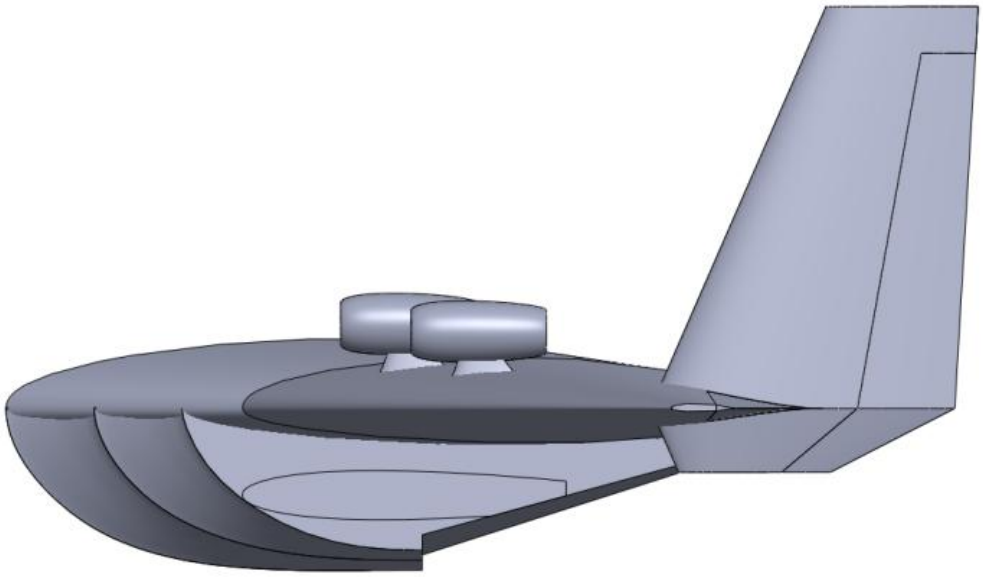

Figure 30: Right View of Optimized Design

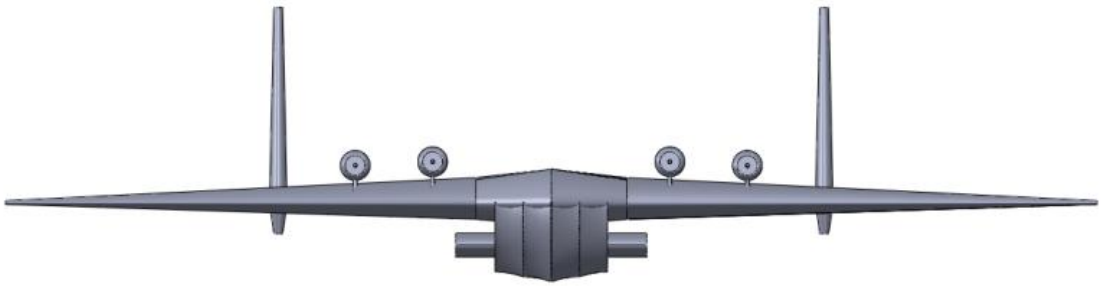

Figure 31: Front View of Optimized Design

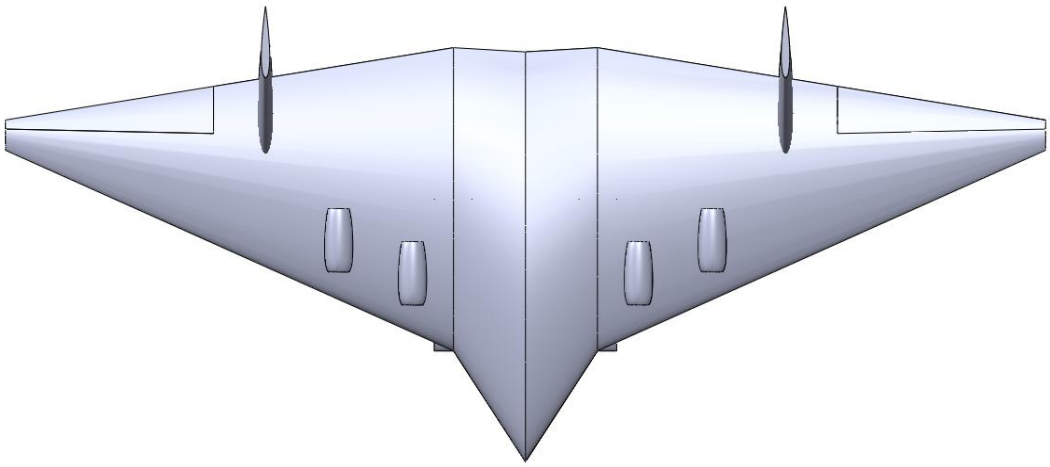

Figure 32: Top View of Optimized Design

5.2 Wind Tunnel Testing

Scale model testing was performed in Auburn University's 3 ft. X 4 ft. subsonic wind tunnel. This testing was used primarily to determine the accuracy of the drag estimates predicted by the sizing code, as well as to obtain data on the aerodynamic performance characteristics of the amphibious aircraft.

5.2.1 Model Design and Construction

A scaled down model was derived from the full scale 3-D model that had been constructed in SolidWorks. The model was scaled about its centroid to have a wingspan of 30 in. The factor used to scale the solid model from full size to having a 30 in. wingspan was .0169987081. This size resulted in acceptable model blockage, with a ratio of model frontal area to test section cross-sectional area of 2.1%. According to Barlow, Rae, and Pope [29], the maximum blockage factor of the tunnel should be less than 7.5% to obtain accurate results. The total

solid and wake blockage correction factor, also provided by Barlow, Rae and Pope [29], for an irregular shape is given by the following equation.

$$\varepsilon_t = \frac{1}{4}\frac{\text{model frontal area}}{\text{test section area}} \tag{5.1}$$

The total blockage correction factor for these tests was found to be .00524.

The wind tunnel model was constructed by Laser Reproductions using an additive manufacturing process known as stereolithography. Stereolithography uses a vat of resin that cures under ultraviolet (UV) light and a UV laser to build parts one layer at a time. For each layer, the beam traces the cross section of the part being built. The beam is controlled by a computer, which reads from a 3-D model of the part. Exposure to the UV light cures and solidifies the pattern traced into the resin and causes it to adhere to the layer below. The platform the model is being built on then descends the thickness of one layer and a fresh coat of the liquid resin is laid on top and the process repeats itself. Stereolithography allows for rapid, accurate prototyping of parts.

In order to prepare the model for the rapid prototyping process, the model fuselage/wing was divided into four sections: the right wing, left wing, forward fuselage and rear fuselage. The elevons and rudders were cut out of the wing and vertical tails, respectively. A cavity was made inside the parts to make room for an aluminum internal structure, which provides rigidity to the model during the testing as well as allows for a mating point to the pyramidal balance being used.

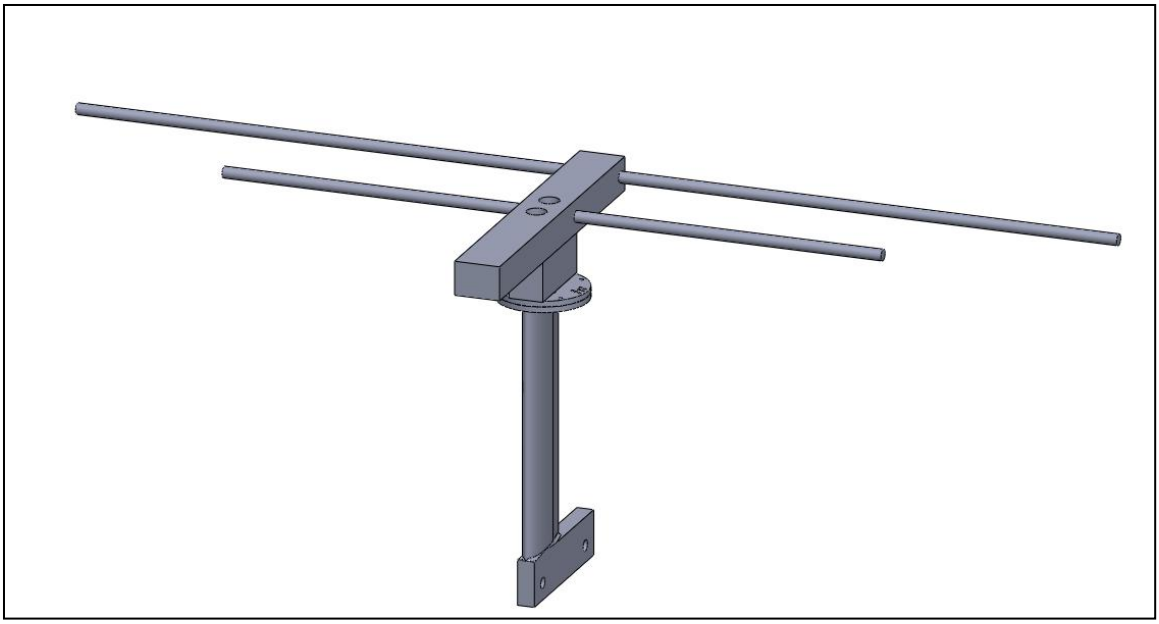

Figure 33: Internal Structure and Pyramidal Balance Mounting Blade

As shown in Figure 33, an aluminum blade was designed and fabricated to attach the model to the pyramidal balance. To reduce interference to the airflow over the model as well as drag created by exposed sections, the blade mount has the shape of a NACA 0016 symmetric airfoil. Also, the pyramidal balance is exposed inside the of the test section. To reduce the drag created by the mating of the blade mount to the pyramidal balance, a shroud was built, which was also in the shape of a symmetric airfoil.

So that yaw cases could be run, a metal disc (Figure 34) was made which had alignment holes for yaw angles of 2, 5, 10, and 11.5 degrees in the positive and negative directions. This disc was mounted to the model. Another disc was mounted to the top of the blade to align the yawing holes.

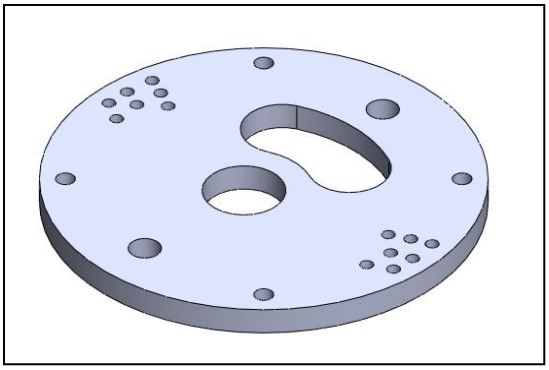

Figure 34: Yaw Alignment Disc

It was important to be able to test control surface deflection to determine if they had been properly sized during the optimization process. To accomplish this, steel brackets were made to hold the control surfaces at 0, 5, and 20 degrees in the positive and negative directions. These fit into matching slots in the control surfaces and wing surfaces.

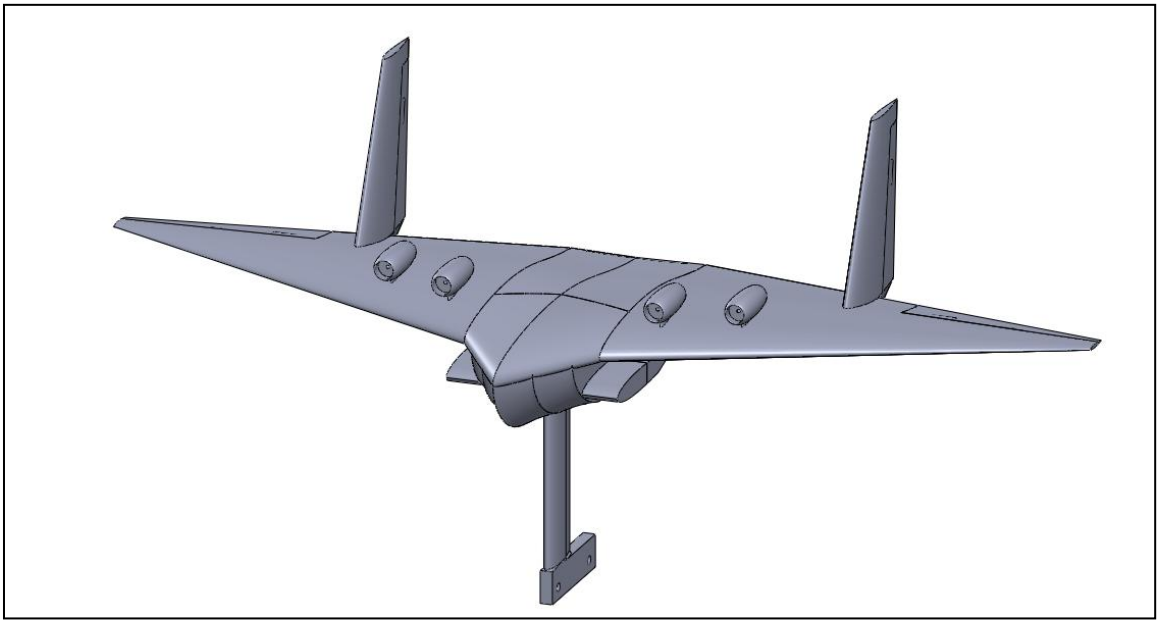

Figure 35: Wind Tunnel Model and Mounting Blade in SolidWorks

Figure 36: Wind Tunnel Model, Mounting Blade and Shroud

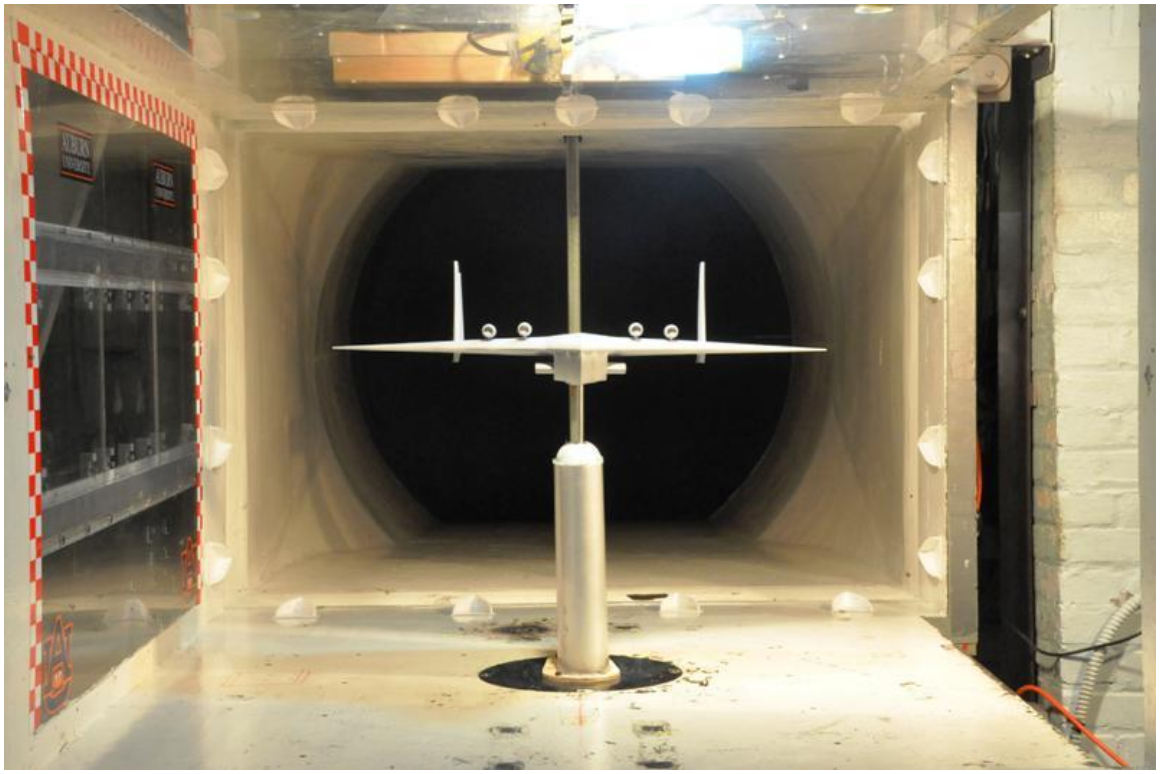

Figure 37: Model Installed in Wind Tunnel

5.2.2 Testing Setup

All of the test runs were conducted in the 3 ft. X 4 ft. closed circuit subsonic wind tunnel at Auburn University. The tunnel is capable of producing velocities up to 180 ft/s, although all test runs for this research were run at 100 ft/s. A pitot tube attached to a port in the test section is used to calculate the freestream velocity. Force and moment data were collected from a six component pyramidal balance, which reads normal, axial, and side forces as well as pitch, roll and yaw moments. This data was then processed using Labview data acquisition software. An accelerometer attached to the mounting blade was used to determine and control the model's angle of attack. Table 5 shows results of a calibration test of the accelerometer.

Table 5: Angle of Attack Calibration Data

Input Angle (deg)	Measured Angle (deg)
-14	-13.8
-12	-11.9
-10	-9.9
-8	-7.9
-4	-3.9
0	-0.2
4	3.9
8	8
12	11.9
16	15.8
20	19.9

The pyramidal balance was calibrated using a series of weights. A "calibration tree" was fabricated to assist in the calibration of the balance. The tree has five branches: one fore, one aft, one port, one starboard, and a vertical branch. The branches are marked with notches every inch, which allows accurate hanging of weights to ensure the induced moments are being calculated

correctly. The top branch allows weight to be placed directly over the pyramidal balance to calibrate the normal force. Table 6 shows the results from the initial calibration test performed on the balance. Raw data from the calibration run can be found in Table 6. No data point had greater than 4% error.

Table 6: Pyramidal Balance Calibration Data

Collected Data						
Normal Force Only						
Weight Applied (lb)	Normal Force (lb)	Axial Force (lb)	Side Force (lb)	Pitching Moment (lb-in.)	Rolling Moment (lb-in.)	Yawing Moment (lb-in.)
0.50	**-0.51**	0.02	0.00	0.00	0.01	0.00
1.00	**-1.00**	0.00	0.00	0.01	0.01	0.00
2.00	**-2.01**	0.01	0.00	0.03	0.02	0.00
Normal Force and Pitching Moment (Fore Branch at 6 in.)						
0.50	**-0.50**	0.00	0.00	**-0.25**	0.01	0.01
1.00	**-1.00**	0.00	0.00	**-0.50**	-0.01	0.00
2.00	**-1.99**	-0.01	0.00	**-1.00**	-0.02	0.00
Normal Force and Pitching Moment (Aft Branch at 6 in.)						
0.50	**-0.50**	0.01	0.00	**0.25**	0.01	0.00
1.00	**-1.00**	0.01	0.00	**0.51**	0.02	0.01
2.00	**-2.00**	0.02	0.00	**1.02**	0.04	0.02
Normal Force and Rolling Moment (Port Branch at 6 in.)						
0.50	**-0.50**	0.00	0.00	0.01	**0.26**	0.00
1.00	**-1.00**	0.00	-0.01	-0.01	**0.52**	0.00
2.00	**-2.00**	0.00	-0.01	0.02	**1.04**	0.00
Normal Force and Rolling Moment (Starboard Branch at 6 in.)						
0.50	**-0.50**	0.00	-0.01	0.01	**-0.26**	0.00
1.00	**-1.00**	0.01	0.00	0.01	**-0.50**	0.00
2.00	**-2.01**	0.01	0.01	0.03	**-1.00**	0.00

5.2.3 Testing Results

A series of wind tunnel tests were run to determine the drag and performance characteristics of the optimized aircraft. Tests were run at sideslip angles of -5, 0, +5, and +11.5 degrees. For each of these sideslip angles, the

rudders and elevons were deflected at angles of -20, -5, 0, +5, and +20 degrees to test rudder and elevator effectiveness. To test aileron effectiveness in roll, tests were also run with the elevons deflected in opposite directions, at 5 and 20 degrees. All of the tests were run at a test section velocity of 100 ft/s, and each test went through an angle of attack sweep from -14 to +20 degrees.

The baseline test was performed with no control surface deflections or sideslip angle and the results of this test are shown in Figure 38.

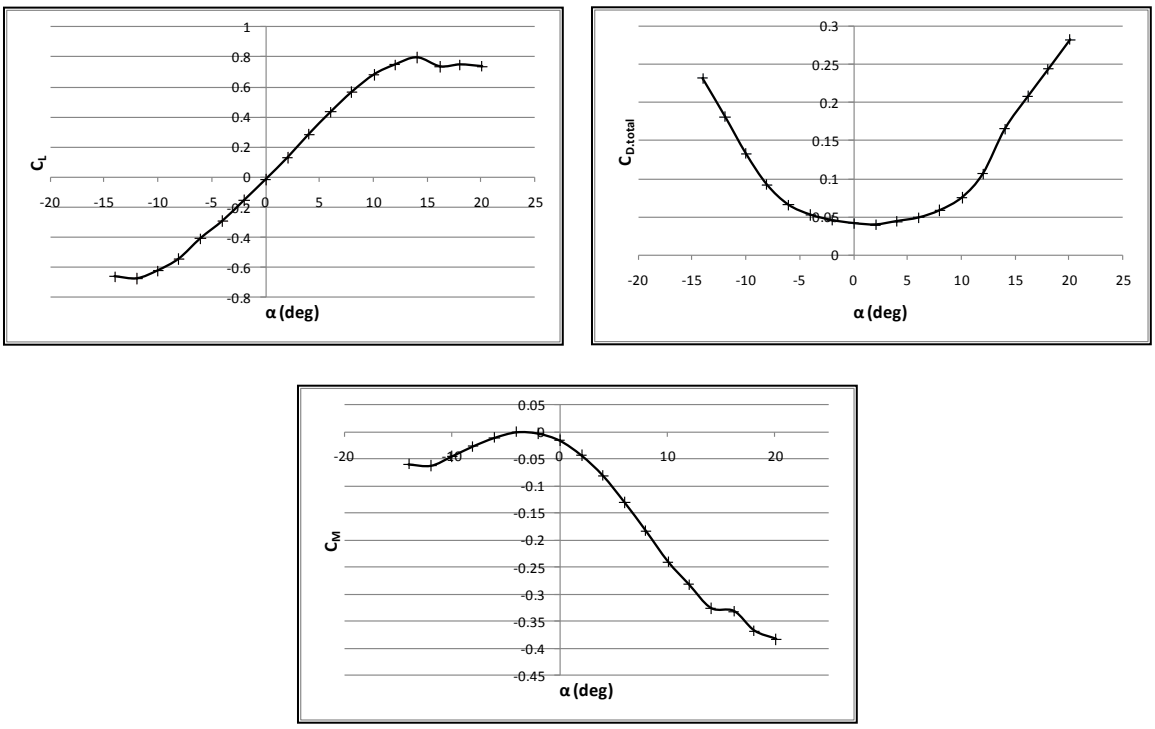

Figure 38: Baseline Wind Tunnel Results

From these baseline results, it is possible to determine if the aircraft has longitudinal static stability as well as find the change in lift, drag and pitching moment with respect to the change in angle of attack ($\frac{dC_L}{d\alpha}, \frac{dC_D}{d\alpha}, \frac{dC_M}{d\alpha}$, respectively). For an aircraft to have longitudinal static stability, the induced pitching moment due to a disturbance at a given angle of attack (e.g., due to vertical gusts, air turbulence, etc.) must be nose down as that will tend to restore the aircraft to its

original angle of attack. Using the sign convention of +x out the nose and +y out the right wing, a nose down pitching moment is assumed to be negative while a nose up pitching moment is assumed to be positive. Thus, for an aircraft to have longitudinal static stability in flight:

$$\frac{dC_M}{d\alpha} < 0 \tag{5.2}$$

where $C_M = \frac{M}{qS\bar{c}}$, q is the dynamic pressure, S is the model reference area, and $\bar{c}$ is the model reference length. The wing area and mean aerodynamic chord of the model were used as the reference area and length, 159.732 in^2 and 7 in. respectively.

Table 7: Baseline Derivatives

$\frac{dC_L}{d\alpha}$	4.1600 1/rad
$\frac{dC_D}{d\alpha}$	1.0256 1/rad
$\frac{dC_M}{d\alpha}$	-1.5126 1/rad

The results of this test show that the optimized aircraft is longitudinally statically stable since $C_{M\alpha} < 0$. These results also allow for the calculation of the lift curve slope, $C_{L\alpha}$, as well as $C_{D\alpha}$, the slope of the drag curve, which demonstrate how angle of attack effect lift and drag characteristics of the aircraft. The values for drag were adjusted for the Reynolds number scaling effects using the same process as was used for the Cessna 172 wind tunnel data.

A drag polar of this data can be used to find the minimum drag coefficient, C_{Dmin}, as well as the lift coefficient that corresponds to the minimum drag coefficient, $C_{Lmin\ drag}$.

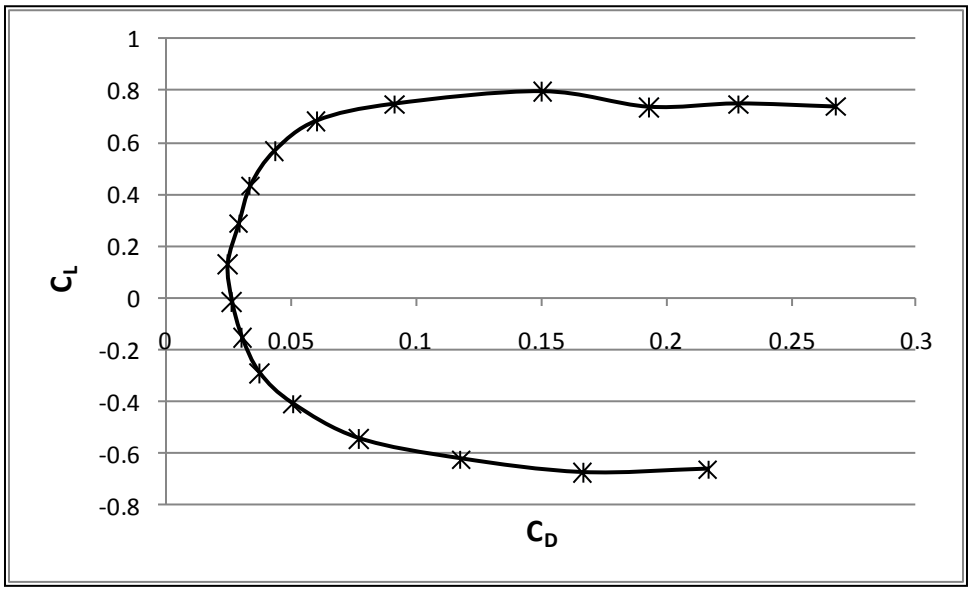

Figure 39: Drag Polar

The minimum drag coefficient of the aircraft is 0.02618 which corresponds to a lift coefficient of 0.1284.

The zero lift drag coefficient, C_{D0}, can also be found from the drag polar. For the optimized aircraft, C_{D0} is 0.02625. The drag area can be found by multiplying C_{D0} by the planform area of the full-size aircraft. Table 8 shows the drag comparison between the sizing code output and wind tunnel results.

Table 8: Sizing Code and Wind Tunnel Drag Comparisons

	C_{D0}	Drag Area (ft^2)
Sizing Code	0.01324	50.84
Wind Tunnel	0.02625	100.79

Much of this error is due to the lack of component detail in the sizing code drag estimations. For example, the sizing code analyzes the fuselage as though it were a cylinder. In order to make the wind tunnel model, an actual fuselage shape

had to be designed, and with that extra design detail comes additional drag. For instance, the step in the fuselage that is designed to reduce the fuselage's drag through the water is not accounted for in the sizing code, but it will cause boundary layer separation while in flight and result in an increase in drag. Other examples of additional drag due to detailed component design after the initial sizing optimization would be the scallops in the fore- and aft-body of the fuselage, as well as the blunt trailing edge of the sponsons which allows them to follow the lines of the aft fuselage. The sizing code also does not take into account flow interaction between the different components. For example, the fuselage and sponsons both contribute to "dirtying" the flow along the underside of the main wing to a width of approximately half the wingspan or more. This will lead to an increase in the measured drag and a decrease in the measured lift. Early boundary layer separation due to the low Reynolds numbers at which the wind tunnel tests were conducted may produce additional drag. This is primarily due to the improper transition from a laminar to a turbulent boundary layer. Laminar to turbulent transition occurs much earlier as a percentage of chord length on a full scale airplane than a scale model. While a laminar boundary layer may produce less drag than a turbulent boundary layer, the laminar boundary layer also has less energy, which makes it far more likely to separate when encountering corners or excessive roughness. Because of this, there may be separation occurring near the highly curved leading edge of the wing, which would lead to the formation of a laminar separation bubble over a large portion of the wing, which in turn increases drag.

Another important design point of the aircraft that can be pulled from the wind tunnel data is its trim characteristics. When an aircraft is trimmed, it is in a state of equilibrium where the pitching moment around the center of gravity of

the aircraft is zero. If the aircraft cannot be trimmed, then the aircraft cannot be flown. The trim criterion of an aircraft is:

$$C_{M,0} = 0 \tag{5.3}$$

where $C_{M,0}$ is the pitching moment coefficient at an angle of attack of 0 degrees. To determine if the aircraft can be trimmed, C_M vs. AoA curves are plotted for various elevon deflections, seen in Figure 40.

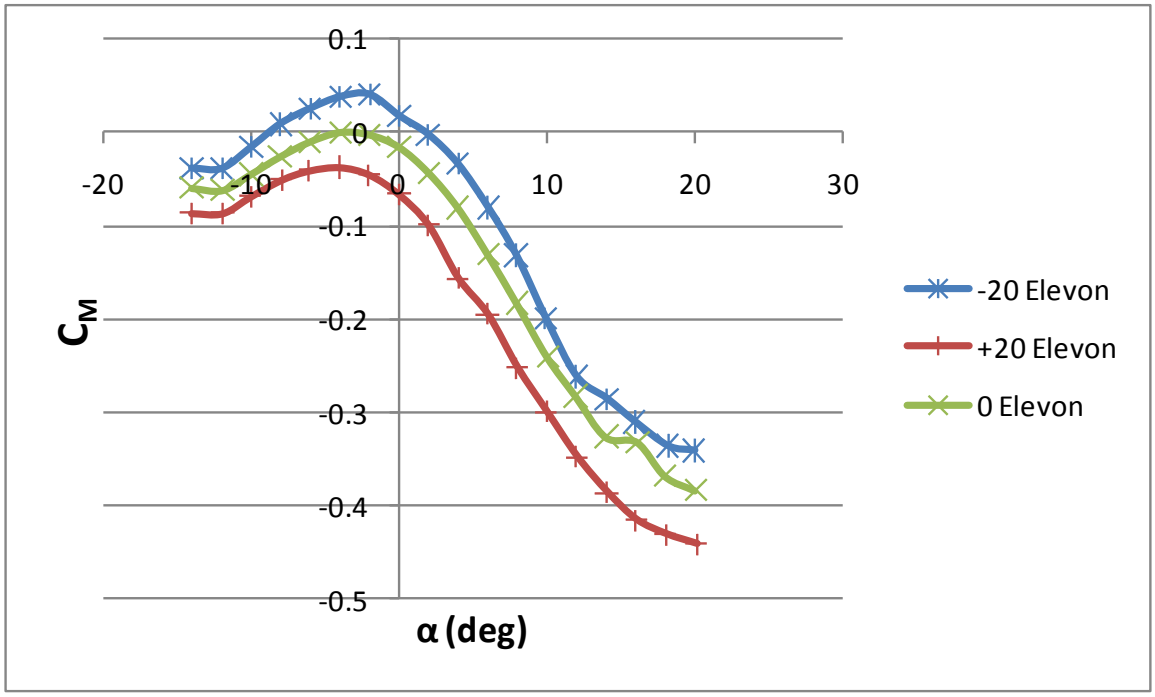

Figure 40: CM vs AoA for Elevator Deflection

These results show that the aircraft can meet the trim criterion. When the elevons are both deflected -20 degrees, which is an upward deflection in the standard axis orientation, the aircraft can be trimmed at approximately 2 degrees angle of attack.

To analyze the elevons' effectiveness as elevators, the change in lift, drag and pitching moment were plotted against the change in elevon deflection at multiple angles of attack.

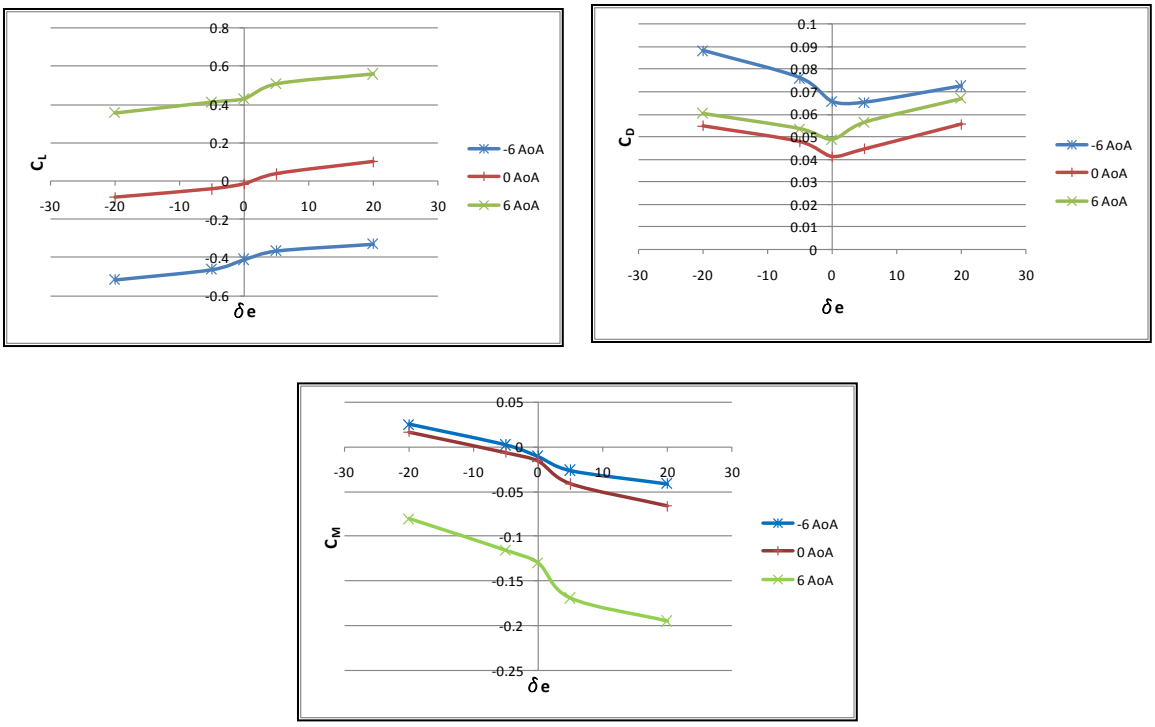

Figure 41: Elevator Deflection Results

As can be seen in Figure 41, the slopes of curves at different angles of attack are very consistent, which means that the aircraft will have consistent elevator effectiveness throughout most of it the angles of attack it will operating in. Table 9 shows the elevator deflection derivative values.

Table 9: Elevator Deflection Derivatives

$\frac{dC_L}{d\delta e}$	0.2808 1/rad
$\frac{dC_D}{d\delta e}$	-0.02864 1/rad
$\frac{dC_M}{d\delta e}$	-0.1260 1/rad

While the curves for the lift and moment coefficients vs. elevator deflection follow a basically linear trend, the drag curve slope transitions from negative to

positive at 0 elevator deflection. The drag derivative is taken from the negative elevator deflection angle data, as this shows the effectiveness of the elevators during trim conditions.

Longitudinal stability takes into consideration disturbances to the aircraft's angle of attack, and is assumed to only be in the vertical plane. Conversely, lateral stability is concerned with disturbances to the aircraft's sideslip angle, which is completely contained in the horizontal plane. While longitudinal stability is primarily concerned with the pitching moment, sideslip will always couple rolling and yawing motions.

For an aircraft to be laterally statically stable it must have an inherent capability to realign its flight path into a resultant wind if it is disturbed from steady, level flight. This is expressed mathematically as:

$$\frac{dC_n}{d\beta} > 0 \tag{5.4}$$

where C_n is the yawing moment coefficient and β is the sideslip angle. Wind tunnel tests were run at sideslip angles of 11.5, 5, 0, and -5 degrees. The plots in Figure 42 show the optimized aircraft's yaw moment, n, rolling moment, l, and side force, y, for the range of sideslip angles tested. All data in the following plots was taken with the aircraft at 0 AoA.

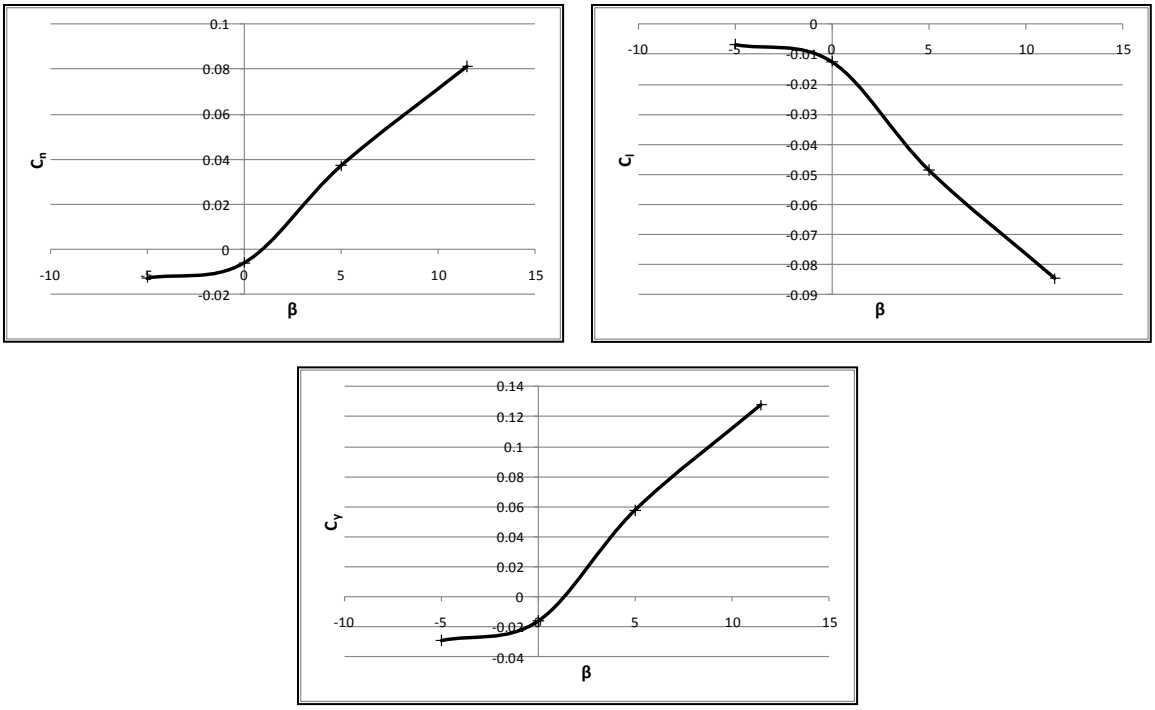

Figure 42: Lateral Static Stability Plots

The lateral stability derivatives are then calculated by finding the slope of the linear portions of the plots. Lateral stability derivatives are shown in Table 10.

Table 10: Lateral Stability Derivatives

$C_{n\beta}$	0.3437 1/rad
$C_{l\beta}$	-0.2864 1/rad
$C_{Y\beta}$	0.5730 1/rad

The optimized aircraft meets the criterion for being statically stable with respect to disturbances in sideslip angle since it has a positive value for $C_{n\beta}$.

Rudder effectiveness was evaluated by plotting the yawing moment, rolling moment and side force against rudder deflection at a range of angles of attack, shown in Figure 43.

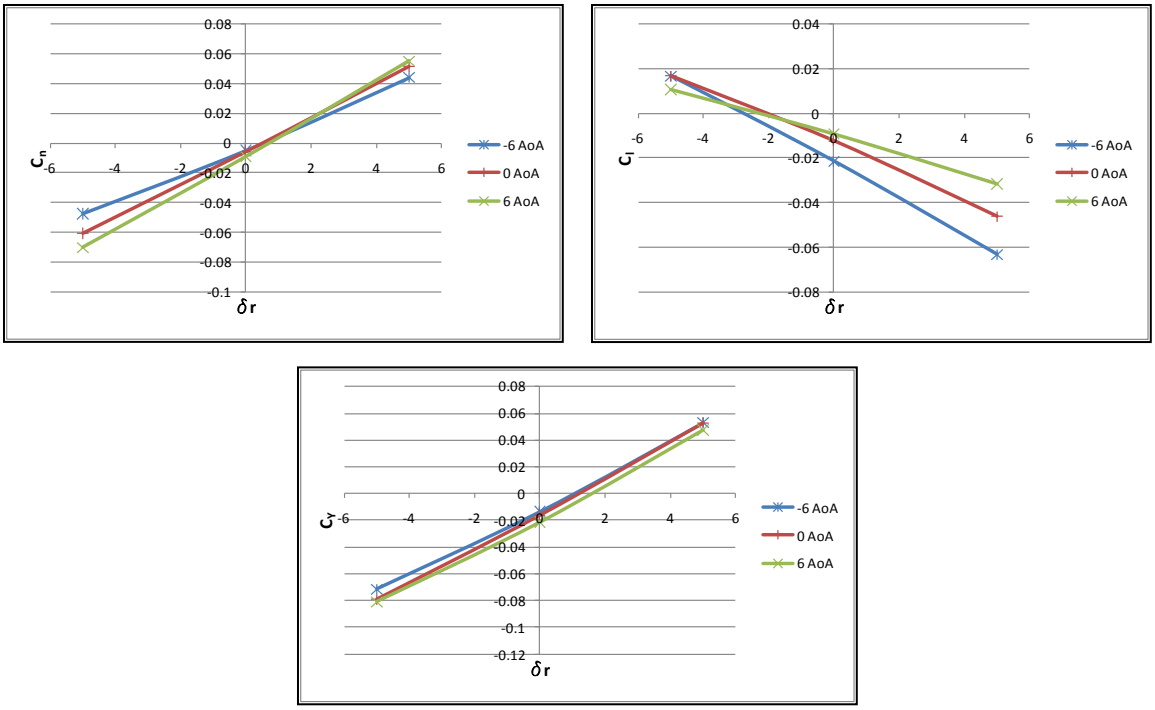

Figure 43: Rudder Deflection Results

As with elevon deflections, Figure 43, the slopes of curves at different angles of attack are very consistent, which means that the aircraft will have consistent rudder effectiveness throughout most of it the angles of attack it will operating in. Table 11 shows the rudder deflection derivative values.

Table 11: Rudder Deflection Derivatives

$\frac{dC_n}{d\delta r}$	0.6417 1/rad
$\frac{dC_l}{d\delta r}$	-0.3610 1/rad
$\frac{dC_Y}{d\delta r}$	-0.7563 1/rad

The derivatives are taken from the slopes of the linear portions of the rudder deflection curves, between -5 and +5 degrees of deflection.

To address the issue of early separation due to the low Reynolds numbers the wind tunnel tests are being conducted at, a round of further tests were conducted with a boundary layer transition strip. The purpose of the strip is to trigger the boundary layer to transition from laminar to turbulent flow by increasing the energy in the boundary layer, which will reduce drag and make the flow over the scale model more similar to a full scale test. Barlow, Rae and Pope [29] suggest multiple methods for implementing a transition strip. The method chosen for these wind tunnel tests was to use a layer of tape cut using pinking shears, leaving the edges in 90 degree triangles, which are placed pointing forward on the model. Layers of tape were added to reach the required transition strip height. The necessary height of the transition strip is given by:

$$h = \frac{12K}{Re} \tag{5.5}$$

where K is based on the model Reynolds number (600 for Re>100,000, 1000 for Re<100,000). With an average Reynolds number of approximately 300,000, K had a value of 600 for these tests. The total required height of the transition strip was found to be .025 inches. The tape had an approximate thickness of .012 inches, so two layers were used in the construction of the transition strip. At the suggestion of Barlow, Ray and Pope [29], the strip was placed at the 10% chord position on all lifting surfaces and engine nacelles. It was placed at the 20% length position on the fuselage. The full range of control surface deflections were rerun with the transition strip at 0 degree sideslip angle.

Figure 44: Wind Tunnel Model with Transition Strip

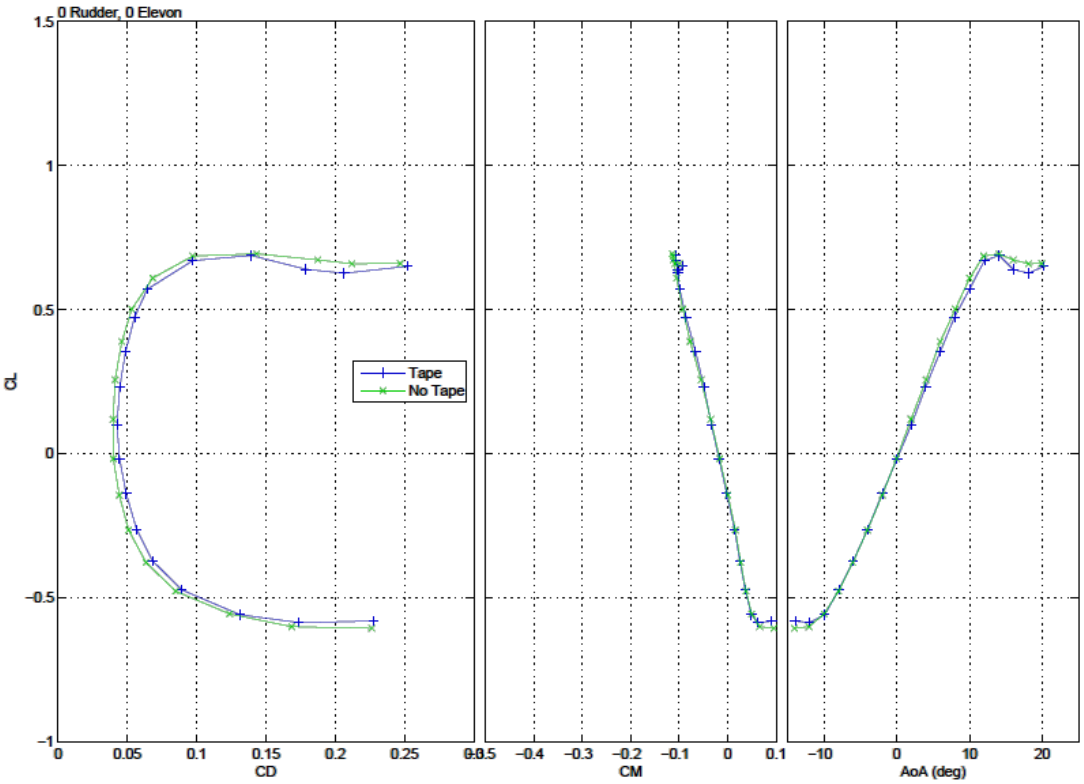

Figure 45: Transition Strip Result Examples (1)

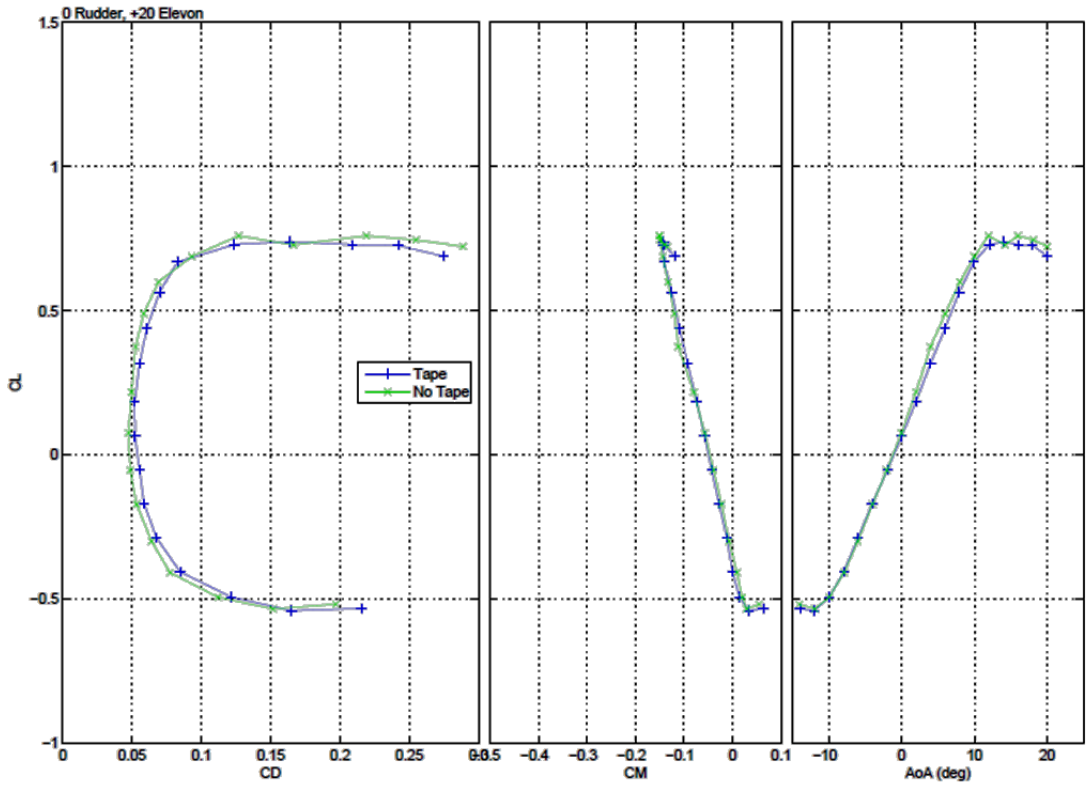

Figure 46: Transition Strip Result Examples (2)

Figure 45 and Figure 46 show two examples of the wind tunnel runs with transition strips compared to the same run without the strip. All the results found that the effect of the transition strip was negligible, with all tests showing a very slight increase in drag as opposed to the expected reduction.

To better understand the airflow over the plane, as well as to further assess the effectiveness of the transition strip, a flow visualization technique was employed. Fluorescent dye was mixed with S.A.E. 10W-30 motor oil and applied to the upper surface of the model. The model was then run in the wind tunnel at angles of attack of -5, 0, +5, +10, +15, and +20 degrees under an ultraviolet light. The purpose of these flow visualization runs was to find areas of flow separation and stagnation. In areas of separation, the oil will pool, as the local velocity of the air is very low. The oil will be blown off areas of the model where the flow is attached due to the high velocity of the local air, leaving a clean surface. These

tests were performed with and without the transition strip to visualize any effects it was having on the airflow over the model. All tests were run at a velocity of 100 ft/s.

Figure 47: Flow Visualization - 5 Degree AoA - No Strip

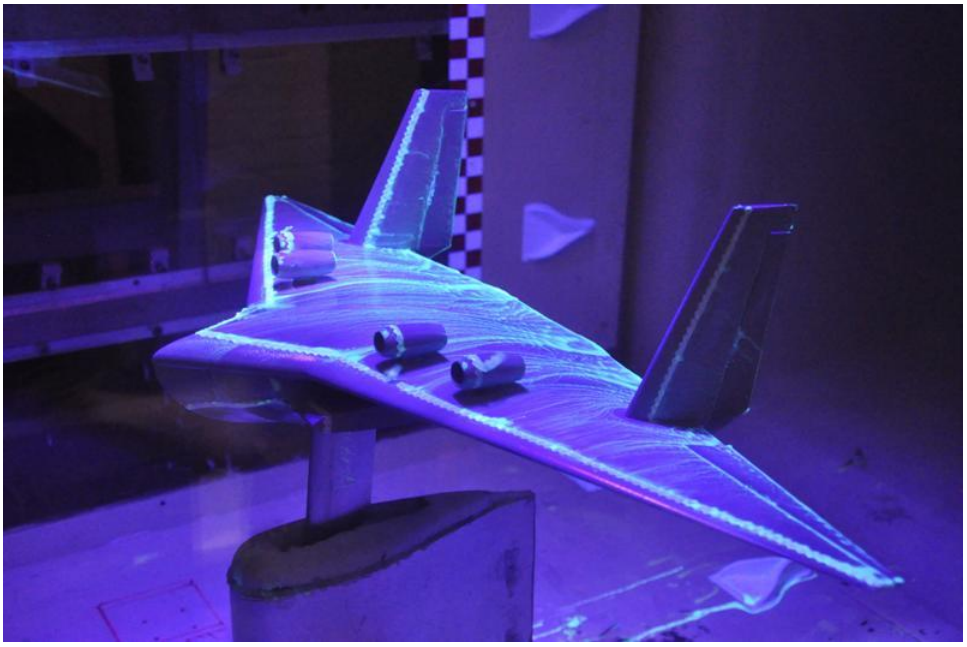

Figure 48: Flow Visualization - 5 Degree AoA - Strip

Figure 47 and Figure 48 show flow visualization results at 5 degrees AoA. It is apparent that the flow over the wing is separating prematurely in the run with no transition strip, as there is a large area just behind the leading edge of pooled oil. This is evidence of a laminar transition bubble, with the flow being detached until immediately before the elevon. In contrast, the run with the transition strip shows a clean flow over the whole chord length of the wing. This indicates that the transition strip was effective, even though it is not drastically influencing the data collected during the wind tunnel tests. The transition strip is putting energy into the boundary layer and causing it to stay properly attached over the whole wing.

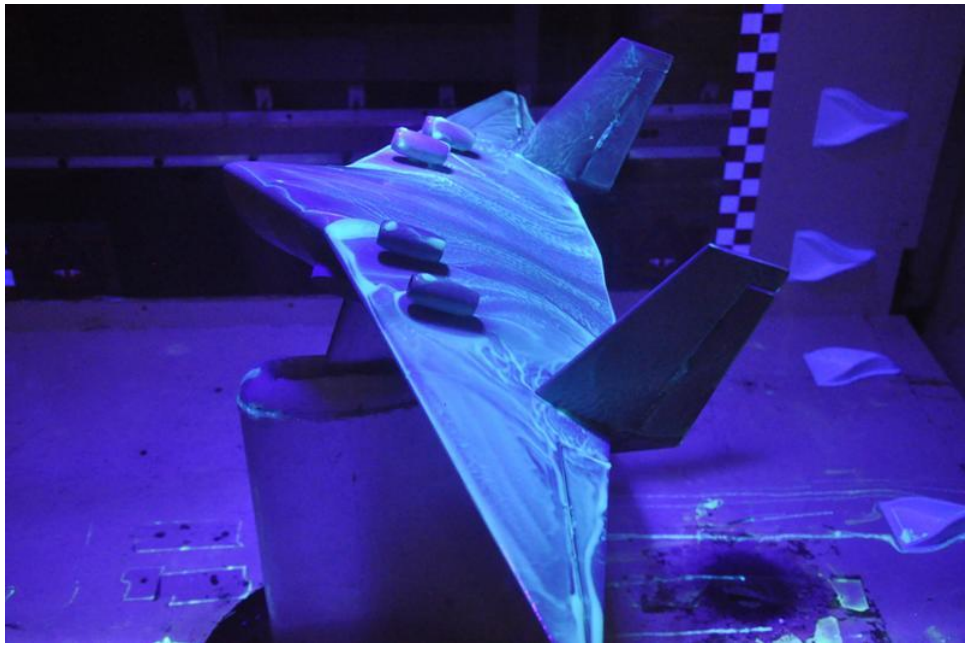

Figure 49: Flow Visualization - 20 Degree AoA - No Strip

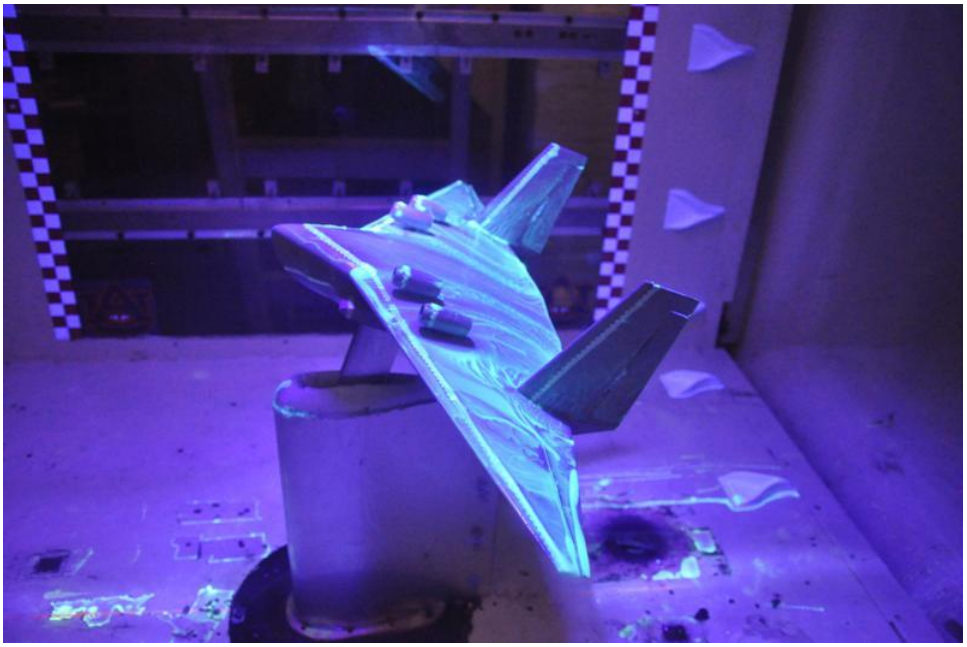

Figure 50: Flow Visualization - 20 Degree AoA - Strip

Figure 49 and Figure 50 illustrate the flow visualization results with the model at 20 degrees angle of attack, well into its stall regime. In this instance, with the flow over the wing completely stalled in both instances, there are no major differences between the visual results of the two model configurations, as would be expected. All results of the wind tunnel tests can be found in Appendix D.

5.3 Orca3D

Orca3D is a suite of tools used for naval architectural design and analysis that were written as a plug-in for the Rhinoceros 3-D modeling software. For this research, Orca3D was used to determine if the amphibious aircraft that was output by the sizing code had satisfactory longitudinal and transverse stability in the water. The stability of the aircraft in water is determined by the finding the location of the longitudinal and transverse metacenters. In order for a craft to be

considered stable, the metacenter must lie above the center of gravity. Nelson [8] has provided an empirical equation to determine if the aircraft will be sufficiently stable. The transverse and longitudinal metacenters should be approximately equal and have a minimum value of

$$GM = K\sqrt[3]{W} \tag{5.6}$$

where, GM is the distance from the metacenter to the center of gravity, W is the displacement of the aircraft in pounds, and K is a constant depending on the type of water operations employed by the aircraft. For a twin float plane, K=1.4, for a boat hull aircraft with wing tip floats, K=1, and for a boat hull aircraft with sponsons, K=0.75. For the optimized aircraft, with a weight of 93,900 lb. and a K value of 0.75, the required transverse and longitudinal metacentric heights are 409.07 in.

Classically, Simpson's Rule was the primary tool used in designing boat hulls. Simpson's Rule is a method of numerical integration and is governed by the following approximation:

$$\int_a^b f(x)dx \approx \frac{b-a}{6}\left(f(a) + 4f\left(\frac{a+b}{2}\right) + f(b)\right) \tag{5.7}$$

Using this approximation, a designer could calculate the location of the longitudinal and transverse metacenters, as well as the center of buoyancy and center of floatation, of a boat hull he or she was designing.

Computer aided hull design has been becoming more and more prominent in recent years, as it offers advantages over traditional design methods. A majority of CAD representations of a boat hull are curve-surfaces. Orca3D generates a mesh from this surface to calculate most of its hydrostatic and stability parameters. With a mesh created, Orca3D then uses Simpson's Rule to numerically integrate between the mesh nodes. This method of computer aided

mesh generation and numerical analysis leads to more accurate results, as it doesn't rely on a manually calculated station model, which has a tendency to miss local hull features, such as discontinuities and curvature changes.

According to Sederberg [46], the de-facto CAD standard for representing curved surfaces since the 1970's has been the non-uniform rational B-splines (NURBS). NURBS are the only free-form surface type supported in the IGES file format, which is the most popular format for transferring data between CAD software. Unfortunately, NURBS have two weaknesses that impact hull design and analysis. First, to make hull optimization and analysis easier, it is helpful to have the entire hull represented with a single surface. Unfortunately, due to NURBS needing rectangular topography when making its mesh, a complicated hull cannot always be represented by a single surface. Secondly, control node points for a NURBS surface must lie in a rectangular grid, which leads to there being a large number of control points that carry no significant geometric information and only serve to increase calculation time. Figure 51 illustrates the drawbacks of the NURBS model. The personal watercraft depicted is divided into 13 surfaces in order to maintain the required rectangular topography. Also, many of the nodal points are unnecessary and are merely included to satisfy rectangular shape constraints.

To address the limitations of using NURBS to model complex boat hulls, T-Splines were introduced. T-Splines are not limited to a rectangular geometry, which significantly reduces the number of superfluous points needed to complete the mesh as well as make the modeling of a complex body with a single surface possible. In the NURBS mesh, all the interior control points have a valence of four, which means that all the interior control points touch four edges. A T-Spline mesh (T-Mesh) allows control points to have valence other than four.

These points are shown in Figure 51 as yellow dots. The ability to have nodal points with different valence values gives T-Splines the ability to model any surface using a single T-Mesh. T-Splines were integrated into Orca3D to decrease calculation time as well as increase the accuracy of the calculations by removing discontinuities between surface meshes.

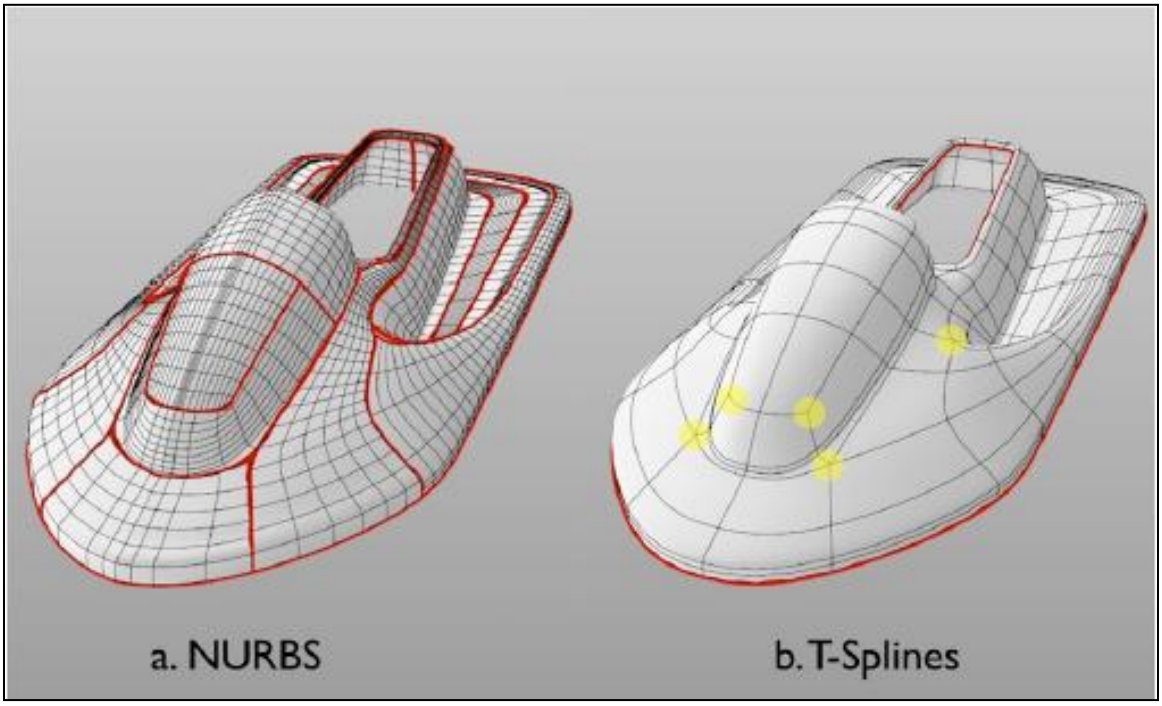

Figure 51: Personal Watercraft Modeled as a NURBS and a T-Spline [46]

5.3.1 Model

The 3-D model of the full scale optimized design was transferred from SolidWorks to Rhinoceros in the form of an IGES file. While Rhinoceros only accepts NURBS meshes, the Orca3D addon allows for the creation of a single surface T-Spline mesh when performing stability and hydrostatic parameter calculations.

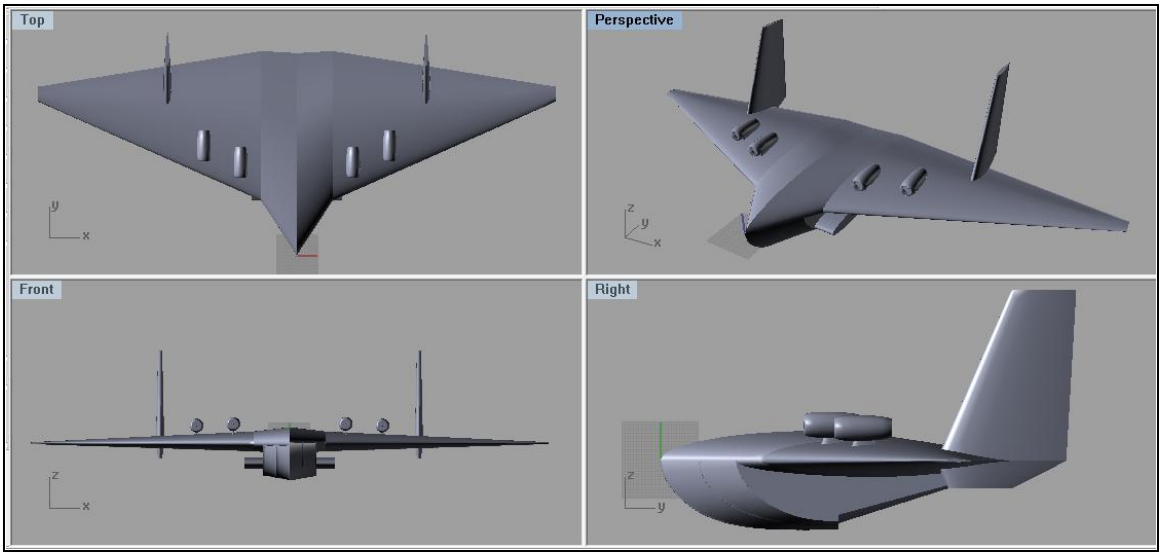

Figure 52: Rhinoceros Model

5.3.2 Results

Orca3D requires a number of parameters in order to output meaningful hydrostatic and stability data. The hull was designed so that the load water line (LWL) would have the aircraft sitting at a 1.5 degree trim angle in the water. During the design of the hull shape, the load water line was specified and the hull shaped to provide that attitude while in the water. Considerations were taken to keep the vertical tails out of the water during water operations. Next, Orca3D needs an input weight (GTOW = 93,900 lb.) and heel angle. The heel angle was set to 0 degrees. Finally, a vertical center of gravity position was needed, which directly affects the metacentric height of the craft, as that is the distance from the metacenter to the center of gravity. From this data and given aircraft geometry, Orca3D outputs the location of the center of buoyancy and center of floatation. It also gives the lateral and longitudinal metacentric heights, and draws in a waterline on the model to give a visual representation of its attitude in the water (Figure 53).

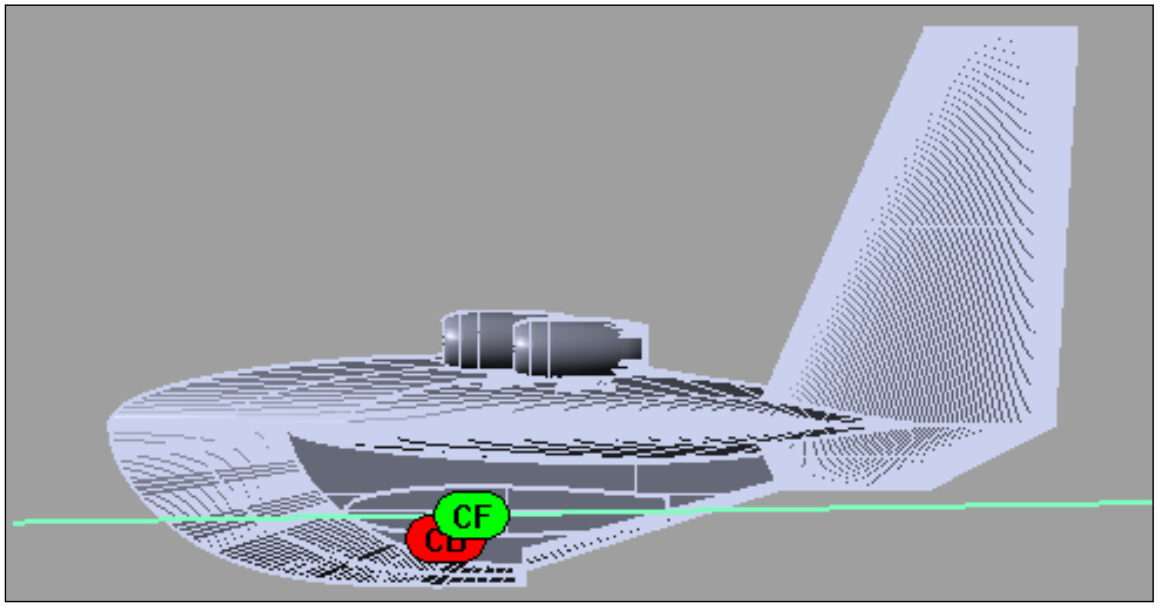

Figure 53: Orca3D Results with Virtual Waterline

The longitudinal and transverse metacentric heights were calculated to be 299.03 and 168.89 in. respectively. While these results do indicate positive stability of the aircraft in the water at this attitude, these values do not meet the metacentric height value of 409.07 in. that has been found to provide the best results historically. In order to address stability in the longitudinal direction, the shape or the dimensions of the fuselage must change. The nose of the fuselage would need to be blunter, which would provide an increase in surface area that is in contact with the water. Reducing the slope of the fuselage aft of the step to the trailing edge of the wing would also make the aircraft sit deeper in the water, which would lead to an increase in longitudinal stability. Unfortunately, there is little room to move the step forward, which would decrease the aft slope, and the height of the fuselage is set by the optimization code, so that cannot be reduced to provide more sink to the aircraft. In the transverse direction, the width of the sponsons will have to be increased to increase the lateral stability of the aircraft. Accordingly, they may be able to be made thinner to keep the volume constant,

which could lead to a reduction in airflow interference on the lower surface of the wing. Possible methods of implementing changes and improvements to the sizing code to attempt to correct these problems will be discussed further in Chapter 6.

5.4 Athena Vortex Lattice (AVL)

An estimate of the aerodynamic characteristics of the optimized amphibious aircraft was obtained through the use of the Athena Vortex Lattice aeroprediction code, which is a vortex-lattice method. For this research, AVL was used primarily to test for any unstable dynamic modes as well as to verify that the vertical tails and various control surfaces were properly sized. AVL only considers the wing and tail surfaces of the aircraft to predict vehicle aerodynamics. No contributions from the fuselage are considered. Because of this a drag correction must be added into the .avl file. A zero-lift drag correction of 0.01324 was added to the drag data corresponding to the zero-lift drag coefficient output by the sizing code.

AVL employs an extended vortex lattice model for lifting surfaces and can use a slender body model for fuselages and nacelles. The vortex lattice method (VLM) is a numerical method which models lifting surfaces as an infinitely thin sheet of discrete vortices to compute lift and induced drag. The influence of wing thickness and fluid viscosity is neglected.

The VLM models the wing segments as a finite number of panels. A horseshoe vortex is placed at the quarter chord of each panel and consists of a bound vortex on the panel and two semi-infinite trailing vortices extending from the ends of the bound vortex to infinity aft of the panel. Each panel has a control

point placed at the three quarter chord and centered between the two trailing vortices.

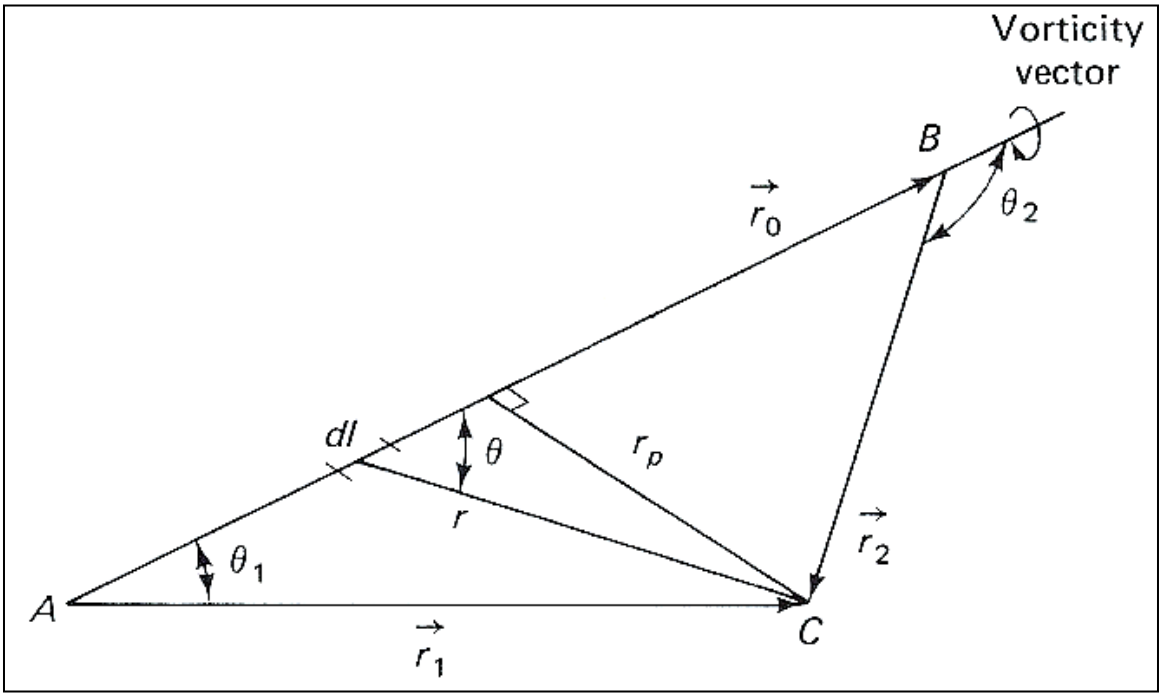

Figure 54: Velocity Induced by a Finite Length Vortex Segment [47]

If a horseshoe vortex has a strength of Γ_n with a length of dl, then the velocity induced by the vortex is found using the Law of Biot and Savart.

$$\overrightarrow{dV} = \frac{\Gamma_n(\vec{dl}\,x\vec{r})}{4\pi r^3} \tag{5.8}$$

Referring to Figure 54, the magnitude of the induced velocity is then found to be:

$$dV = \frac{\Gamma_n \sin\theta dl}{4\pi r^2} \tag{5.9}$$

Integrating this equation results in the total induced velocity produced by the vortex filament:

$$V = \frac{\Gamma_n(\cos\theta_1 - \cos\theta_2)}{4\pi r_p} \tag{5.10}$$

Next, to obtain the strength of the vortex at the surface of the wing, a boundary condition is applied. This condition states that the flow does not pass

through the wing but maintains tangency with the wing surface. Bertin [47] suggests using the following approximation for the tangency condition if the wing has a modestly sloped camber line:

$$w_n - v_m \tan\phi + U_\infty \left[\alpha - \left(\frac{dz}{dx}\right)_m\right] = 0 \tag{5.11}$$

A 2-D, planar approximation can be further applied if the wing is of modest thickness

$$w_m + U_\infty \sin\alpha = 0 \tag{5.12}$$

or, when dealing with only small angles of attack:

$$w_m = -U_\infty \alpha \tag{5.13}$$

As derived by Bertin [47], the downwash at collocation point i on panel j can be summed to find the total downwash at i, w_{mi}.

$$w_{mi} = \frac{1}{4\pi} \sum_j C_{ij} \Gamma_j \tag{5.14}$$

Substituting this into the tangency condition for small angles of attack to find equations for the vortex strengths:

$$\frac{1}{4\pi} \sum_j C_{ij} \Gamma_j = -U_\infty \alpha \tag{5.15}$$

The definition of the lift coefficient, using the Kutta-Joukowski theorem [27] is:

$$L' = \rho U \Gamma = \frac{1}{2} \rho U^2 2 b C_L \tag{5.16}$$

Solving for C_L and substituting in the equation for Γ:

$$C_L = \frac{-4\pi}{b} C^{-1} \alpha = C_{l\alpha} \alpha_e \tag{5.17}$$

Finally, solving for the effective angle of incidence, α_e

$$\alpha_e = \frac{-4\pi}{b C_{l\alpha}} C^{-1} \alpha \tag{5.18}$$

This equation provides a relationship between the effective angle of incidence of each segment and the aerodynamic angle of attack of the segment, which includes the influence of one segment on another. The effective angle of attack can then be used to find the total lift and moment of each segment.

5.4.1 Model

AVL requires a .avl file and a .mass file to run. The .avl file specifies the geometry of the lifting surfaces and the .mass file specifies masses and inertias as well as sets the units for the run cases.

The .avl file requires an operating Mach number, as well as wing area, mean aerodynamic chord length and wingspan. The user is required to choose a reference position, which is important for properly placing the lifting surfaces. In the case of this research, it was simplest to make the reference point at global coordinates of (0, 0, 0), which coincides with the nose of the aircraft. The .avl file also requires the location of the center of gravity as measured from the reference point.

Next, wing surfaces are constructed in sections. The .avl file is set up so that you initially divide the surface into panels in the spanwise and chordwise directions, which influence the speed and accuracy of the AVL results. The location of the leading edge of the root chord of the wing surface is input next with respect to the reference point. The surface is divided into sections which define the chord length at some spanwise location along the surface. At least two sections are necessary to complete a surface, a root and tip section. The position of the leading edge of the section chord as well as the length of the section chord is input into the .avl file. AVL then interpolates between the two sections to

build a surface. Due to this interpolation, a new section must be created at each change in sweep angle of the surface, as well as a section where a control surface begins or ends. AVL also allows the user to input the shape of the airfoil camber line, which by default is a flat plate, by creating a .DAT file with coordinates for a unit airfoil shape. This input can be used to introduce twist to the wing, by having different camber profiles at different wing sections and having AVL interpolate between the two shapes. Control surfaces may also be designed into wing surfaces by placing a hinge deflection on section planes. First, a control variable, such as aileron, elevator, rudder, etc., must be defined. Next, the location of the hinge as a percentage of section chord length must be input, as well as a gain variable, which determines the sensitivity of the control surface. This gain variable allows for the contribution of more than one control variable at a section. For example, if an aileron and flap are put into a section, with gains of 1.0 and 0.3 respectively, the overall deflection will be:

$$\delta_{\text{Total}} = 1.0\delta_{\text{a}} + 0.3\delta_{\text{f}} \tag{5.19}$$

The .mass file defines many aircraft parameters, such as mass and moments of inertia, as well as simulation parameters, such as the units of length, mass and time as well as the value of gravitational acceleration and a baseline operational density.

Two .mass files and three .avl files were made for this research. Each one contained surfaces representing the main wing and two vertical tails, as well as elevons and rudders. The fuselage was not modeled, as it cannot be accurately drawn in AVL. One of each file type was made for baseline run cases, which were cruise, stall, cruise into a crosswind and stall into a crosswind. A separate .mass and .avl file had to be made for the run cases where the aircraft was cruising in ground effect. The third .avl file was made to demonstrate the effects

of modifications to the control surfaces on trim and stability characteristics. Full .avl and .mass files can be found in Appendix E.

5.4.2 Results

A total of five cases were run for the optimized aircraft. Table 12 shows the details of the cases that were run.

Table 12: AVL Run Cases

	Velocity (ft/s)	Altitude (ft)	Density (slug/ft^3)	β (deg)
Stall	157.85	0	0.002377	0
Cruise	280.00	20,000	0.001267	0
Ground Effect	255.20	0	0.002377	0
Crosswind Stall	157.85	0	0.002377	11.5
Crosswind	280.00	20,000	0.001267	11.5

To simulate flying into a crosswind, the sideslip angle β was set to 11.5 degrees. The stall cases were run at takeoff speed, with is 10 percent greater than stall speed. The constraint put on all the models was to trim the aircraft at the given speed and flight conditions, which meant setting the roll, pitch and yaw moments to 0. When run, AVL would calculate necessary control surface deflection angles to trim the aircraft as well as identify any dynamic maneuvering flight modes the aircraft may have.

Table 13 shows the results of the AVL trim scenarios. The elevons function as both ailerons and elevators for the purpose of this analysis. Roskam [48] states that acceptable control surface deflections must be within the stall limits of the control surface, which is approximately 25 degrees.

Table 13: AVL Results - Control Surface Deflections for Trim

	Aileron	Elevator	Rudder
Stall	0.000	66.045	0.000
Cruise	0.000	36.919	0.000
Ground Effect	0.000	25.128	0.000
Crosswind Stall	10.129	69.056	31.263
Crosswind	6.038	39.961	21.637

The results of these runs show that there are unacceptable amounts of elevon and rudder deflection needed to trim the aircraft. The elevon is under-sized for functioning as an elevator in all cases, and the rudder not effective enough for the case of stalling in a crosswind. The elevons are adequately sized to trim the rolling moment though.

In addition to a trim analysis, AVL also conducted an eigenvalue analysis to identify unstable maneuvering modes, such as Dutch roll, short period, phugoid, and spiral modes.

Dutch roll is one of the basic flight dynamic modes, and is the result of a yaw-roll coupling moment. It is usually excited by use of the ailerons and rudder. Dutch roll tendencies, which coincide with increases in an aircraft's restoring rolling moment, can be increased by: the placement of wings above the center of gravity, increasing wing sweep, and increasing wing dihedral. Often times, Dutch roll modes will experience decreased damping when an aircraft increases altitude. To counteract the Dutch roll mode, many aircraft employ yaw dampers to artificially increase Dutch roll stability [39].

Short period modes describe the rapid pitching of an aircraft around its center of gravity. The mode is generally very quickly damped out, with a period lasting only a few seconds. The period is short enough that the airspeed of the aircraft does not have time to change, and instead functions as just a variance in angle of attack.

The phugoid mode is a long period mode that consists of an aircraft pitching up and down as well as gaining and losing altitude, but experiencing very little change in angle of attack. This mode can last for minutes in large aircraft, such as the optimized amphibious aircraft being used in this research. While the damping of phugoid modes is normally weak, the period is long enough that the pilot usually can correct for this motion without problem.

The spiral mode is a lateral-directional mode involving roll-yaw coupling with a very long period. A divergent spiral mode may be excited by a gust, which applies a small initial roll angle, which produces a small sideslip. This sideslip then causes a yawing moment. If the aircraft lacks sufficient dihedral stability and yaw damping, the spiral mode will be unstable and the aircraft will continue to turn while maintaining its sideslip and yaw angle. This spiral will get continuously steeper and if left unchecked, a high speed spiral dive will result. Usually, this mode happens relatively slowly, allowing for pilot correction. In order to be spirally stable, an aircraft must have sufficient dihedral, which will increase roll stability, and a sufficiently long vertical tail moment arm, which will increase yaw damping.

Results of the eigenvalue analysis for the optimized aircraft are in Table 14. They show level 1 and level 2 damping and frequency requirements for a cargo aircraft [49].

Table 14: Eigenvalue Analysis Results for Optimized Aircraft

Flight Condition	Eigenvalues Real	Imag	Natural Freq.	Damping	Time to Double	ωζ	Mode	Level 1 Req.			Level 2 Req.		
Stall	-1.64	2.76	3.21	0.51		1.64	Short Period	0.3 ≤ ζ ≤ 2.0			0.2 ≤ ζ ≤ 2.1		
	-0.15	1.41	1.41	0.11		0.15	Dutch Roll	ζ ≥ 0.08	ωζ ≥ 0.15	ω ≥ 0.4	ζ ≥ 0.02	ωζ ≥ 0.05	ω ≥ 0.4
	-1.79	0.00											
	0.00	0.00											
	-0.04	0.21	0.21	0.17		0.04	Phugoid	ζ ≥ 0.04			ζ ≥ 0		
Cruise	-1.69	0.00											
	-0.14	1.48	1.49	0.09		0.14	Dutch Roll	ζ ≥ 0.08	ωζ ≥ 0.15	ω ≥ 0.4	ζ ≥ 0.02	ωζ ≥ 0.05	ω ≥ 0.4
	-1.13	2.86	3.08	0.37		1.13	Short Period	0.3 ≤ ζ ≤ 2.0			0.2 ≤ ζ ≤ 2.0		
	0.00	0.00											
	-0.01	0.11	0.11	0.11		0.01	Phugoid	ζ ≥ 0.04			ζ ≥ 0		
Ground Effect	-3.40	0.00											
	-0.29	1.73	1.75	0.17		0.29	Dutch Roll	ζ ≥ 0.08	ωζ ≥ 0.15	ω ≥ 0.4	ζ ≥ 0.02	ωζ ≥ 0.05	ω ≥ 0.4
	-2.22	3.60	4.23	0.52		2.22	Short Period	0.3 ≤ ζ ≤ 2.0			0.2 ≤ ζ ≤ 2.1		
	0.00	0.00											
	-0.01	0.11	0.11	0.09		0.01	Phugoid	ζ ≥ 0.04			ζ ≥ 0		
Crosswind Stall	-1.58	2.67	3.10	0.51		1.58	Short Period	0.3 ≤ ζ ≤ 2.0			0.2 ≤ ζ ≤ 2.1		
	-1.76	0.00											
	-0.16	1.41	1.42	0.11		0.16	Dutch Roll	ζ ≥ 0.08	ωζ ≥ 0.15	ω ≥ 0.4	ζ ≥ 0.02	ωζ ≥ 0.05	ω ≥ 0.4
	-0.04	0.20	0.20	0.18		0.04	Phugoid	ζ ≥ 0.04			ζ ≥ 0		
	0.00	0.00											
Crosswind	-1.55	3.61	3.92	0.39		1.55	Short Period	0.3 ≤ ζ ≤ 2.0			0.2 ≤ ζ ≤ 2.1		
	-1.74	0.00											
	-0.15	1.47	1.48	0.10		0.15	Dutch Roll	ζ ≥ 0.08	ωζ ≥ 0.15	ω ≥ 0.4	ζ ≥ 0.02	ωζ ≥ 0.05	ω ≥ 0.4
	-0.01	0.11	0.11	0.13		0.01	Phugoid	ζ ≥ 0.04			ζ ≥ 0		
	0.00	0.00			496.52		Spiral	T2s > 12			T2s > 8		

The results of the eigenvalue analysis show that the aircraft achieves level 1 stability for all dynamic flight modes except for Dutch roll during cruise, where falls in the high range of level 2 stability. Level 1 stability refers to an aircraft having flying qualities that are clearly adequate for the required mission while level 2 stability refers to an aircraft having flying qualities are adequate to accomplish the mission but may require additional pilot workload or may cause degradation in mission effectiveness. Neither level requires exceptional pilot skill or technique to return the aircraft to level, steady flight [49]. The level 2 Dutch roll stability requirement encountered during cruise could be corrected with the addition of an artificial yaw damper, which would increase yaw stability and provide level 1 stability for the aircraft in all dynamic flight modes.

Analysis through AVL shows that the primary problem of the optimized aircraft configuration is the large control surface deflections necessary to trim the aircraft under stall and crosswind flight conditions. To assist in finding an optimal size for the control surfaces, a parametric study was conducted varying what percent of the wing chord the control surfaces would occupy. The tests

were performed using the crosswind at stall speed test scenario, which yielded the worst results overall. The results of that study are shown in Figure 55.

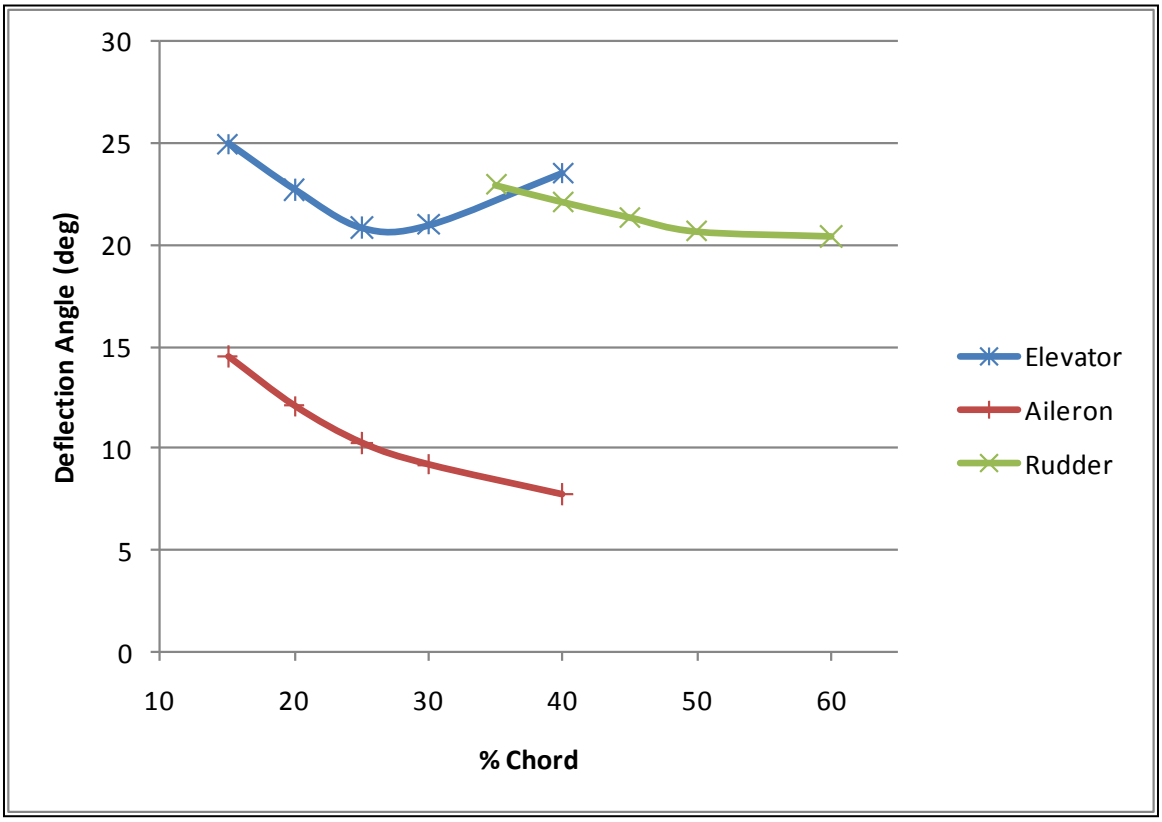

Figure 55: Control Surface Sizing Parametric Study

The results of this parametric study show that the elevator is most effective when it is approximately 27 percent of the total chord while the aileron's performance continually increased with an increase in its size. The rudder performance sees a steady increase as the percentage of chord increases until it is approximately 50 percent of the chord length of the wing, where the added benefits of more rudder become negligible. In accordance with the findings of the parametric study, the elevons were resized to be 27% of the local chord, a decrease in size, and the rudder was increased in size to 50% of the local chord. Also, having to deflect the elevons almost 37 degrees to trim during steady cruise flight indicates that the elevons alone do not have enough size to control the

aircraft properly. To compensate for this, a dedicated elevator was added between the vertical tails to assist the elevons in controlling the pitch of the aircraft. Like the elevons, the elevator was sized at 27% chord. Table 15 shows the results of the aircraft with revised control surface sizing.

Table 15: Modified Control Surface Deflections for Trim

	Aileron	Elevator	Rudder
Stall	0.000	18.942	0.000
Cruise	0.000	10.585	0.000
Ground Effect	0.000	6.915	0.000
Crosswind Stall	9.586	20.223	21.742
Crosswind	5.431	11.498	16.794

With the increase in size of the rudder, slight decrease in size of the elevons and addition of a dedicated elevator, the control surface deflections for all run cases have been brought under the stall threshold of 25 degrees.

To ensure that the change in control surface sizing, along with the addition of an elevator, had not caused the aircraft to develop an unacceptable dynamic stability mode, an eigenvalue analysis was run again. Results of this analysis are in Table 16.

Table 16: Eigenvalue Analysis Results for Modified Aircraft

Flight Condition	Eigenvalues Real	Imag	Natural Freq.	Damping	Time to Double	ωζ	Mode	Level 1 Req.			Level 2 Req.		
	-0.21	1.43	1.45	0.15		0.21	Dutch Roll	ζ ≥ 0.08	ωζ ≥ 0.15	ω ≥ 0.4	ζ ≥ 0.02	ωζ ≥ 0.05	ω ≥ 0.4
	-1.67	0.00											
Stall	-1.63	2.76	3.21	0.51		1.63	Short Period	0.3 ≤ ζ ≤ 2.0			0.2 ≤ ζ ≤ 2.1		
	0.02	0.00			39.84		Spiral	T2s > 12			T2s > 8		
	-0.04	0.21	0.21	0.18		0.04	Phugoid	ζ ≥ 0.04			ζ ≥ 0		
	-0.16	1.53	1.54	0.10		0.16	Dutch Roll	ζ ≥ 0.08	ωζ ≥ 0.15	ω ≥ 0.4	ζ ≥ 0.02	ωζ ≥ 0.05	ω ≥ 0.4
	-1.73	0.00											
Cruise	-1.59	3.72	4.05	0.39		1.59	Short Period	0.3 ≤ ζ ≤ 2.0			0.2 ≤ ζ ≤ 2.0		
	0.01	0.00			76.92		Spiral	T2s > 12			T2s > 8		
	-0.01	0.11	0.11	0.12		0.01	Phugoid	ζ ≥ 0.04			ζ ≥ 0		
	-0.31	1.78	1.81	0.17		0.31	Dutch Roll	ζ ≥ 0.08	ωζ ≥ 0.15	ω ≥ 0.4	ζ ≥ 0.02	ωζ ≥ 0.05	ω ≥ 0.4
	-2.91	0.00											
Ground Effect	-2.74	4.37	5.15	0.53		2.74	Short Period	0.3 ≤ ζ ≤ 2.0			0.2 ≤ ζ ≤ 2.1		
	0.01	0.00			83.70		Spiral	T2s > 12			T2s > 8		
	-0.01	0.11	0.11	0.11		0.01	Phugoid	ζ ≥ 0.04			ζ ≥ 0		
	-1.57	2.66	3.09	0.51		1.57	Short Period	0.3 ≤ ζ ≤ 2.0			0.2 ≤ ζ ≤ 2.1		
	-1.62	0.00											
Crosswind Stall	-0.23	1.43	1.44	0.16		0.23	Dutch Roll	ζ ≥ 0.08	ωζ ≥ 0.15	ω ≥ 0.4	ζ ≥ 0.02	ωζ ≥ 0.05	ω ≥ 0.4
	-0.04	0.20	0.21	0.19		0.04	Phugoid	ζ ≥ 0.04			ζ ≥ 0		
	0.02	0.00			32.32		Spiral	T2s > 12			T2s > 8		
	-1.54	3.61	3.92	0.39		1.54	Short Period	0.3 ≤ ζ ≤ 2.0			0.2 ≤ ζ ≤ 2.1		
	-1.70	0.00											
Crosswind	-0.17	1.49	1.50	0.11		0.17	Dutch Roll	ζ ≥ 0.08	ωζ ≥ 0.15	ω ≥ 0.4	ζ ≥ 0.02	ωζ ≥ 0.05	ω ≥ 0.4
	-0.02	0.11	0.11	0.14		0.02	Phugoid	ζ ≥ 0.04			ζ ≥ 0		
	0.01	0.00			57.63		Spiral	T2s > 12			T2s > 8		

The control surface changes resulted in large improvements of Dutch roll stability. All dynamic flight modes now comply with level 1 requirements for military cargo aircraft. While all modes are now compliant, the changes to the control surface have resulted in the addition of a spiral mode to every run case. Fortunately, the time to double is very slow in all cases and is easily corrected through pilot input.

Chapter 6

Conclusions and Suggestions for Further Work

6.1 Improvement of Sizing/Optimization Methods

The purpose of this research effort was to analyze the optimization and sizing methodology used in the creation of a preliminary design for an amphibious aircraft and to make suggestions about ways it can be improved. It is very difficult, if not impossible, to create an aircraft that will function perfectly after the first design iteration. This is why it is called a preliminary design. A preliminary design aims to address as many design issues as possible in an expedient manner before beginning detailed design work on the remaining problems. A good preliminary design process can save a company vast amounts of money because design problems are caught early. The further into the design and manufacturing process a product is when a major problem is found in its design, generally the more expensive that problem is to correct. If weaknesses can be found in the sizing and optimization process used in the preliminary design of an amphibious aircraft, efforts can be made to address these issues, and develop a more accurate and efficient preliminary design process in the future.

While the main focus of this paper was the suggestion of possible improvements that could be made to the sizing and optimization methods used, there were many positive results found throughout the course of this research work.

First, the results of the validation work done on the sizing code were very promising. The geometric parameters predicted by the sizing code for Lockheed C-130-H and Cessna 172-R validation cases were very accurate. The drag

predicted for Cessna 172 with and without floats was also quite accurate, with the percent error for the two cases being approximately 4% and 10%, respectively. The sizing code reasonably predicted the size of floats necessary for a Cessna 172, with the largest error in the predicted float geometry being the depth of the float with 6.7% error.

Also, the optimized aircraft was found to be statically stable in flight in both the longitudinal and lateral directions through the analysis of wind tunnel test results. This demonstrates the effectiveness of the penalty functions put in place to produce a stable aircraft. Also, there were no unacceptable dynamic maneuvering modes found through analysis using AVL. The damping of all maneuvering modes was found satisfy the level 1 flying quality requirements, except for a Dutch roll mode during cruise conditions which just missed qualification for level 1 stability. Both level 1 and 2 flight quality requirements are acceptable for aircraft, requiring no exceptional piloting ability to return the craft to level and steady flight. If needed, the stability in the cruise Dutch roll mode could be increased to meet level one requirements through the addition of a yaw augmentation device.

6.1.1 Drag Estimation

Drag estimation in the sizing code seemed to be quite inconsistent. When the Cessna 172 was used for validation with and without floats, the percent error without floats was within 4%, and the percent error with floats was within 10%. In contrast, when the optimized model was tested in the wind tunnel, the results showed almost a 50% error between the wind tunnel and sizing code results. The method of drag calculation used by the sizing code is imperfect. It doesn't

take into account interference from one component to another. There is also the issue of the shape of the individual components. The sizing code does not have a detailed model of components such as the fuselage and sponsons. It does not account for drag due to flow separation at the step of the fuselage. It does not consider the blunt trailing edge of the sponsons that was put in place to allow them to follow the contour lines of the aft part of the fuselage. It also does not include the additional drag due to the scalloped cut outs in the fore and aft sections of the fuselage. One method of improving aerodynamic prediction could be the inclusion of a vortex panel code into the design code. This would completely replace the current aerodynamic calculations made in the sizing code and could hopefully help improve drag predictions [50].

6.1.2 Stability During Water Operations

A second issue that arose with the sizing code was found during the analysis of its lateral and longitudinal stability on the water using Orca3D. While the aircraft was found to be stable in both the lateral and longitudinal directions, it did not have the levels of metacentric heights that have been recommended through the gathering of empirical data from existing amphibious aircraft.

This is a difficult problem to solve, as it requires the designer to know the shape of the fuselage in order to calculate its center of buoyancy and metacentric heights. This requires a more detailed design than is currently being used and may not be feasible with the current approach. On the other hand, if a panel method could be implemented that could handle the complex geometries involved in detailed boat hull design, then it is possible that that geometry could

have a sectioning method performed on it inside the sizing code to predict its on-water performance. Alternatively, if a panel method or something similar enables the creation of a 3-D hull geometry inside the sizing code, it could be exported into Orca3D through a subroutine built into the sizing code to analyze its stability during water operations. Once Orca3D has analyzed the model, the output data could be fed back into the sizing code and checked for appropriate levels of stability and the geometry could be adjusted from there. The option of exporting to an outside program would seem to be very time intensive though, and may not be feasible when going through the many design iterations necessary during the optimization process.

If an panel method was used that was allowed to change many of the geometrical parameters of the fuselage and other components, the smart use of penalty functions would be necessary to make sure that the geometry maintains a level of feasibility. This includes parameters such as length-to-beam ratio, which is currently user input. Care would need to be taken that it could not be made too large or too small, as either extreme is not feasible.

6.1.3 Control Surface Sizing

Proper control surface sizing is very important to having an aircraft that is capable of being trimmed. Initially in the sizing code, the chord and span factors of the ailerons, elevators, and rudders were determined from guidelines based on existing aircraft. When the aircraft was analyzed in AVL with control surfaces at the sizes suggested by these guidelines, the aircraft could not be trimmed. A parametric study was performed that looked at finding the control surface size that would result in the minimum deflection angle needed to trim

the aircraft. A flying wing aircraft normally gets rid of the use of a dedicated elevator and instead uses elevons to fill the rolls of both the elevator and ailerons. AVL results showed that the addition of a dedicated elevator as well as some slight resizing of the elevons and rudders would result in an aircraft that trimmed within acceptable limits of control surface deflection.

Presently, the sizing code treats the span and chord factors for the control surfaces as inputs and does not vary them or analyze their effectiveness. In order to properly size them during the preliminary design and optimization process, an analysis tool must be integrated with the code. One possible method would be to create a subroutine in the sizing code that writes an AVL input file then runs AVL for a worst-case scenario to determine if the control surfaces are of proper size. Since AVL can return the results in a text file format, the results could be read back into the sizing code and checked to see if the current size is acceptable.

Bibliography

[1] Knott, R. C., The *American Flying Boat: An Illustrated History,* Naval Press Institute, Annapolis, MD,1979.

[2] Jenkins, R. M., Hartfield, R. J., "Hybrid Particle Swarm – Pattern Search Optimizer for Aerospace Propulsion Applications," AIAA-2010-7078, 46th AIAA/ASME/SAE/ASEE Joint Propulsion Conference and Exhibit, Nashville, TN, July 2010.

[3] Raymer, D. P., *Aircraft Design: A Conceptual Approach,* 4th ed., Education Series, American Institute of Aeronautics and Astronautics, Inc., Reston, VA, 2006.

[4] Roskam, J., *Airplane Design: Part V: Component Weight Estimation*, Roskam Aviation and Engineering Corp., Ottawa, KS, 1985.

[5] Raymer, D.P., "Dynamic Lift Airship Design Study (Phase One)," Conceptual Research Corp., Rept. to Ohio Airships, Inc., Playa del Rey, CA, Dec. 2001.

[6] Corke, T. C., *Design of Aircraft,* Prentice Hall, Upper Saddle River, NJ, 2003.

[7] Garner, H. M., Coombes, L. P., "Seaplane Hulls and Floats: An Epitome of Present Knowledge with Suggestions for Future Research," *Aircraft Engineering and Aerospace Technology*, Vol. 2, No. 9, 1930, pp. 221-225.

[8] Nelson, W., *Seaplane Design,* 1st ed. McGraw-Hill Book Company, Inc., New York, NY, 1934.

[9] Klemin, A., Pierson, J.D., Storer, E. M., "An Introduction to Seaplane Porpoising," *Journal of the Aeronautical Sciences,* Vol. 6, No. 8, 1939, pp. 311-318.

[10] Benson, J. K., Lina, L. J., "The Use of a Retractable Planning Flap Instead of a Fixed Step on a Seaplane," NACA L-257, 1943.

[11] Carter, A. W., "Recent N.A.C.A. Research on High Length-Beam Ratio Hulls," *Journal of the Aeronautical Sciences*, Vol. 17, No. 3, 1949, pp. 167-183.

[12] Mottard, E. J., "A Brief Investigation of the Effect of Waves on the Take-Off Resistance of a Seaplane," NASA TN-D-165, 1959.

[13] Long, B. J., "The Navy Seadart Supersonic Seaplane," AIAA 1993-3941, Aircraft Design @Systems and Operations Meeting, Monterey, CA, Aug. 1993.

[14] Fisher, L. J., Hoffman, E. L., "A Brief Hydrodynamic Investigation of a Navy Seaplane Design Equipped with a Hydro-Ski," NACA RM-L53F04, 1953.

[15] "The Hydrofoil and Float Combination," Seaplane Pilots Association, Aug. 2008, http://www.seaplanes.org/mambo/index.php?option=com_content&task=view&id=221&Itemid=245 [retrieved 20 June 2011].

[16] McKann, R. E., Blanchard, U. J., Pearson, A. O., "Hydrodynamic and Aerodynamic Characteristics of A Model of A Supersonic Multijet Water-Based Aircraft Equipped with Supercavitating Hydrofoils," NASA TM-X-191, 1960.

[17] Vagianos, N. J., Thurston, D. B., "Hydrofoil Seaplane Design," Thurston Aircraft Corp., Rept. to Department of the Navy Air Systems Command, Sanford, ME, 1970.

[18] Petrie, D. M., "Operational and Developmental Experience on the U.S. Navy Hydrofoil 'High Point'," *Journal of Aircraft*, Vol. 3, No. 1, 1966, pp. 79-84.

[19] Holland, J. H., *Adaptation in Natural and Artificial Systems: An Introductory Analysis with Applications to Biology, Control and Artificial Intelligence*, The MIT Press, Cambridge, MA, 1975.

[20] Obayashi, S., Yamaguchi, Y., Nakamura, T., "Multiobjective Genetic Algorithm for Multidisciplinary Design of a Transonic Wing Planform," *Journal of Aircraft*, Vol. 34, No. 5, 1997, pp. 690-693.

[21] Vicini, A., Quagliarella, D., "Inverse and Direct Airfoil Design Using a Multiobjective Genetic Algorithm," *AIAA Journal*, Vol. 35, No. 9, 1997, pp. 1499-1505.

[22] Crossley, W. A., Laananen, D. H., "Conceptual Design of Helicopters via Genetic Algorithm," *Journal of Aircraft*, Vol. 33, No. 6, 1996, pp. 1062-1070.

[23] Kennedy, J., Eberhard, R., "A New Optimizer using Particle Swarm Theory," 6th International Symposium on Micro Machine and Human Sciences, Nagoya, Japan, Oct. 1995.

[24] Mishra, S. K., "Repulsive Particle Swarm Method on Some Difficult Test Problems of Global Optimization," Sept. 2006, http://ssrn.com/abstract=928538 [retrieved 25 June 2011].

[25] Hooke, R., Jeeves, T. A., "'Direct Search' Solution of Numerical and Statistical Problems," *Journal of the ACM*, Vol. 8, No. 2, 1961, pp. 212-229.

[26] Hasdorff, L., *Gradient Optimization and Nonlinear Control*, John Wiley & Sons, Inc., New York, NY, 1976.

[27] Anderson, J. D, *Fundamentals of Aerodynamics*, 4th ed., McGraw-Hill Higher Education, Boston, MA, 2007.

[28] Jacobs, E. N., "The Variable Density Tunnel," NACA-TR-416, 1932.

[29] Barlow, J. B., Rae, W. H., Pope, A., *Low-Speed Wind Tunnel Testing*, 3rd ed., John Wiley & Sons, Inc., New York, NY, 1999.

[30] Braslow, A. L., Hicks, R. M., Harris, R. V., "Use of Grit Type Boundary Layer Transition Trips on Wind Tunnel Models," NASA TN-D-3579, 1966.

[31] Holmes, B. J., Obara, C. J., "Observations and Implications of Natural Laminar Flow on Practical Airplane Surface," ICAS-82-5.1.1, *Proceedings of the 13th Congress of International Council of Aeronautical Sciences*, Vol. 1, AIAA, New York, NY, 1982, pp. 168-181.

[32] Thom, A., "Blockage Corrections in a High Speed Wind Tunnel," ARC R&M 2033, 1943.

[33] Smits, A. J., Lim, T. T., *Flow Visualization Techniques and Examples*, Imperial College Press, London, England, 2000.

[34] Merzkirch, W., *Flow Visualization*, 2nd ed., Academic Press, Inc., Orlando, FL, 1987.

[35] Shoemaker, J. M., Parkinson, J. B., "A Complete Tank Test of a Model of a Flying-Boat Hull – N.A.C.A. Model No. 11," NACA TN-464, 1933.

[36] Langley, M., *Seaplane Float and Hull Design*, Sir Isaac Pitman & Sons, Ltd., London, England, 1935.

[37] "Main Float Buoyancy," FAR 23.751, Federal Aviation Administration, 2011.

[38] Gilruth, R. R., White, M. D., "Analysis and Prediction of Longitudinal Stability of Airplanes," NACA-TR-711, 1941.

[39] Pamadi, B. N., *Performance, Stability, Dynamics and Control of Airplanes*, 2nd ed., Education Series, American Institute of Aeronautics and Astronautics, Inc., Reston, VA, 2004.

[40] "C-130 Hercules Factsheet," United States Air Force, Oct. 2009, http://www.af.mil/ information/factsheets/factsheet.asp?fsID=92 [retrieved 30 March 2011].

[41] *172R (180HP) Skyhawk Information Manual*, The Cessna Aircraft Company, Wichita, KS, 1999.

[42] "The BF2550 Float," Baumann Floats, Feb. 2008, http://baumannfloats.com/models/ pdf/bf2550.pdf [retrieved 28 March 2011].

[43] Lagarias, J. C., Reeds, J.A., Wright, M. H., Wright, P. E., "Convergence Properties of the Nelder-Mead Simplex Method in Low Dimensions," *SIAM Journal on Optimization*, Vol. 9, No. 1, 1998, pp.112-147.

[44] Albarado, K.M., Hartfield, R.J., Jenkins, R.M., Hurston, B.W., "Solid Rocket Motor Performance Matching Using Pattern Search/Particle Swarm Optimization", AIAA-2011-5798, 47th AIAA/ASME/SAE/ASEE Joint Propulsion Conference, San Diego, CA, July 2011.

[45] Brimm, D. J., *Seaplanes: Maneuvering, Maintaining, Operating*, Pitman Publishing Corporation, New York, NY, 1937.

[46] Sederberg, M. T., Sederberg, T. W., "T-Splines: A Technology for Marine Design with Minimal Control Points", Chesapeake Powerboat Symposium, Annapolis, MD, March 2010.

[47] Bertin Jr., J. J., Smith, M. L., *Aerodynamics for Engineers*, 1st ed., Prentice-Hall, Inc., New Jersey, 1979.

[48] Roskam, J., *Airplane Design: Part VII: Determination of Stability, Control and Performance Characteristics: FAR and Military Requirements*, Roskam Aviation and Engineering Corp., Ottawa, KS, 1985.

[49] "Military Specification: Flying Qualities of Piloted Airplanes," MIL-F-8785C, Department of Defense, 1980.

[50] Ahuja, V., Burkhalter, J., Hartfield, R. J., "Preliminary Design Drag Calculations Using Advanced Paneling Schemes," AIAA-2010-0063, 48th AIAA Aerospace Sciences Meeting, Orlando, FL, Jan. 2010.

Appendix A: Sizing Code Text Output Sample

```
CONVERGENCE TEST
Weight Estimate                    117169 lbs
Excess Weight                           0 lbs

FLIGHT PLAN
Time Airborne                       11.13 hrs

AIRCRAFT SPECIFICATIONS
Main Wing
   Planform Area                  3090.39 ft^2
   W/S                              37.91 lb/ft^2
   Total Span                      179.82 ft
   Inner Wing Segment Half-Span      4.83 ft
   Root Chord                       23.57 ft
   Aspect Ratio                     10.46
   e                                 0.76
   Mean Aerodynamic Chord           17.56 ft
   Inboard Taper Ratio               0.89
   Outboard Taper Ratio              0.62
   Inboard Sweep Angle (LE)         17.65 deg
   Outboard Sweep Angle (LE)         4.95 deg
   Inboard Sweep Angle (TE)        -13.48 deg
   Outboard Sweep Angle (TE)        -0.39 deg
   Location of c/4 Behind Nose      15.53 ft
Horizontal Tail
   Planform Area                   994.76 ft^2
   Span                             73.13 ft
   Root Chord                       20.73 ft
   Aspect Ratio                      5.38
   Taper Ratio                       0.31
   Sweep Angle (LE)                 13.00 deg
```

Location of c/4 Behind Nose	62.17	ft
Vertical Tail		
Planform Area	647.67	ft^2
Span	36.81	ft
Root Chord	27.36	ft
Aspect Ratio	2.09	
Taper Ratio	0.29	
Sweep Angle (LE)	27.96	deg
Location of c/4 Behind Nose	57.20	ft

BUOYANCY CHARACTERISTICS		
Total Displacement	2349.43	ft^3
Wing	109.01	ft^3
Fuselage	228.16	ft^3
Cabin	1785.00	ft^3
Tail	51.16	ft^3
Floats	82.38	ft^3
Systems	43.70	ft^3
Batteries	0.00	ft^3
Fuel (Submerged)	50.01	ft^3

FLIGHT CHARACTERISTICS		
L/D Cruise	20.2594	
L/D Ground Effect	21.0098	
Speed Cruise	184.12	kts
Speed Ground Effect	167.66	kts
Cruise Thrust (Sea Level)	10850.21	lbs

FUSELAGE DIMENSIONS		
Fuselage Width	9.67	ft
Fuselage Height	9.67	ft
Fuselage Length	77.72	ft

WEIGHT BREAKDOWN

Gross Weight	117169.01 lb	22.08 ft
Empty Weight	73600.04 lb	
Fuel Weight	24818.97 lb	22.08 ft
Payload	18750.00 lb	19.50 ft
Cargo Weight	18750.00 lb	
Pilot Weight	0.00 lb	

Component Weight Breakdown

Wing	18223 lb	20.95 ft
HT	3112 lb	65.55 ft
VT	1403 lb	62.75 ft
Fuselage	15422 lb	17.10 ft
Cabin	6212 lb	19.50 ft
Main LG	0 lb	20.95 ft
Nose LG	0 lb	15.54 ft
Nacelle Group	1958 lb	20.95 ft
Engine	1938 lb	20.95 ft
Engine Controls	51 lb	20.95 ft
Starter	70 lb	20.95 ft
Fuel System	173 lb	20.95 ft
Flight Controls	1431 lb	20.95 ft
Instruments	548 lb	19.50 ft
Hydraulics	340 lb	31.09 ft
Electrical	532 lb	19.50 ft
Avionics	5392 lb	19.50 ft
Furnishings	1097 lb	19.50 ft
A/C	957 lb	19.50 ft
Anti-Ice	234 lb	20.95 ft
Handling Gear	35 lb	19.50 ft
Cargo Handling Sys	467 lb	19.50 ft
Struts	3515 lb	20.95 ft
Floats	10489 lb	22.08 ft

CENTER OF GRAVITY CALCULATIONS

C.G. Location (From Nose)	22.08	ft
C.G. Percent of Fuselage	28.41	%

NEUTRAL POINT CALCULATIONS

N.P. Location (From Nose)	23.52	ft
N.P. Percent of Fuselage	30.26	%
Static Margin	8.20	%

Component Drag Breakdown

	Cruise	In GE	
Wing	0.00755	0.00702	
Fuselage	0.00163	0.00151	
H Tail	0.00305	0.00284	
V Tail	0.00188	0.00175	
Nacelle	0.00020	0.00019	
Floats	0.00225	0.00209	
Struts	0.00042	0.00040	
Misc	-0.00170	-0.00158	
TOTAL Cd0	0.01529	0.01422	
Drag Area	47.27	43.95	ft^2

Reynolds Numbers

	Cruise	In GE
Wing	21574637	31037475
Fuselage	95480151	137358636
H Tail	6944615	9990588
V Tail	9042993	13009334
Nacelle	11706502	16841083
Floats	70309984	101148598
Struts	1228494	1767322

Friction Coefficients

	Cruise	In GE

Wing	0.00253	0.00235
Fuselage	0.00188	0.00174
H Tail	0.00317	0.00295
V Tail	0.00301	0.00279
Nacelle	0.00285	0.00265
Floats	0.00199	0.00185
Struts	0.00448	0.00417

Flight Parameters

	Cruise	In GE	
Speed	184.12	167.66	kts
Mach Number	0.30	0.25	
Dyn Pressure	61.18	95.17	lbs/ft^2
Cl	0.620	0.398	
Cd	0.0306	0.0205	
Cdi	0.0153	0.0047	
L/D	20.26	21.01	

Appendix B: Final Optimized Design Sizing Code Output

```
CONVERGENCE TEST
Weight Estimate                      93900 lbs
Excess Weight                            0 lbs

SUBMERGED PROPULSION TYPE
Battery Powered When Submerged.

FLIGHT PLAN
Time Enroute to Dropoff              12.14 hrs
   Time Airborne                     12.14 hrs
   Conversion Time                    0.00 hrs
   Time Submerged                     0.00 hrs

AIRCRAFT SPECIFICATIONS
Main Wing
   Planform Area                  3838.83 ft^2
   W/S                              24.46 lb/ft^2
   Total Span                      147.07 ft
   Inner Wing Segment Half-Span     10.18 ft
   Root Chord                       57.45 ft
   Aspect Ratio                      5.63
   e                                 0.83
   Mean Aerodynamic Chord           34.32 ft
   Inboard Taper Ratio               0.74
   Outboard Taper Ratio              0.10
   Inboard Sweep Angle (LE)         56.75 deg
   Outboard Sweep Angle (LE)        23.94 deg
   Inboard Sweep Angle (TE)          4.92 deg
   Outboard Sweep Angle (TE)        -9.32 deg
   Location of c/4 Behind Nose      14.36 ft
Vertical Tail
```

Number of Vertical Tails	2	
Planform Area Per Tail	455.54	ft^2
Span	30.41	ft
Root Chord	19.97	ft
Aspect Ratio	1.40	
Taper Ratio	0.50	
Sweep Angle (LE)	23.70	deg
Location of c/4 Behind Nose	47.30	ft

BUOYANCY CHARACTERISTICS

Total Displacement	2519.89	ft^3
Wing	205.67	ft^3
Fuselage	414.84	ft^3
Cabin	1785.00	ft^3
Tail	28.01	ft^3
Floats	0.00	ft^3
Systems	43.70	ft^3
Batteries	0.00	ft^3
Fuel (Submerged)	42.67	ft^3
Downforce Required	86989.40	ft^3
Dry Volume for Neutral Buoyancy	732.30	ft^3

FLIGHT CHARACTERISTICS

L/D Cruise	18.5401	
L/D Ground Effect	19.2081	
L/D Submerged	17.2394	
Speed Cruise	166.14	kts
Speed Ground Effect	151.21	kts
Speed Submerged	3.89	kts
Cruise Thrust (Sea Level)	9501.85	lbs
Power Submerged	60.29	HP

FUSELAGE DIMENSIONS

Fuselage Width	15.16 ft	
Fuselage Height	15.16 ft	
Fuselage Length	57.45 ft	
WEIGHT BREAKDOWN		
Gross Weight	93900.30 lb	26.82 ft
Empty Weight	54253.13 lb	
Fuel Weight	20897.17 lb	33.79 ft
Payload	18750.00 lb	19.50 ft
Cargo Weight	18750.00 lb	
Pilot Weight	0.00 lb	
Underwater Equipment	0.00 lb	
Submerged Prop. Batt. Weight	0.00 lb	17.63 ft
Submerged Prop. Motor Weight	0.00 lb	34.47 ft
Component Weight Breakdown		
Wing	14116 lb	29.02 ft
HT	0 lb	51.70 ft
VT	1199 lb	51.51 ft
Fuselage	15582 lb	28.72 ft
Cabin	6212 lb	19.50 ft
Main LG	1005 lb	29.02 ft
Nose LG	579 lb	11.49 ft
Nacelle Group	1706 lb	29.02 ft
Engine	1675 lb	29.02 ft
Engine Controls	43 lb	29.02 ft
Starter	65 lb	29.02 ft
Fuel System	156 lb	33.79 ft
Flight Controls	1288 lb	29.02 ft
Instruments	489 lb	19.50 ft
Hydraulics	274 lb	45.96 ft
Electrical	479 lb	19.50 ft
Avionics	5392 lb	19.50 ft
Furnishings	1225 lb	19.50 ft

A/C	830 lb	19.50 ft
Anti-Ice	188 lb	29.02 ft
Handling Gear	28 lb	19.50 ft
Cargo Handling Sys	292 lb	19.50 ft
Sponsons	1429 lb	26.82 ft

CENTER OF GRAVITY CALCULATIONS

C.G. Location (From Nose)	26.82 ft
C.G. Percent of Fuselage	46.68 %

NEUTRAL POINT CALCULATIONS

N.P. Location (From Nose)	31.13 ft
N.P. Percent of Fuselage	54.18 %
Static Margin	12.56 %

Component Drag Breakdown

	Cruise	In GE
Wing	0.00673	0.00627
Fuselage	0.00459	0.00427
H Tail	0.00000	0.00000
V Tail	0.00185	0.00173
Nacelle	0.00015	0.00014
Sponsons	0.00140	0.00130
Misc	-0.00147	-0.00137
TOTAL Cd0	0.01324	0.01234
Drag Area	50.84	47.36

Reynolds Numbers

	Cruise	In GE
Wing	38414066	54730444
Fuselage	64301475	91613533
H Tail	0	0
V Tail	18233917	25978775
Nacelle	9935922	14156206

Sponsons	23776693	33875846

Friction Coefficients

	Cruise	In GE
Wing	0.00225	0.00210
Fuselage	0.00203	0.00189
H Tail	0.00000	0.00000
V Tail	0.00261	0.00243
Nacelle	0.00295	0.00275
Sponsons	0.00248	0.00231

Flight Parameters

	Cruise	In GE	
Speed	166.14	151.21	kts
Mach Number	0.27	0.23	
Dyn Pressure	49.81	77.41	lbs/ft^2
Cl	0.491	0.316	
Cd	0.0265	0.0178	
Cdi	0.0132	0.0041	
L/D	18.54	19.21	

Appendix C: Cessna 172 Wind Tunnel Data and Results

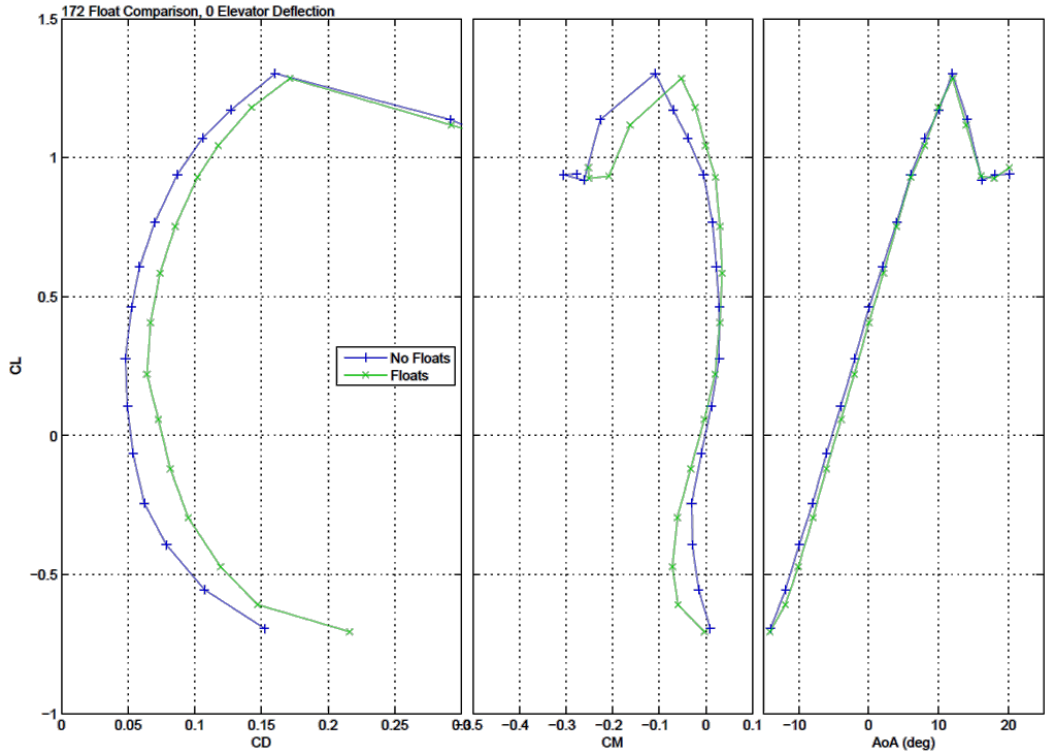

Figure 56: Cessna 172 Float Comparison, 0 Elevator Deflection

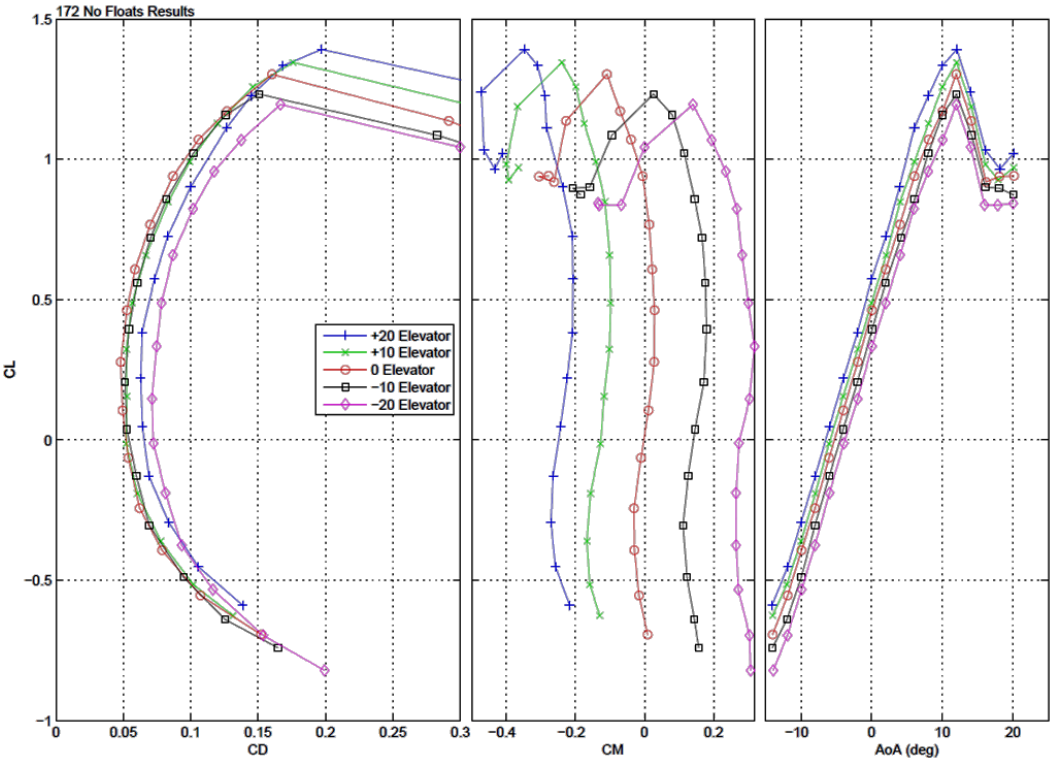

Figure 57: 172 No Floats Results

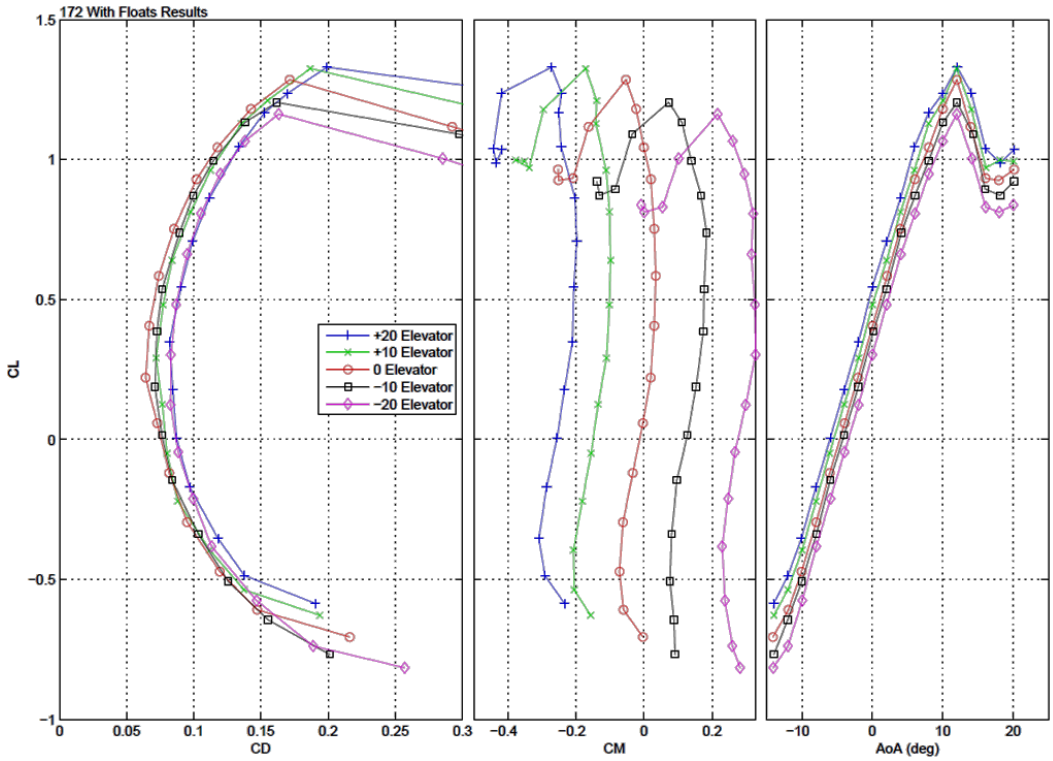

Figure 58: 172 with Floats Results

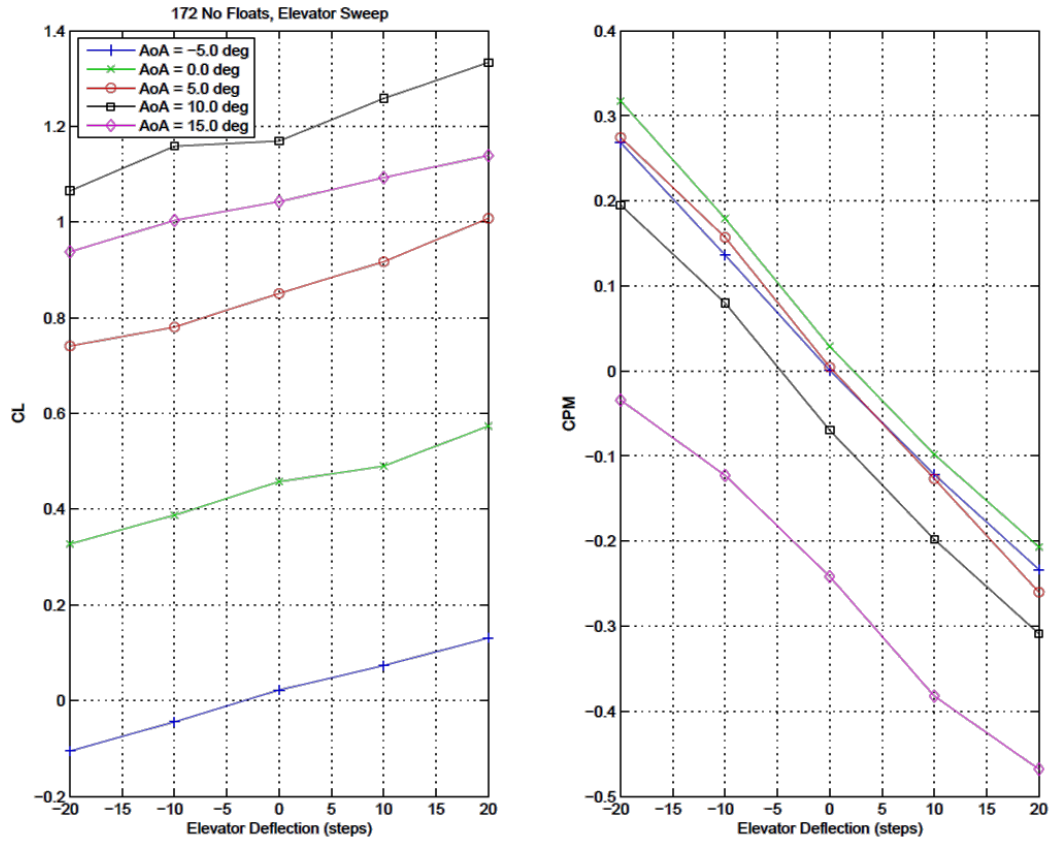

Figure 59: 172 No Floats, Elevator Sweep

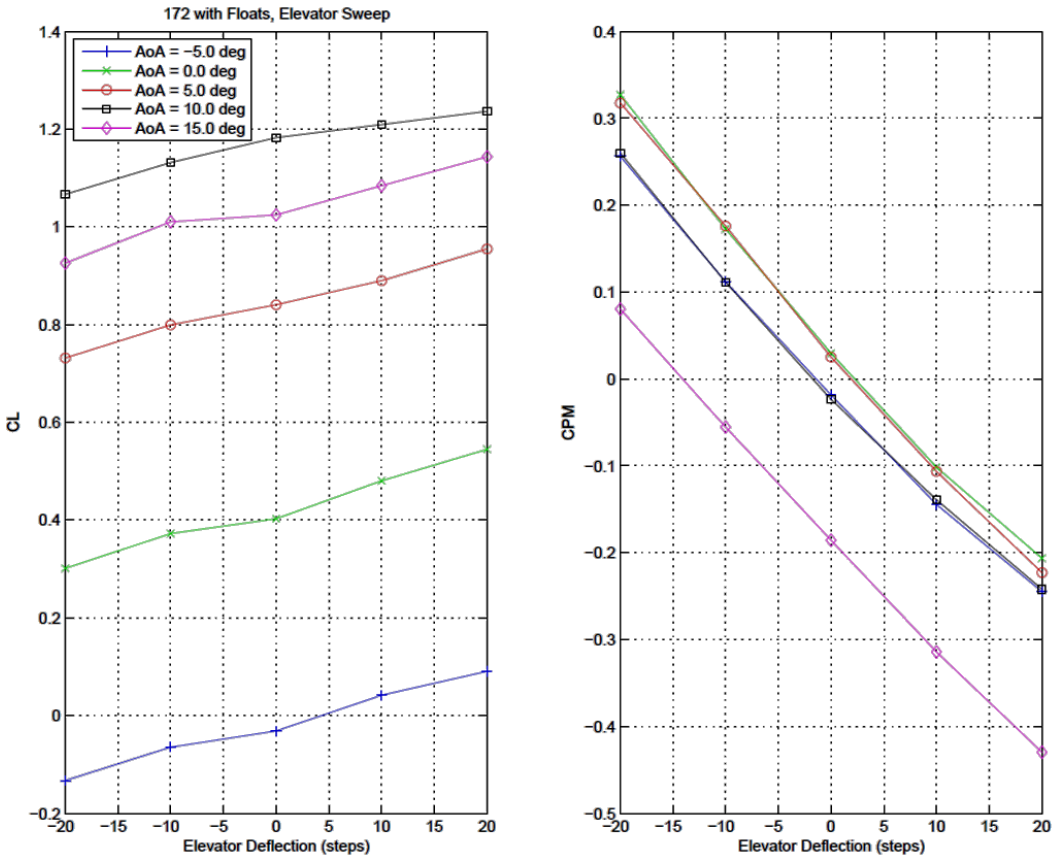

Figure 60: 172 with Floats, Elevator Sweep

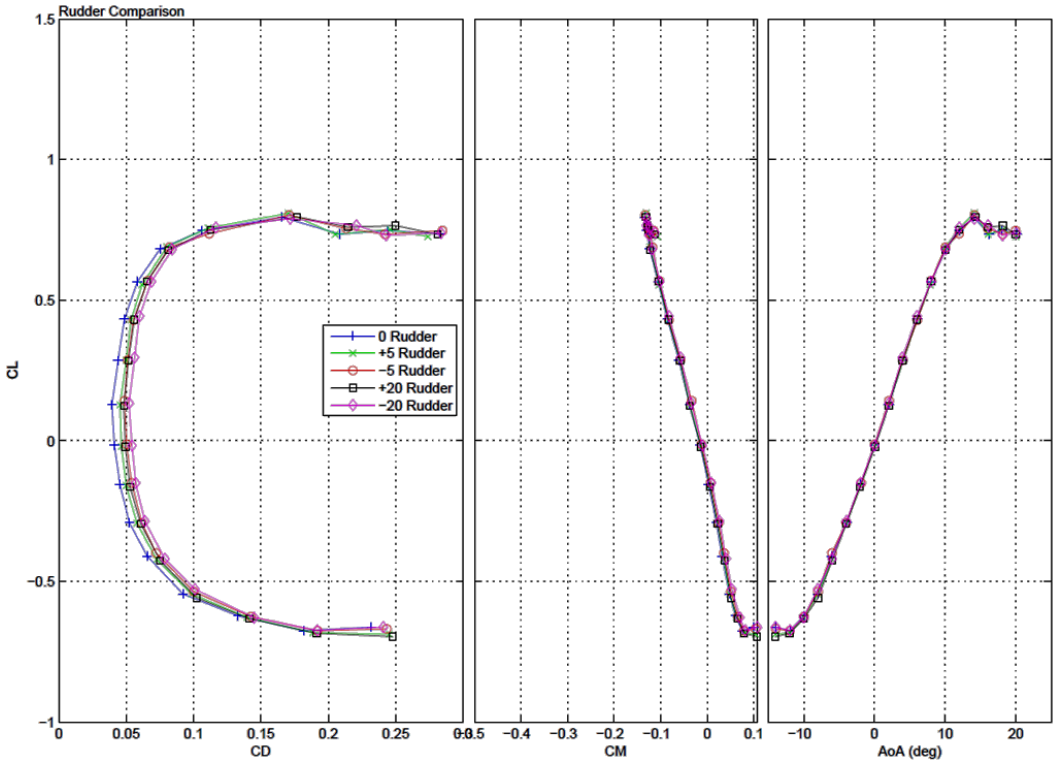

Figure 61: 0 Yaw, Rudder Comparison

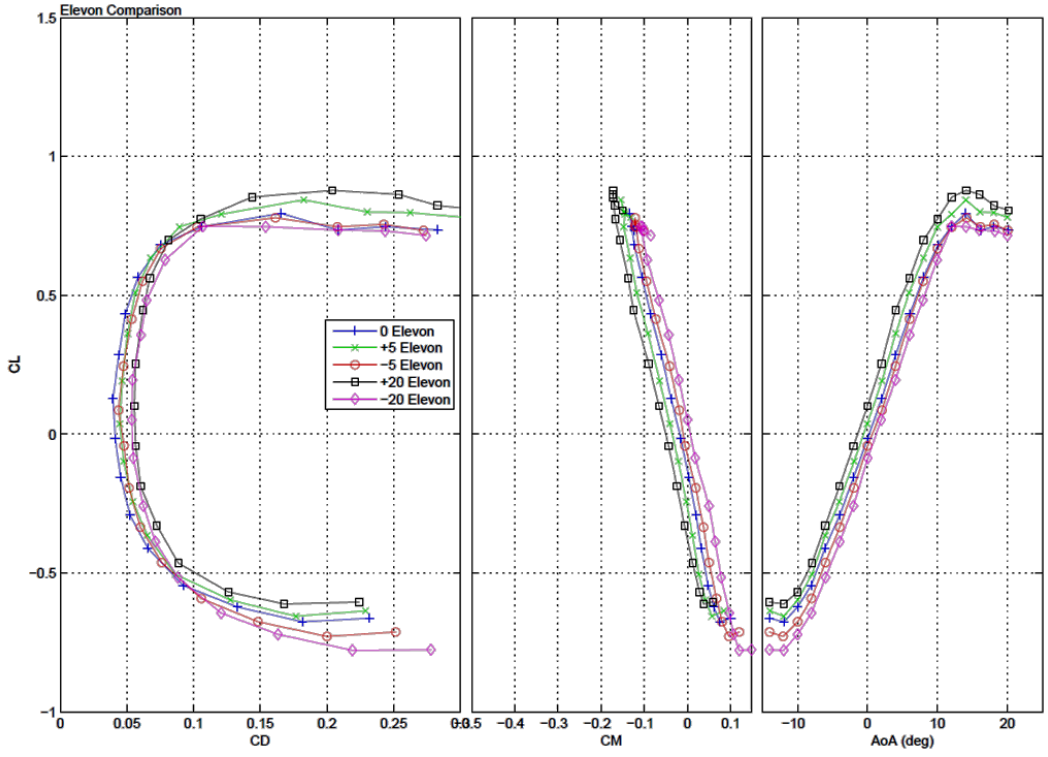

Figure 62: 0 Yaw, Elevon Comparison

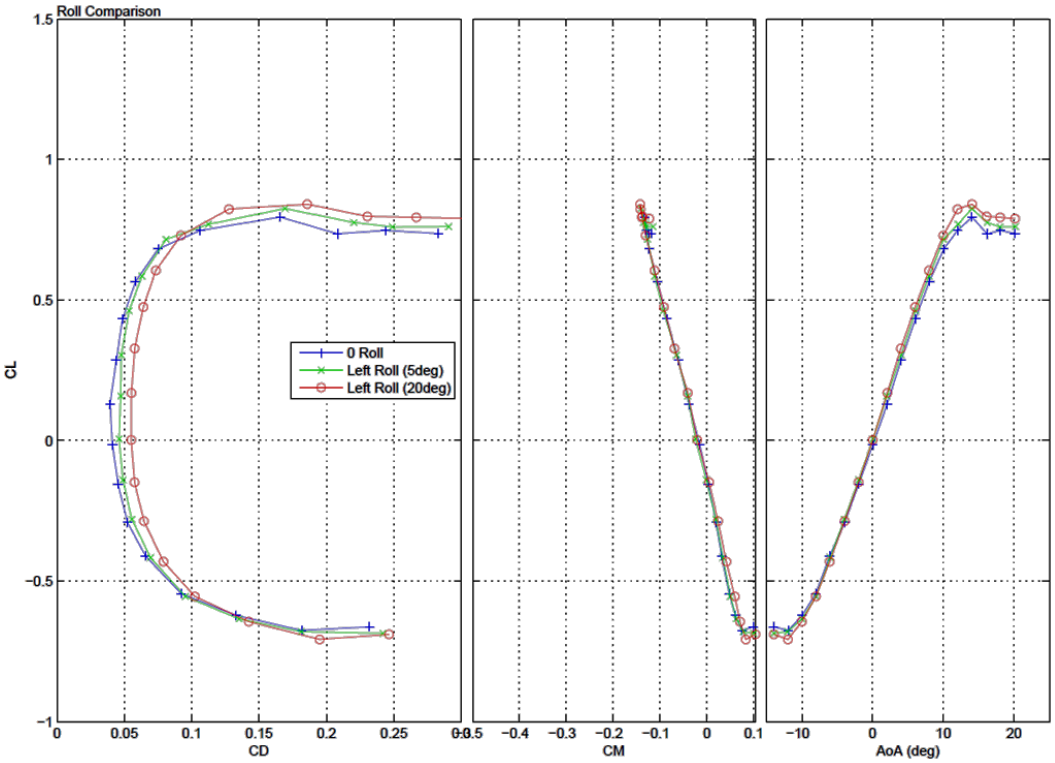

Figure 63: 0 Yaw, Roll Comparison

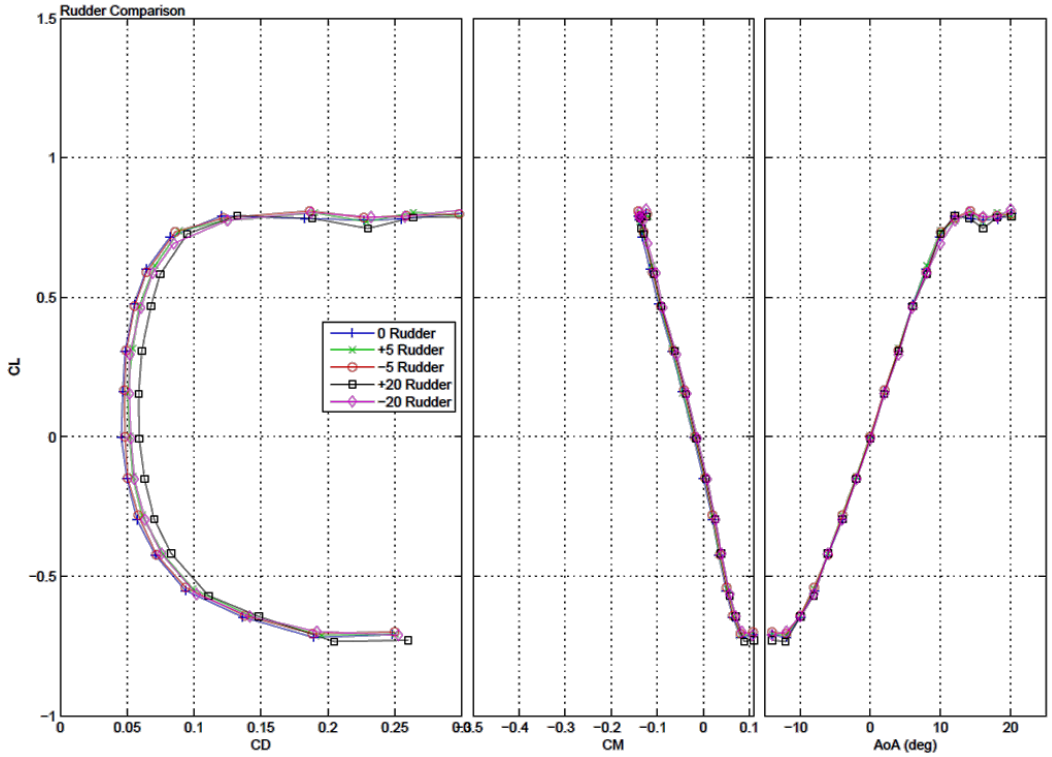

Figure 64: -5 Yaw, Rudder Comparison

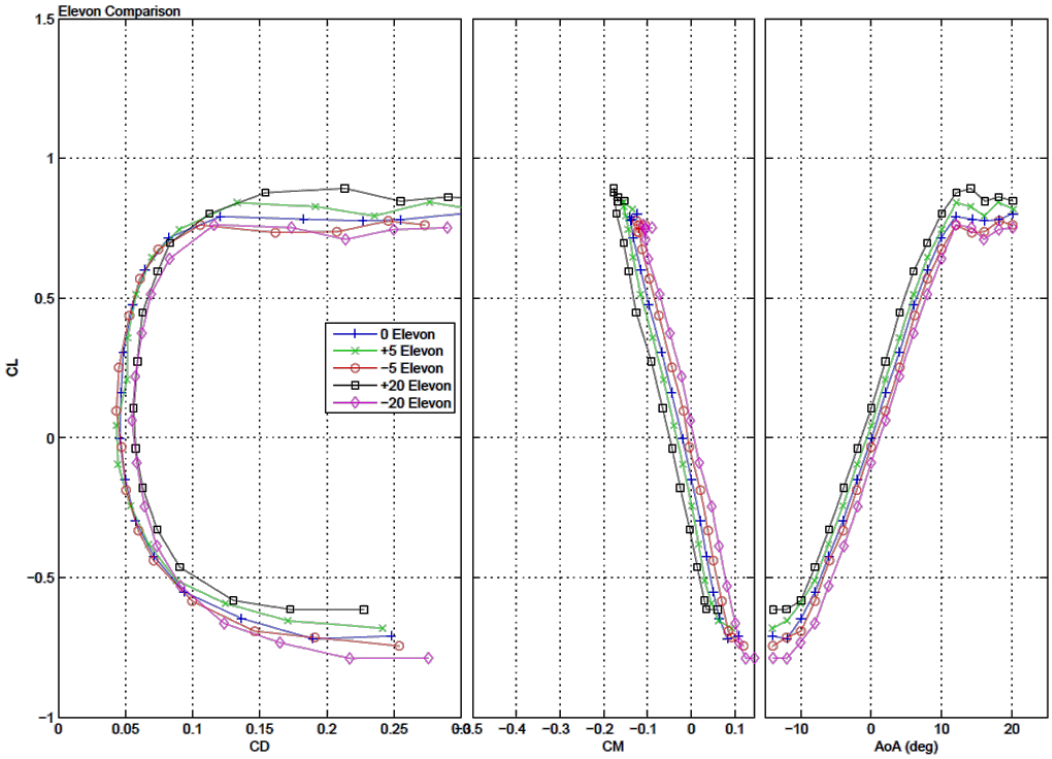

Figure 65: -5 Yaw, Elevon Comparison

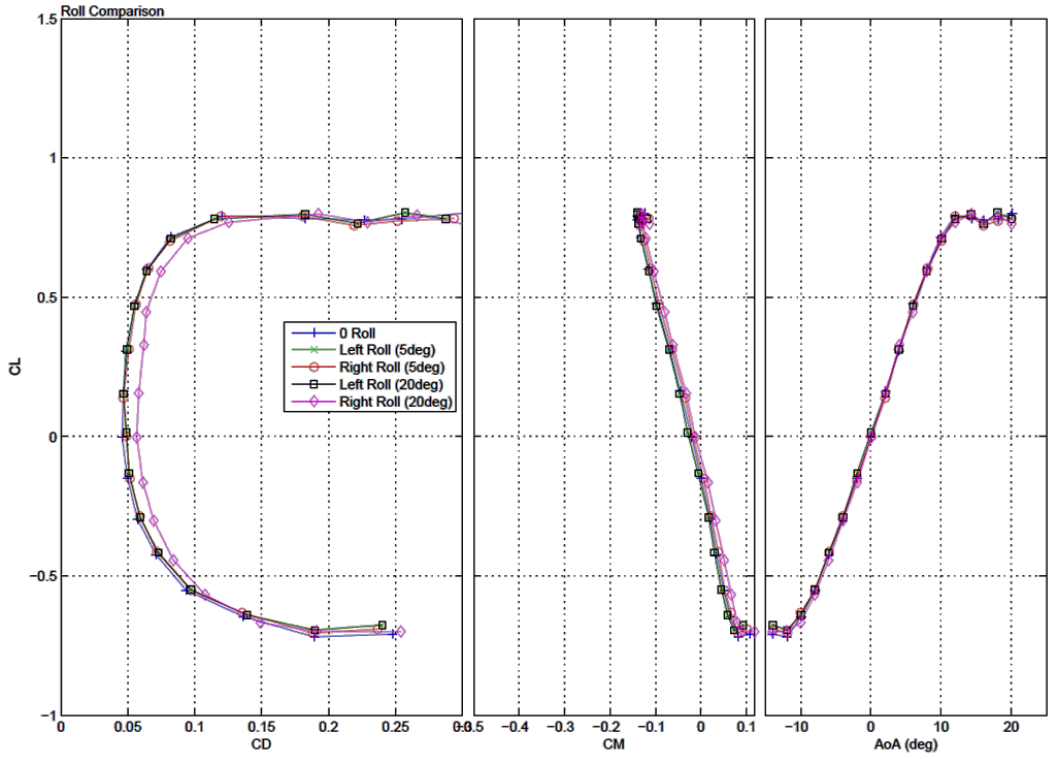

Figure 66: -5 Yaw, Roll Comparison

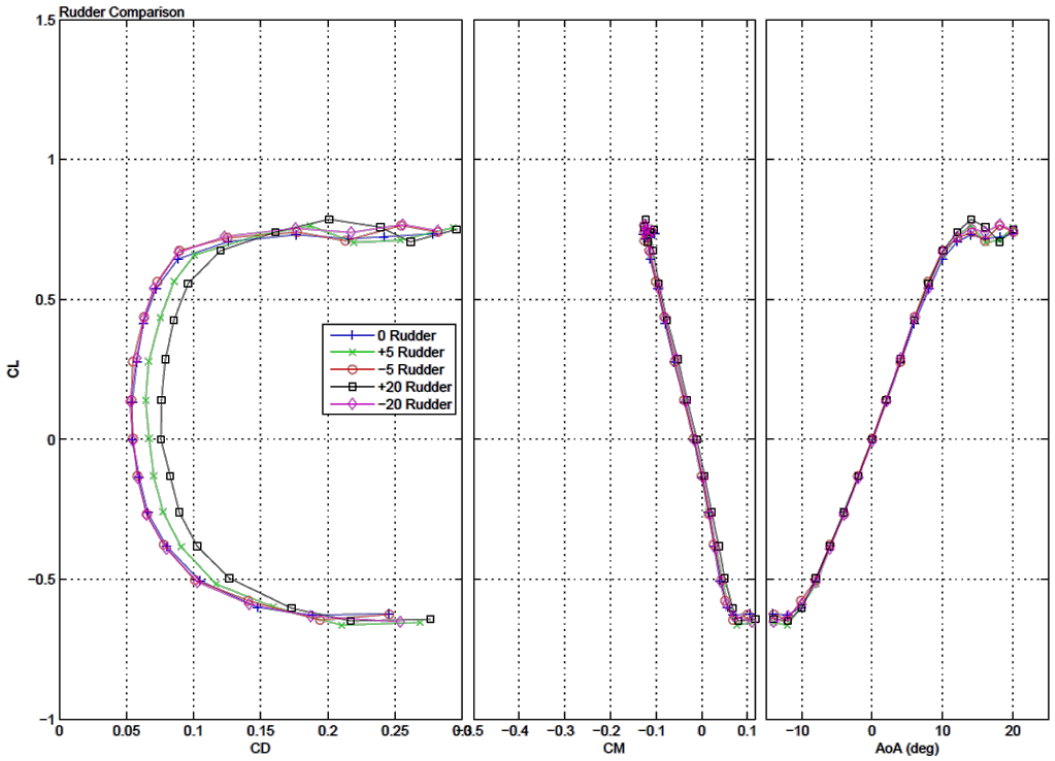

Figure 67: -11.5 Yaw, Rudder Comparison

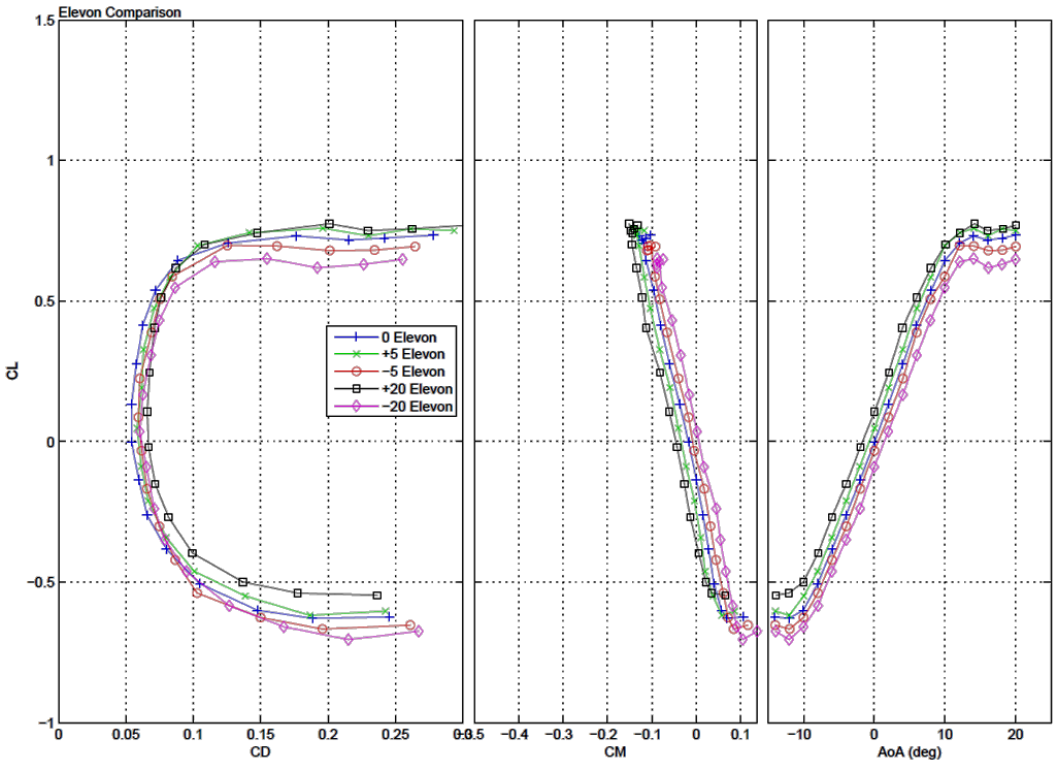

Figure 68: -11.5 Yaw, Elevon Comparison

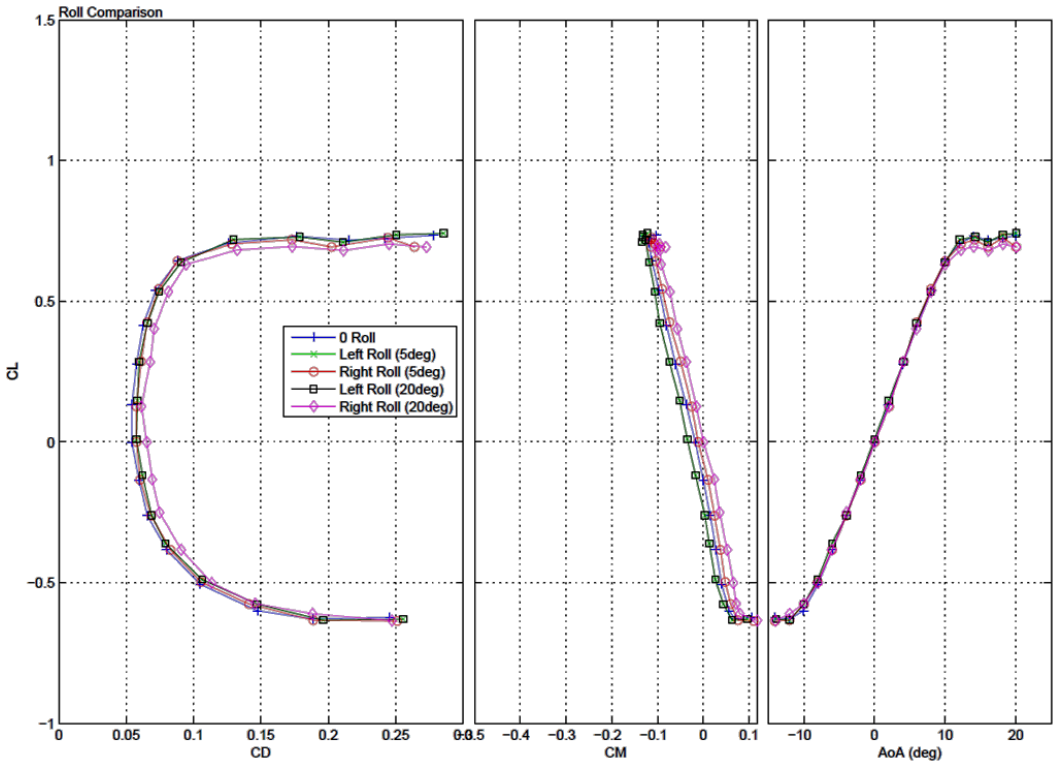

Figure 69: -11.5 Yaw, Roll Comparison

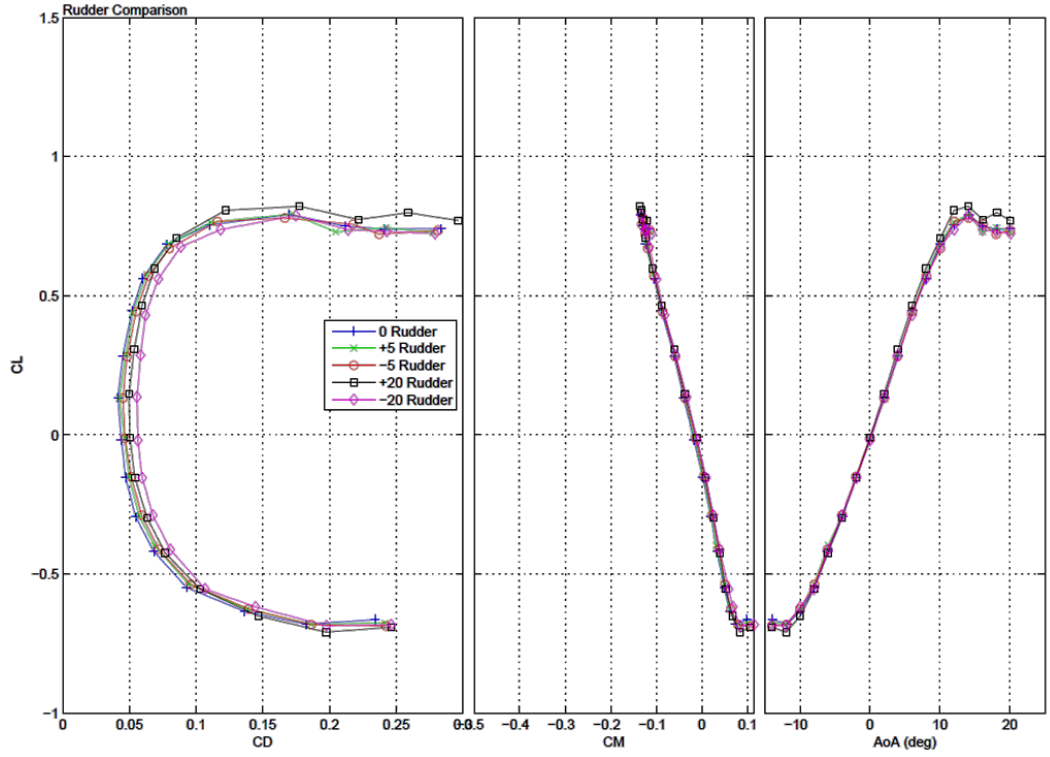

Figure 70: +5 Yaw, Rudder Comparison

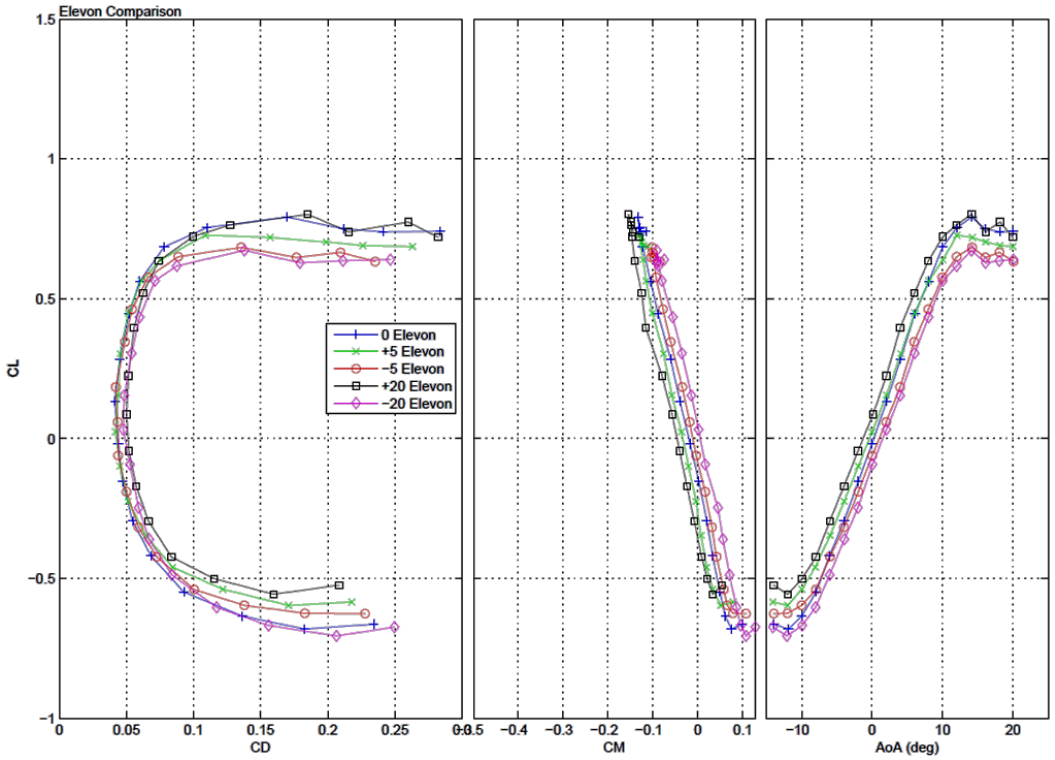

Figure 71: +5 Yaw, Elevon Comparison

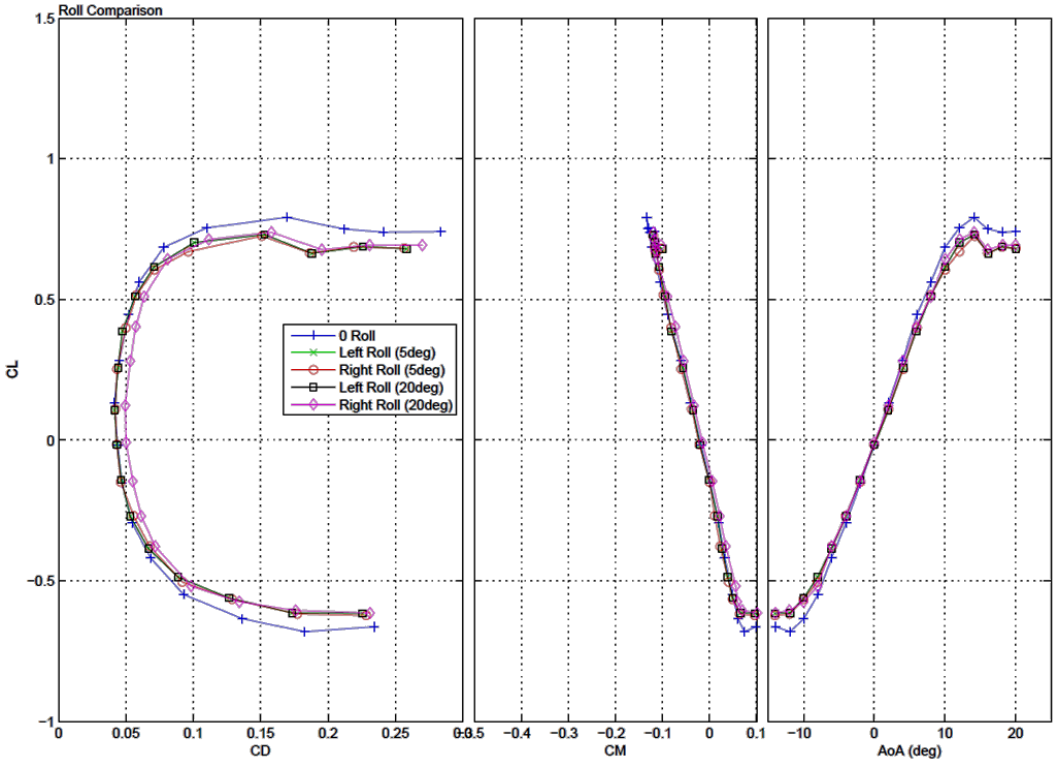

Figure 72: +5 Yaw, Roll Comparison

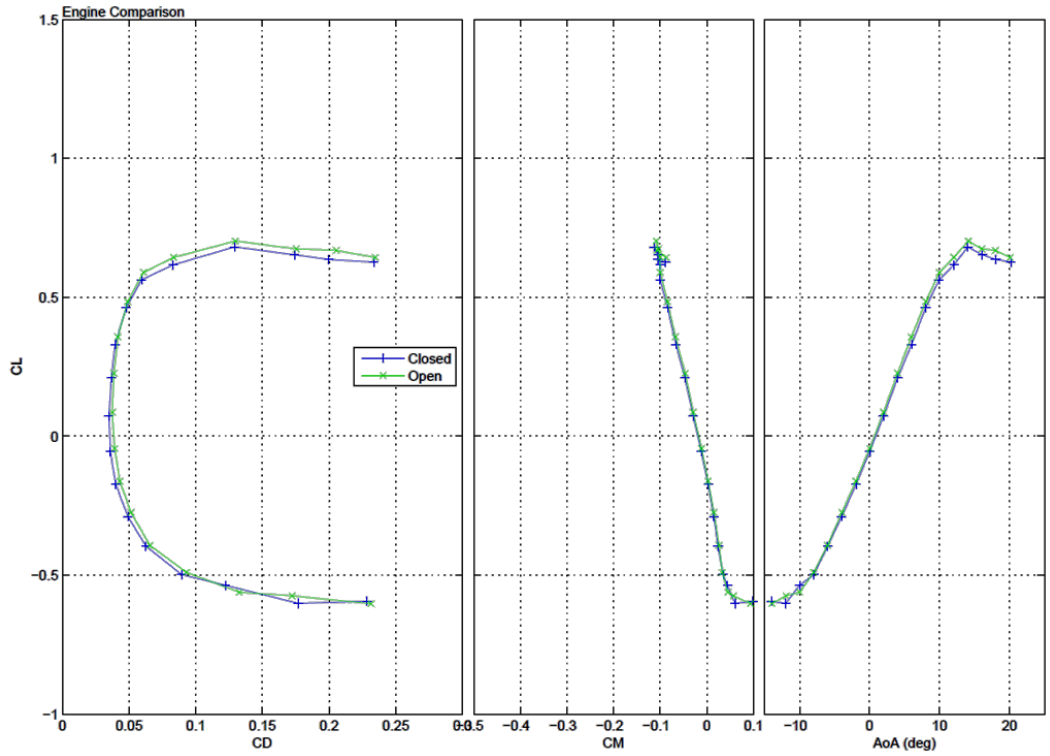

Figure 73: Engine Comparison

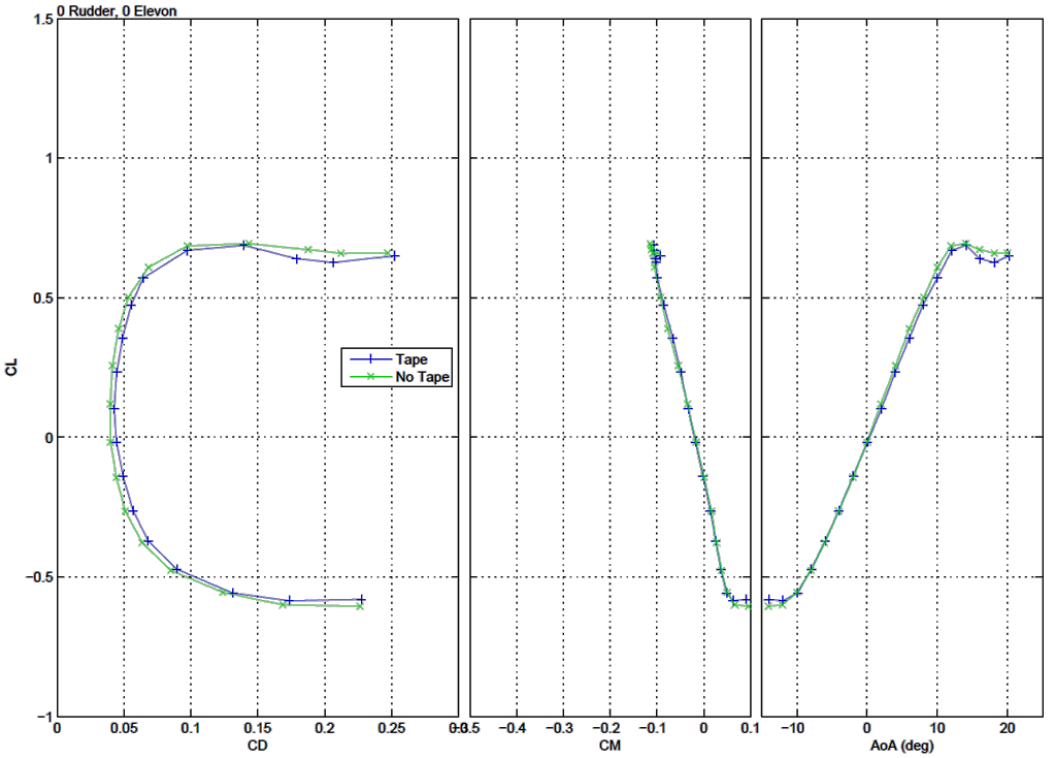

Figure 74: 0 Rudder, 0 Elevon, Transition Strip Comparison

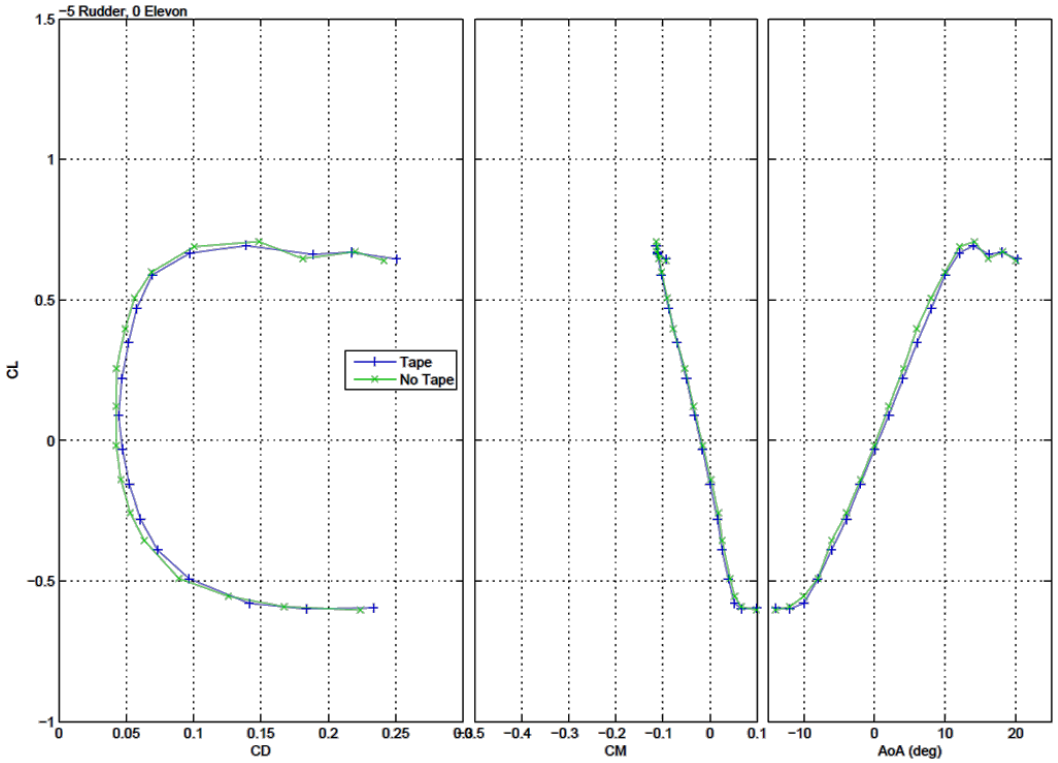

Figure 75: -5 Rudder, 0 Elevon, Transition Strip Comparison

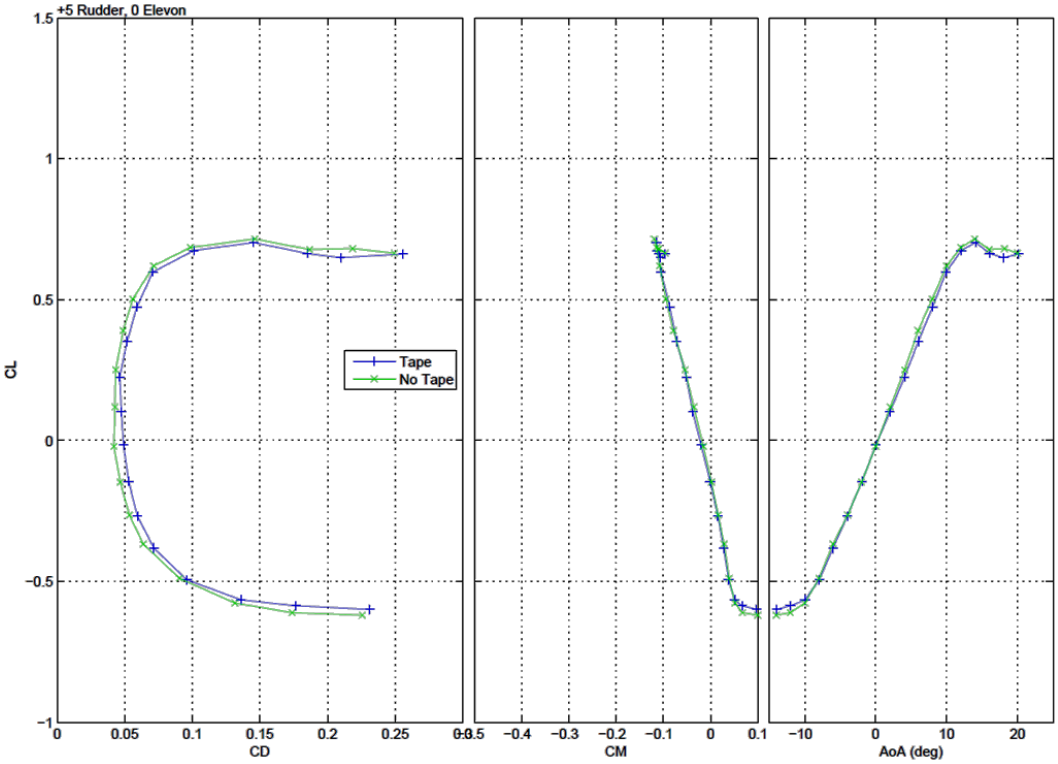

Figure 76: +5 Rudder, 0 Elevon, Transition Strip Comparison

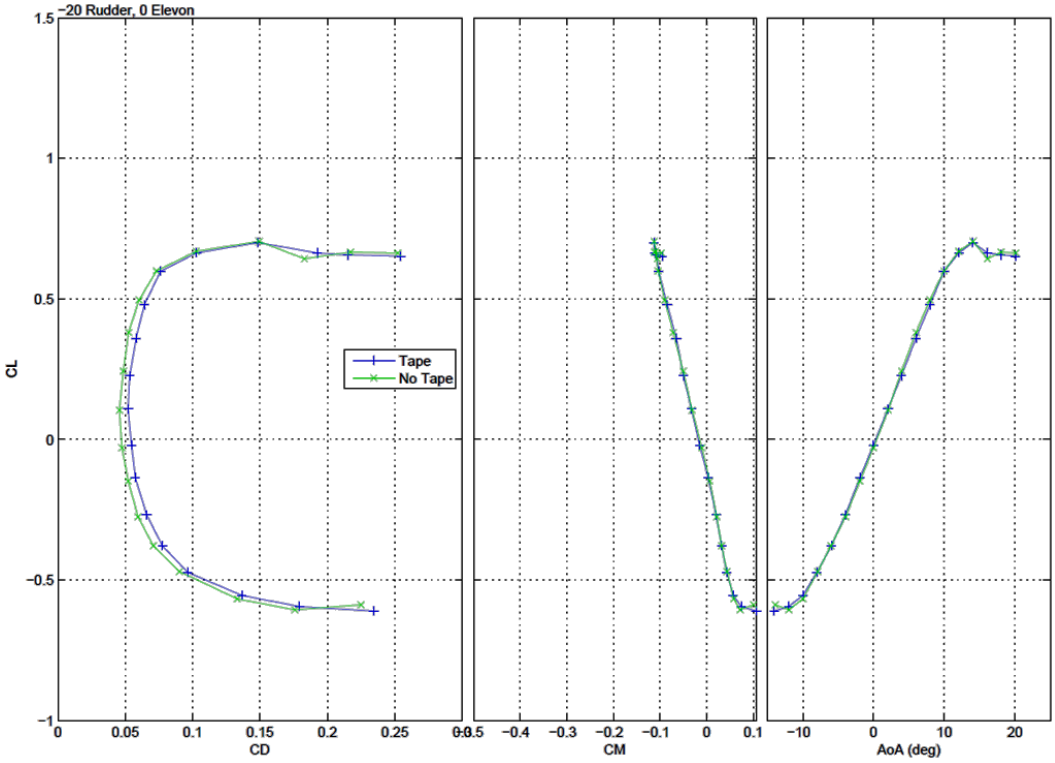

Figure 77: -20 Rudder, 0 Elevon, Transition Strip Comparison

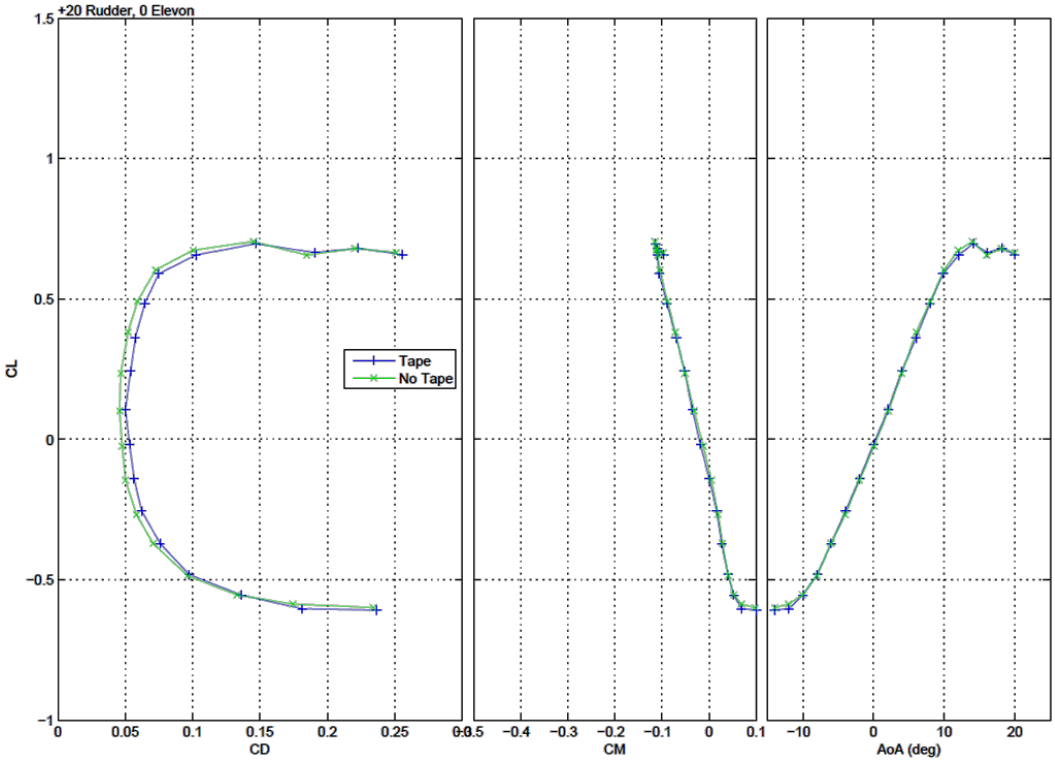

Figure 78: +20 Rudder, 0 Elevon, Transition Strip Comparison

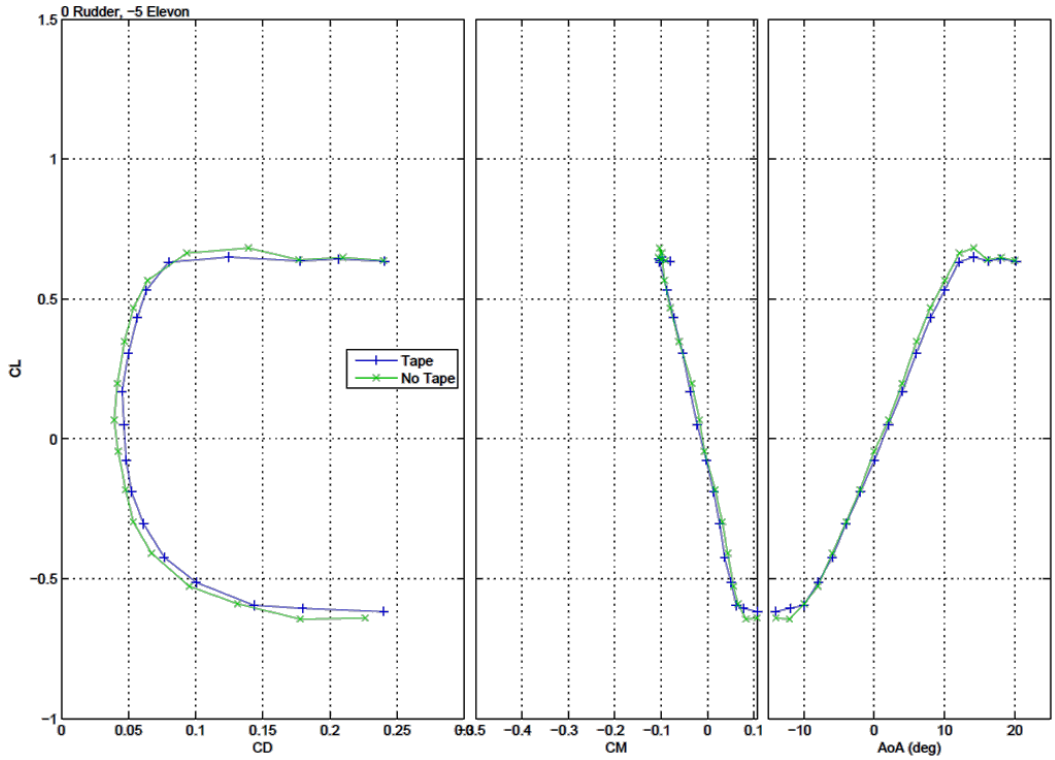

Figure 79: 0 Rudder, -5 Elevon, Transition Strip Comparison

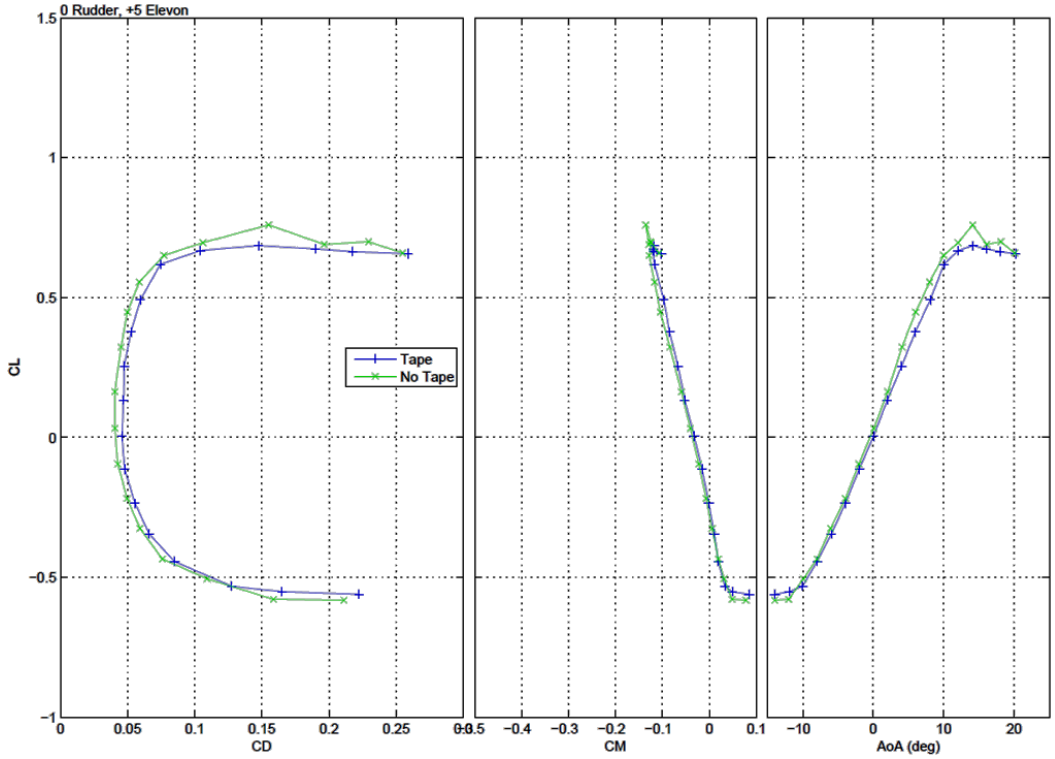

Figure 80: 0 Rudder, +5 Elevon, Transition Strip Comparison

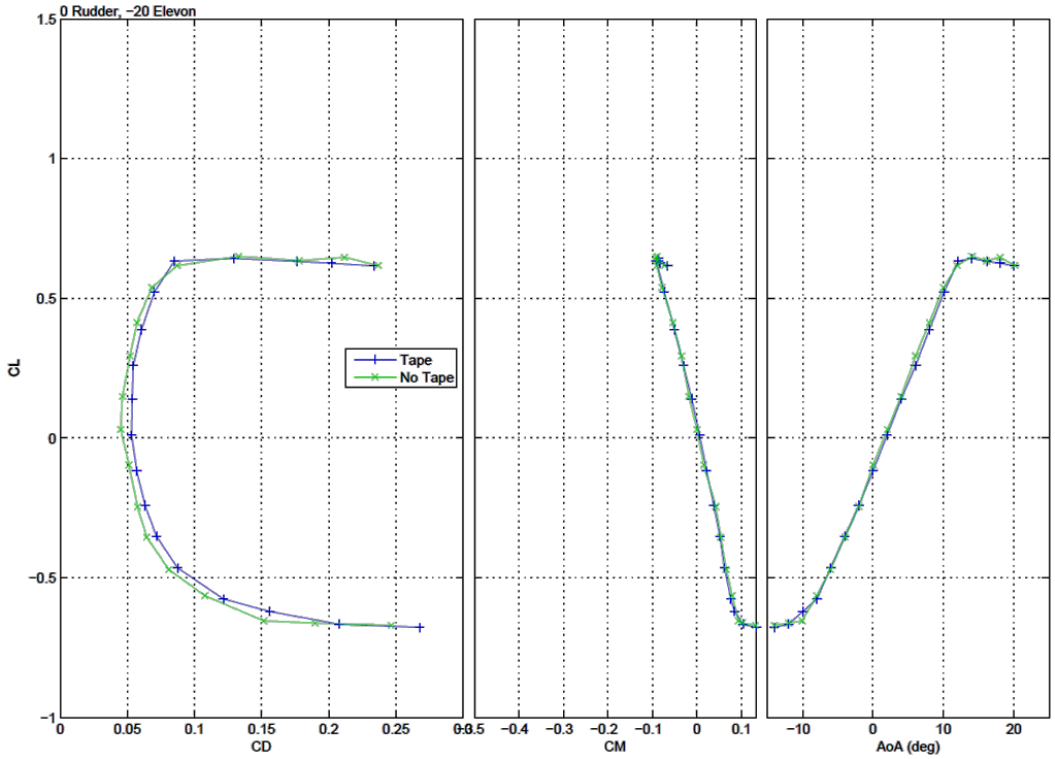

Figure 81: 0 Rudder, -20 Elevon, Transition Strip Comparison

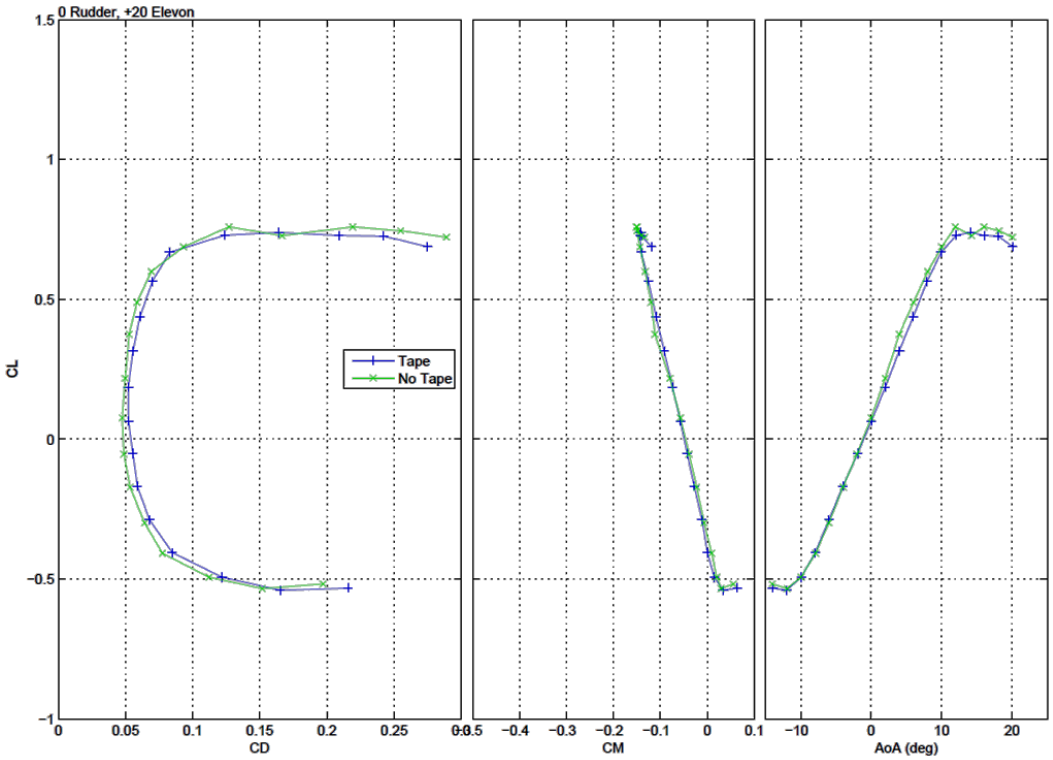

Figure 82: 0 Rudder, +20 Elevon, Transition Strip Comparison

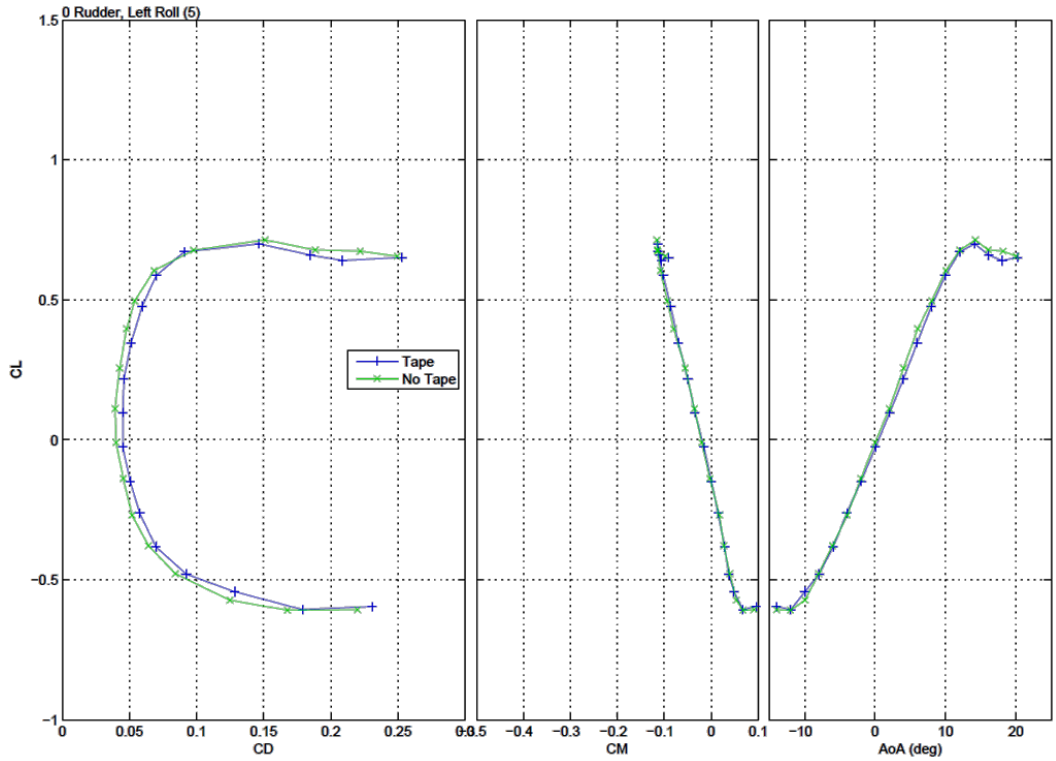

Figure 83: 0 Rudder, Left Roll (5 Degrees), Transition Strip Comparison

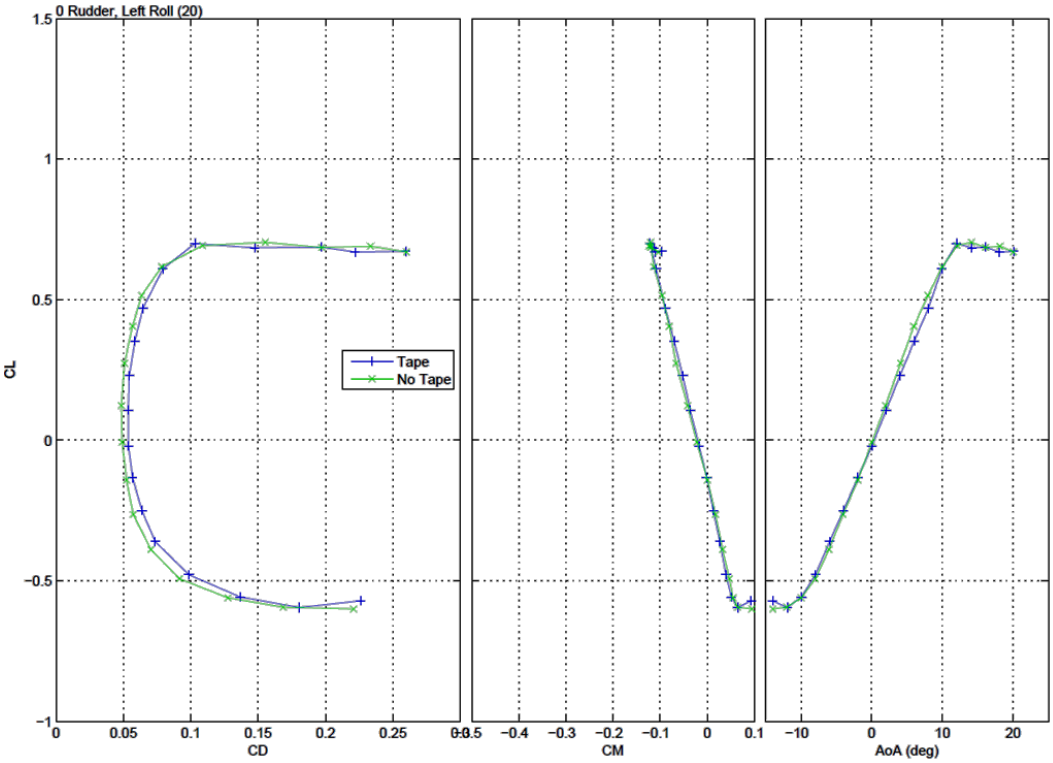

Figure 84: 0 Rudder, Left Roll (20 Degrees), Transition Strip Comparison

Appendix E: AVL Input Files

-Baseline AVL Input File

```
Amphibious_Flying_Wing
0.27
0    0    0 !out of ground effect
!0    1    -9.62  ! Ground effect: Ground at -9.618 feet
3838.83    34.32    147.07 !Reference area
26.82     0    0  !CG location for most aft position 5% SM
0.01324

SURFACE
Main Wing
6    1    20    -2
YDUPLICATE
    0
ANGLE
    0
TRANSLATE
0    0    0
SECTION
    0    0    0    57.45    0
AFILE
hsnlf213_smooth.dat
SECTION
    15.5271    10.18    0    42.513    0
AFILE
hsnlf213_smooth.dat
SECTION
    30.5960    44.121    0    22.0152    0
AFILE
hsnlf213_smooth.dat
CONTROL
    Aileron    1    0.7    0    0    0     -1
CONTROL
    Elevator   0.75    0.7    0    0    0     1
SECTION
    43.6551    73.535    0    4.2513    0
AFILE
hsnlf213_smooth.dat
CONTROL
    Aileron    1    0.7    0    0    0     -1
CONTROL
    Elevator   0.75    0.7    0    0    0     1
```

```
SURFACE
VS Upper
6    1    20    -2
YDUPLICATE
    0
ANGLE
    0
TRANSLATE
42.30728 36.7675 0
SECTION
    1.829    0    -4.1667    9.985    0
NACA
    0012
CONTROL
    Rudder    1    0.68    0    0    0    -1
SECTION
    0    0    0    19.97    0
NACA
   0012
CONTROL
    Rudder    1    0.77    0    0    0    -1
SECTION
    10.1851   0    23.2023    11.142    0
NACA
    0012
CONTROL
    Rudder    1    0.68    0    0    0    -1
SECTION
    11.52    0    26.2433    9.985    0
NACA
    0012
```

-Modified Control Surfaces AVL Input File

```
Amphibious_Flying_Wing_Modified
0.27
0    0    0 !out of ground effect
!0    1    -9.62  ! Ground effect: Ground at -9.618 feet
3838.83    34.32    147.07 !Reference area
26.82     0    0  !CG location for most aft position 5% SM
0.01324

SURFACE
Main Wing
6    1    20    -2
YDUPLICATE
    0
ANGLE
    0
TRANSLATE
0    0    0
SECTION
    0    0    0    57.45    0
AFILE
hsnlf213_smooth.dat
CONTROL
    Elevator   0.75    0.73    0    0    0     1
SECTION
    15.5271    10.18    0    42.513    0
AFILE
hsnlf213_smooth.dat
CONTROL
    Elevator   0.75    0.73    0    0    0     1
SECTION
    30.5960    44.121    0    22.0152    0
AFILE
hsnlf213_smooth.dat
CONTROL
    Aileron    1    0.73    0    0    0     -1
CONTROL
    Elevator   0.75    0.73    0    0    0     1
SECTION
    43.6551    73.535    0    4.2513    0
AFILE
hsnlf213_smooth.dat
CONTROL
    Aileron    1    0.73    0    0    0     -1
CONTROL
    Elevator   0.75    0.73    0    0    0     1
```

```
SURFACE
VS Upper
6    1    20    -2
YDUPLICATE
    0
ANGLE
    0
TRANSLATE
42.30728 36.7675 0
SECTION
    1.829    0    -4.1667    9.985    0
NACA
    0012
CONTROL
    Rudder    1    0.5    0    0    0     -1

SECTION
    0    0    0    19.97    0
NACA
   0012
CONTROL
    Rudder    1    0.6714    0    0    0     -1
SECTION
    10.1851   0    23.2023    11.142    0
NACA
    0012
CONTROL
    Rudder    1    0.5484    0    0    0     -1
SECTION
    11.52    0    26.2433    9.985    0
NACA
    0012
CONTROL
    Rudder    1    0.5149    0    0    0     -1
```

-AVL Mass File

```
#  Amphibious Flying Wing
#
#  Dimensional unit and parameter data.
#  Mass & Inertia breakdown.

#  Names and scalings for units to be used for trim and eigenmode calculations.
#  The Lunit and Munit values scale the mass, xyz, and inertia table data below.
#  Lunit value will also scale all lengths and areas in the AVL input file.
Lunit = 1 ft
Munit = 1 slug
Tunit = 1 s

#--------------------------
#  Gravity and density to be used as default values in trim setup (saves runtime
typing).
#  Must be in the unit names given above (i.e. m,kg,s).
g   = 32.2
rho = 0.001267

#--------------------------
#  Mass & Inertia breakdown.
#  x y z  is location of item's own CG.
#  Ixx... are item's inertias about item's own CG.
#
#  x,y,z system here must be exactly the same one used in the .avl input file
#     (same orientation, same origin location, same length units)
#
#  mass     x      y     z      Ixx       Iyy         Izz    [  Ixy   Ixz   Iyz ]
*   1.      1.     1.    1.     1.        1.          1.       1.    1.    1.
+   0.      0.     0.    0.     0.        0.          0.       0.    0.    0.
2916.149  26.82   0     -2.5    1515379.13 262034.017  1543783.282     ! entire
aircraft
```